MODAL ANALYSIS AND DESIGN OF COMPOUND GRATINGS AND FREQUENCY SELECTIVE SURFACES

by

HUNG LOUI

B.M., University of Colorado at Boulder, 2001

B.S., University of Colorado at Boulder, 2001

M.S., University of Colorado at Boulder, 2003

A thesis submitted to the

Faculty of the Graduate School of the

University of Colorado in partial fulfillment

of the requirements for the degree of

Doctor of Philosophy

Department of Electrical and Computer Engineering

2006

This thesis entitled:

Modal Analysis and Design of Compound Gratings

and Frequency Selective Surfaces

written by Hung Loui

for the Doctor of Philosophy degree

has been approved for the

Department of Electrical and Computer Engineering

by

_____

Prof. Zoya Popović

_____

Prof. Edward F. Kuester

Date _____

The final copy of this thesis has been examined by the signatories, and we find that both the content and the form meet acceptable presentation standards of scholarly work in the above mentioned discipline.

Loui, Hung (Ph.D., Electrical Engineering, Electrical and Computer Engineering)

Modal Analysis and Design of Compound Gratings and Frequency Selective Surfaces

Thesis directed by Profs. Zoya Popović and Edward F. Kuester

Abstract

This thesis presents a general method for the analysis of transmission and reflection of electromagnetic waves from complex thick/thin metallic frequency selective surfaces (FSS's), gratings and corrugated surfaces. The method is based on mode-matching using surface impedance boundary conditions and accounts for arbitrary profiles, lossy dielectric fillings/coatings for compound unit cells with multiple apertures. Perturbation theory is applied to include metal losses. In order to represent a complex thick FSS in terms of a network model that facilitates design, the Extended Generalized Scattering Matrix (EGSM) formulation is developed and criteria for resonance, Q and computation reduction are established. With minor modifications, the formulation also allows extension to the aperiodic case. The method is validated against both experiment and models from the literature. Specifically, analysis of simple and compound thick-metal transmission gratings, corrugated surfaces and thin-metal FSS's in the 30-300 THz frequency range is compared with several other methods and new compound thick-metal FSS results are reported. Agreement with experiment is obtained for a K-band thick FSS with tapered circular holes having similar TE and TM characteristics for scan angles up to $\pm 45^{\circ}$.

Dedication

To my beautiful wife Suzie, an inspiring fountain of love, faith and humility.

Personal Acknowledgments

My sincere and heart-felt gratitude goes to Dr. Marilyn Flachman, who believed in, cared for and encouraged me to succeed over the past 11 years. The Flachman family provided me refuge during the critical transition from high school to college and have been there for me ever since. I am truly blessed to receive so much of their kindness and generosity. To me, they are family. I am also grateful to my parents for laying the necessary foundation for my future through the sacrifices they made.

Professional Acknowledgments

First and foremost, I would like to thank Professor Zoya Popovć for her support of my interest in theoretical research despite recent funding trends for all things practical. This allowed me ample time to build a solid foundation in electromagnetics and encouraged my curiosity for science in technology. I am especially grateful for the opportunities to visit Universidad de Buenos Aires in Argentina and the Arecibo Observatory in Puerto Rico. These international visits broadened my horizons for discovery. By placing emphasis on laboratory work and machine shop training, she has strengthened my experimental abilities. Along the way, I have also gained good habits in preparing, writing and revising technical manuscripts.

I wish to express my sincere thanks to Professor Edward F. Kuester for his suggestions, technical inputs and unwavering support of my graduate work. Through our interactions, I have come to know an inspiring teacher of science and humanity. The quote by Benjamin Disraeli at the beginning of this thesis's introduction chapter perfectly describes my view of his influence in my life.

I truly enjoyed engaging research discussions with Professor Diana Skigin. She is a brilliant physicist full of passion and drive for scientific knowledge. Although my visit with her was short, it was most productive. Special thanks also go to Profs. Ricardo Depine, Angela Fantino and everyone in Grupo de Electromagnetismo Aplicado, Departamento de Fisíca, Facultad de Ciencias Exactas y

Naturales, Universidad de Buenos Aires for their warm companionship during my three month visit to Argentina.

Dr. George Lawrence put me on the road of discovery. He gave me the chance to work at the Laboratory for Atmospheric and Space Physics (LASP) as an undergraduate research assistant and taught me by example of how great research is to be conducted.

I especially enjoyed Numerical Methods in Photonics with Professor Robert McLeod, a class where I became familiar with FDTD, ray-tracing, Fourier, tomography, Eigen-mode and coupled-mode propagation algorithms.

Sid Gustafson from the Physics Trades Teaching Lab and Mark Eaton from the Manufacturing Center of the Integrated Teaching and Learning (ITL) Laboratory helped tremendously in the production of experimental gratings and frequency selective surfaces. Not only did I learn from them the necessary workman skills but also the importance of machine shop safety.

I would like to thank Dr. Michael Forman for this time saving LaTeXthesis template. His recognition of my work and subsequent recommendation for post-doctoral career placement are greatly appreciated.

To all those that were an integral part of my experience at CU Boulder, thank you for making graduate school a memorable experience for me!

This research is funded by a Department of Education Graduate Assistance in Areas of National Need (GAANN) Fellowship in Hybrid Signal Electronics (HYSE), award #P200A040154. The visit to Argentina was made possible by an NSF International Supplement to an ITR Collaborative Research Grant No. CCR-0112591.

Contents

Tables

Figures

Chapter 1

Introduction

The greatest good you can do for another is not just to share your riches but to reveal to him his own.

— Benjamin Disraeli, 1804 - 1881

1.1 Gratings and FSS's

Gratings (GT's) and frequency selective surfaces (FSS's) are an important class of periodic structures that scatter electromagnetic (EM) radiation by changing its amplitude, phase, direction and polarization. Planar GT's and FSS's surfaces can be categorized in terms of material content into two general classes:

1. Dielectric/Metal(DM) -
   Primarily dielectric with embedded metal/dielectric objects;

2. Metal/Dielectric(MD) -
   Primarily metal with dielectric layers, fillings or coatings.

The primary focus of this thesis is on the second class of GT's and FSS's, those that are Metal/Dielectric (see Fig. 1.1(b)), although the method presented can

be extended vigorously to cover the Dielectric/Metal case (Fig. 1.1(a)). The dominant use of MD types of surfaces in the millimeter to centimeter regime are in applications related to multi-band antennas and low-observable radomes which are covered in detail in Chapter 4.1.

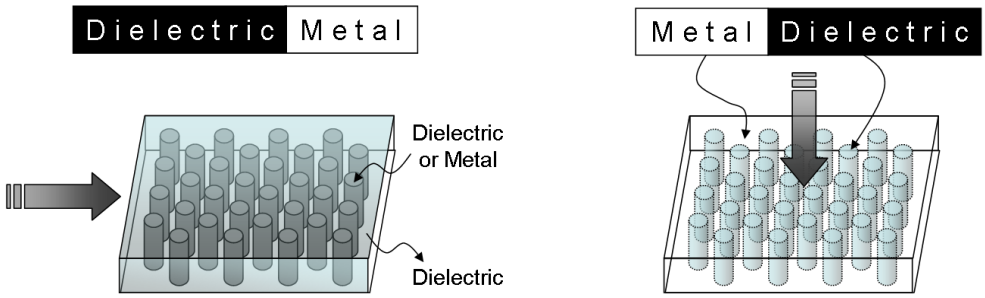

(a) Dielectric/Metal Surface (b) Metal/Dielectric Surface

Figure 1.1: Examples of Dielectric/Metal and Metal/Dielectric surfaces. (a) is a thick dielectric plate embedded with metal/dielectric cylindrical posts. (b) is (a)'s complement with dielectric posts perforating the thick-metal plate. The arrows represent the usual direction of excitation.

The MD class of GT's and FSS's can be further divided into surfaces that are metallically thin or thick. Both types can be free-standing or embedded in multi-layer dielectrics. The results of a simple keyword search using IEEE Xplore are given in Table 1.1. Clearly it is impractical to provide even a remote account of all work related to gratings and frequency selective surfaces. However, a large amount of references for FSS work are covered in books [1–3]. Likewise, gratings are discussed in [4, 5]. Because GT's are usually periodic in one dimension and FSS's in two, past results for the more general case are briefly summarized next.

1.1.1 Thin Metal

The majority of analyzed and manufactured FSS's are metallically thin and supported by thick-dielectric substrates. This is because metal patterns are relatively

Table 1.1: Literature search from 1348795 documents using IEEE Xplore

Keyword	**Hit**
FSS or Frequency Selective Surface	845
FSS or Frequency Selective Surface and Loss	74
Finite FSS or Finite Frequency Selective Surface	16
Dichroic and Plate	15
Thick FSS or Thick Frequency Selective Surface	4
Compound FSS or Compound Frequency Selective Surface	0
Grating	7718
Metal Grating	60
Gratings and Metal and Loss	24
Thick Gratings	3
Thick Metal Gratings	1
Compound Grating	1

straight forward to produce using conventional printed-circuit-board (PCB) process by either etching or surface milling. The most common design parameters are the element shape, the dielectric substrate and the number of layers. Performance evaluations are usually based on stability of resonant frequency, bandwidth and polarization response with respect to angle of incidence. Munk [3] showed that the complementary structure made up of patch islands inside periodically perforated apertures and sandwiched symmetrically by dielectric matching layers produces the best over-all response in terms of performance criteria stated above. By longitudinally cascading multiple layers, sharper band-edge roll-off can be achieved at the expense of angle sensitivity. Recently, Ma and Mittra [6] provided additional freedom in the design of thin multi-layer structures by allowing each layer to have a different periodicity; however results in terms of angle stability were not reported. Finally, it is interesting to quote Munk on his viewpoint of thick-metal FSS's: "Again, the fact is simply that no matter what fancy stuff you may put inside the waveguides (thick apertures), they are inherently scan independent

while the outside is scan dependent unless compensated (by dielectric layers). No amount of mindless computations can ever make up for that."

1.1.2 Thick Metal

In addition to providing sharp band-edge roll-off and improving band-separation, thick-metal FSS's find applications where mechanical strength and power handling are important [7]. However, their analysis is more complicated and cumbersome as can be seen by the fewer number of references given in Table 1.1. The earliest known thick-metal FSS investigation was done by Chen [8]. Schmier [1] has provided an extensive chapter on the design of band-pass radomes using thick-metal FSS's. A comparison between thick and thin-metal surfaces is provided in terms of Q and scan performance suggesting thick-metal FSS's are superior.

Performance degradation due to surface wave propagation inside multi-layer thin-metal FSS's was discussed and intriguingly Schmier proposes the following: "If the potential problems associated with the internal surface waves in a multiple-layer thin-screen FSS cannot be tolerated, then a single-thick-screen FSS with multiple irises is required. The multiple irises in the thick-screen FSS give equivalent performance to the multiple-layer thin-screen FSS, but because the irises all exist within the thick conducive screen no internal surface waves or the problems associated with them are possible." The irises he is referring to are multiple thin patches placed longitudinally in sequence inside each thick perforation. Although no experimental or numerical curves for this case is given, it certainly raise questions to Munk's comments above.

Table 1.1 shows that over the past 50 years, many researchers have studied the scattering of electromagnetic (EM) waves from one- and two-dimensionally periodic thin-metal gratings and frequency selective surfaces. Of those, some have worked on thick perforations or corrugations filled with or covered by multi-

layered dielectrics. There has been less work done on modelling finite structures and inclusion of metal/dielectric losses. Successful behavior prediction of a multitude of gratings, FSS's and most recently photonic/electromagnetic bandgap (PBG/EBG) media and metamaterials has been demonstrated. A representative, but far from complete, bibliography is given by the selection [1–3, 8–20].Due to the geometrical differences between various structures, different analytical and numerical methods are often used to analyze these structures. The advantages and limitations of each method are reviewed next.

1.2 Analysis Methods

A number of numerical techniques [21, 22] have been applied in the past to analyze periodic [1–3] and aperiodic scattering problems of the type to be considered here. These include: Circuit Equivalent Analysis (CEA), Electromotive Force Method (EMF), Method of Moments (MoM), Mode Matching (MM), Finite Element Method (FEM), Transmission Line Method (TLM) and the Finite Difference Time Domain (FDTD) method.

1.2.1 Circuit Equivalent Analysis

CEA is best suited for thin-metal free-standing periodic surfaces where the periodicity, thickness and dimensions of the inductive strips and/or capacitive gaps are much less than the excitation wavelength [23]. Although oblique incidences less than 45° from normal have been treated [24], cross-polarization and wide-angle responses cannot be predicted. Rather than using lumped equivalents, the EMF method [25] bases its analysis on assumed current distributions over the thin metallic strips. While successful at predicting the driving-point impedances of embedded active devices in a periodic grid above a dielectric substrate [26],

excitation is restricted to normal incidence because of the use of PEC and PMC symmetry planes. Other approaches based on mutual impedances and antenna theory [3] are more successful at solving multi-layered thin-metal planar FSS's for arbitrary incidence angles.

1.2.2 Method of Moments

MoM is applied [27] for thin-metal arrays having arbitrarily-shaped elements with unknown currents. The convergence properties are determined by the choice of basis functions used to expand the quasi-periodic form of the surface current density [9]. MoM solutions are electric or magnetic surface currents, requiring post-processing in order to obtain reflection and transmission responses. The complexity of the method increases for stratified media, as do extensions to thick-metal surfaces [10]. Further, Green's functions for arbitrary three-dimensional structures are difficult to formulate.

1.2.3 Mode Matching

MM was originally developed for waveguide bifurcation problems [28], where fields on each side of the discontinuity are expanded in terms of waveguide modes (an entire-domain basis). The mode matching procedure involves equating the expansions according to boundary conditions over the appropriate regions of the discontinuity. In the case of scattering from periodic structures, the fields above and below a unit cell are expanded into Floquet modes [29]. Like MoM, MM uses basis and test functions to reduce an integral equation to matrix form. The unknowns in this case are primarily field amplitudes and the basis and test functions used are essentially the eigenvectors of the structure. The orthogonality of the basis and test functions results in a smaller and easier to solve set of linear equations. Because transmission and reflection are defined in terms of field am-

plitudes, it is straightforward to cast the solution in matrix formats suitable for network analysis. This in turn enables the modeling of multi-layered geometries.

Although MM avoids the determination of structure-dependent Green's functions, it does so at the cost of finding eigenvectors in the various propagation regions. For simple canonical geometries, readily available closed-form eigenvectors can be used in analytical preprocessing to increase the algorithm's efficiency. Complex cross-sections with imperfect conductors and arbitrary dielectrics require other methods such as FEM to find the needed eigenvectors.

1.2.4 Finite Element Method

Originally introduced to solve closed domain problems, FEM is well suited to determine the eigenvectors of an arbitrary structure. For open problems, implementation of absorbing boundary conditions increases its complexity and reduces accuracy at high incidence angles. To handle open problems involving arbitrary three-dimensional periodic scatterers, hybrids of FEM with Boundary Element (FE/BE) [30] or Boundary Integral (FE/BI) [31] methods have been introduced. The generality of these algorithms requires significant computational resources and long run times in solving fields iteratively over frequency.

1.2.5 Finite Difference Time Domain

For obtaining broadband responses, time domain methods can be effective. A detailed discussion of FDTD in solving FSS problems is given in [32]. Oblique excitation is difficult for time-domain methods in the case of periodic scatterers due to the required phase shift between relevant periodic boundaries. The phase shift in the frequency domain translates to time retardation, requiring data storage for all time instances along every periodic boundary. Harms et al. [33] excited the FDTD mesh by the phasor equivalent of sinusoid and cosinusoid sources, thus

allowing the enforcement of phase delay at the periodic boundaries. This method for oblique incidence requires a separate FDTD run per frequency point. This and the addition of curvilinear meshes require significant computation time and code complexity. Other time domain methods such as TLM also have similar problems as FDTD at oblique incidence. The use of perfect PEC and PMC walls in the TLM method [34] is similar to the EMF case restricting the angle of incidence to normal.

1.2.6 Network Approaches

Plane-wave scattering from multi-layered dielectrics without metal has been traditionally studied using the network approach where each layer is modeled as a section of transmission line with a different characteristic impedance. Extensions of the traditional network representations such as admittance, impedance, transfer and scattering matrices to their generalized multi-terminal form [35] enable interconnections of multi-mode passive structures. The multi-terminal/multi-mode form of generalized network formulation [36] has been applied in guiding structures, i.e. N-Furcation problems [37]. Use of the generalized admittance matrix (GAM), generalized impedance matrix (GIM), generalized transfer matrix (GTM) and generalized scattering matrix (GSM) for various types of discontinuities appearing in multi-layered periodic structures has been discussed in [38]. Comparisons between R-Matrix, GSM and GTM as applied to gratings are given in [39], indicating that GSM is superior from the viewpoint of numerical stability. The algebraic equations resulting from GAM and GIM are more complicated, leading to longer computing times. Because GTM requires an equal number of modes on both sides of an abrupt junction, it has difficulty converging to the correct solution for problems involving infinitely thin structures [40].

Network approaches in combination with other methods can analyze a large va-

riety of metal-dielectric thin-thick planar scatterers without sacrificing efficiency. The MM-FE-GSM hybrid combines the speed of MM, the generality of FE and the flexibility of GSM and has already been utilized on a large class of scattering problems [11, 41, 42]. Oblique excitations of both thick and thin FSS's [43] with arbitrary aperture cross-sections and on-axis longitudinal perforations have been successfully analyzed. In many instances, approximate solutions and observable trends can be quickly obtained using a fewer number of modes. This in turn enables design by iterations on a standard personal computer (PC). Because there are various ways to obtain the eigen solutions of a structure, it is not necessary to restrict a hybrid method to the use of FE. By extending the MM-GSM parts of existing hybrid methods, novel metal GT's and FSS's can be efficiently analyzed. A further motivation for this extension is made evident upon closer examination of Table 1.1. Although our search was not all encompassing, we find that the following properties of GT's and FSS's are in need of research attention due to the relative small number of publications. They are compound, thick, finite and with loss.

1.3 Thesis Purpose

The purpose of this thesis is to extend the capabilities of the Mode Matching-Generalized Scattering Matrix (MM-GSM) method such that *compound periodic* (multiple apertures per unit cell) and aperiodic scattering problems involving metal losses can be efficiently solved and computationally implemented. The resulting matrix formulations for both periodic and aperiodic scattering problems are similar and further simplify to the *simple periodic* case when the number of apertures per unit cell reduces to unity. This means that the same code used to study simple periodic surfaces can be modified with little effort to handle

compound periodic and aperiodic surfaces. The method presented in this paper is capable of efficiently analyzing the reflection and transmission properties of TE- and TM-polarized plane waves incident at arbitrary angles onto the following types of scatterers:

1. Thin or thick arbitrarily shaped FSS's;
2. Gratings with generalized profiles;
3. Metal structures with multiple layers of dielectric fillings and/or coatings;
4. Thick-metal structures with arbitrary internal connections.

In addition, the above geometries can be:

a. Periodic or aperiodic;

b. Lossless or low-loss;

c. Transmitting and/or reflecting.

Arbitrarily incident waves can be treated by the superposition of plane waves incident at multiple angles. Finally, internal excitations can be included for radiation analysis. In order to describe the problem at hand, we refer to the generalized geometry as a *compound structure*. As an example, we define a *compound periodic surface* as an assembly of identical unit cells each consisting of possibly dissimilar elements as illustrated in Fig. 1.2(b) arranged in a one- or two-dimensional infinite array. An example of this definition in one dimension is a compound grating with N closely spaced corrugations or perforations per unit cell, discussed in Chapter 4.3. In the case where a unit cell is made up of only one element, the surface reduces to that of a *simple periodic surface*. An example of a simple unit cell analyzable by the current state-of-the-art MM-GSM algorithm is shown in Fig. 1.2(a). If the unit-cell is not repeated periodically but rather situated within

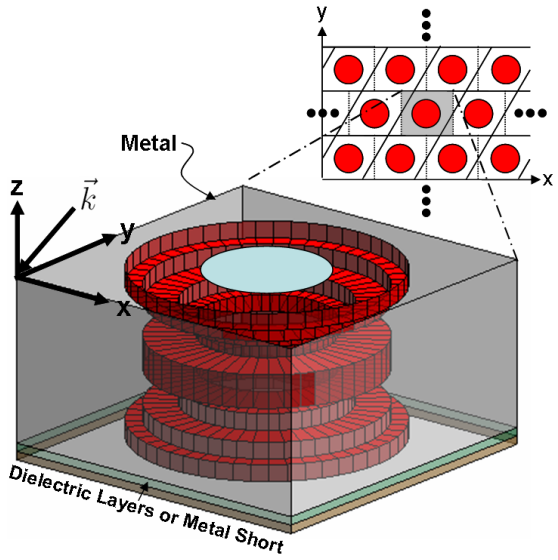

(a)

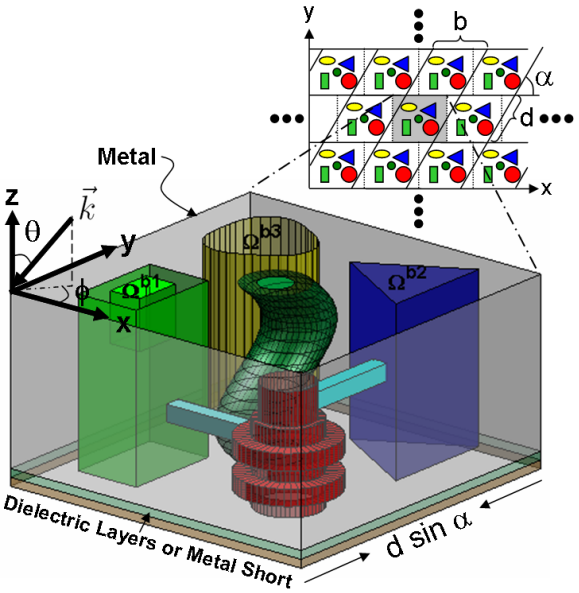

(b)

Figure 1.2: (a) A simple periodic unit cell. (b) A compound periodic unit cell consisting of a number of waveguides having various cross-sections.

an infinite domain, then the surface is called an *aperiodic surface*. Examples of aperiodic surfaces are a finite number of apertures located in an infinite ground plane or a finite number of planar metal patches situated in infinite free space or attached to an infinite dielectric substrate.

1.4 Thesis Organization

The outline of the thesis is as follows:

- Chapter 2 describes the main approach for analyzing plane-wave scattering from a generalized thick compound surface. In order to represent a complex scatter in terms of a network model that facilitates design, the Extended Generalized Scattering Matrix (EGSM) formulation is developed. Detailed mathematical derivations for both the periodic and aperiodic problems are given and similarities between them are highlighted.

- Chapter 3 compares the results from our theory with results for various examples found in the literature for GT's, corrugated surfaces (CS's) and FSS's in the 30-300 THz range. Additionally, criteria for resonance, Q and an identity relevant for computation reduction are established using the EGSM formalism presented in Chapter 2.

- Chapter 4 introduces various applications of GT's and FSS's. Specifically, the applicability of thick-metal FSS for use in airborne applications is discussed and relevant design issues are identified. Based on the criteria developed in Chapter 3, a K-band thick FSS with linear-tapered circular holes having similar TE and TM characteristics for scan angles up to $\pm 45^{\circ}$ is designed. A special taper is introduced and shown to improve angle stability and transmission bandwidth. This chapter also provides detailed information on the measurement setup used to characterize the manufactured FSS's.

- Chapter 5 summarizes the research findings of this thesis and lists the major contributions made. Future work in the areas of loss, convergence and active compound structures are also discussed. Relevant factors affecting the measured results are identified and a new measurement setup is proposed.

Chapter 2

Theory

Lack of will power has caused more failure than lack of intelligence or ability.

— Flower A. Newhouse, 1909 - 1994

2.1 Analysis Approach

We start at the highest level of abstraction with a complicated geometry shown in Fig. 2.1 (longitudinal cross section) and Fig. 2.2 (transverse cross section). The geometry is then divided in the longitudinal and transverse dimensions into slices and sub-domains respectively. The power of an incident wave is coupled longitudinally in Fig. 2.1 in two ways: directly through the perforation and by complicated coupling between different perforations. Imposing the boundary conditions, the standard MM approach is extended to take into account all coupling mechanisms, thus giving a solution to the original complex geometry. In the remainder of this section, the higher-level formulation of the problem is given, separated into longitudinal and transverse dimensions.

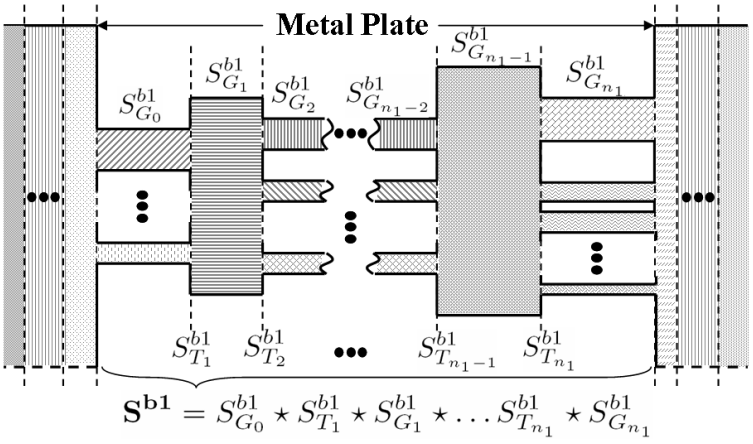

(a) Abrupt longitudinal transitions

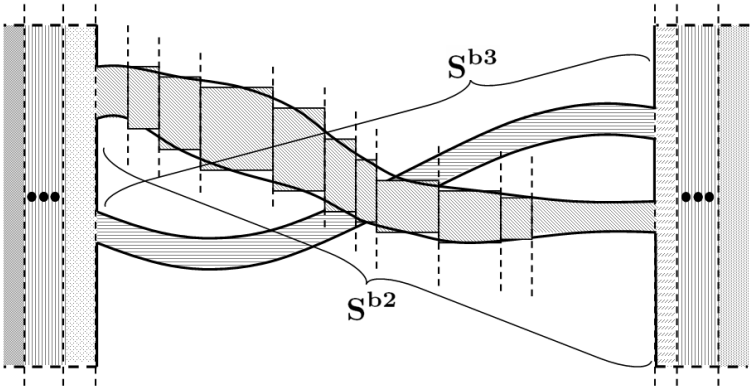

(b) Smooth longitudinal transitions

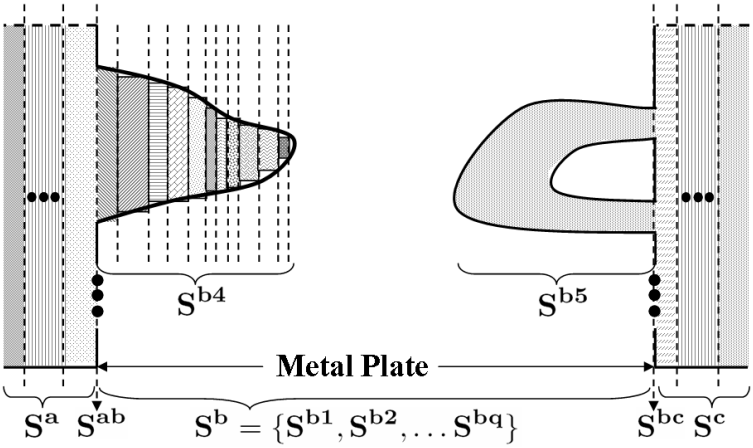

(c) Corrugations and feedback

Figure 2.1: Various longitudinal discontinuities. White regions are metal and shaded regions are waveguides filled with different dielectrics.

2.1.1 Longitudinal Dimension

Fig. 2.1 shows the longitudinal cross section of various geometries, where we distinguish between three-dimensional waveguide *sections*, and two-dimensional *junctions* and *transitions*. A *junction* is the discontinuity between two waveguides inside the metal plate, while a *transition* is a collection of junctions due to possible waveguide bifurcations and/or interconnections. These guided-wave sections and transitions are represented by their equivalent extended-generalized-scattering-matrices (EGSM) S_G and S_T, respectively. The notation is as follows: the subscript of each EGSM denotes the number of a transition ($_T$) or guiding section ($_G$), while the superscripts ($^{\mathbf{a,c}}$) and ($^{\mathbf{b}}$) specify multi-layer dielectrics, and metal plate layers, respectively. The combined superscripts ($^{\mathbf{ab}}$) and ($^{\mathbf{bc}}$) indicate boundaries between different types of layers. In addition, the various metal profiles are described by a number in the superscript, e.g., (^{b1}).

Unlike the standard scattering matrix which contains only reflection and transmission coefficients of propagating modes, the generalized-scattering-matrix (GSM) also contains coefficients for evanescent modes at a junction. Because a transition can contain multiple junctions, the matrix S_T is an extended GSM, or EGSM, relating amplitudes of forward and reverse modes between all junctions at a transition. For example, in Fig. 2.1(a), sections of different waveguides are joined by abrupt transitions inside a thick-metal plate where transitions $S^{b1}_{T_1}$ and $S^{b1}_{T_2}$ both contain multiple junctions. Similarly, because a slice can contain multiple waveguide sections, the EGSM S_G relates amplitudes of forward and reverse modes at the ends of all waveguide sections between two transitions.

The number of junctions at different transitions can vary and the dielectric fillings, lengths, types and cross-sectional shapes of the waveguides are arbitrary. As an example, both a single conductor waveguide and a coaxial type waveguide are connected at the transition $S^{b1}_{T_{n_1}}$; they are coupled by the waveguide to the left

of $S^{b1}_{T_{n_1}}$ and in dielectric layers to the right of the aperture plane. It is important to point out that aperture openings in Fig. 2.1(a) on both sides of a thick-metal plate need not have the same cross section, be of the same type or be aligned along the same axis. Furthermore, the number of aperture openings on either side of the metal plate is arbitrary.

It is possible to obtain a single EGSM inside the plate of Fig. 2.1(a) by way of the EGSM cascade operator $\star$ (defined in Appendix A):

$$\mathbf{S^{b1}} = S^{b1}_{G_0} \star S^{b1}_{T_1} \star S^{b1}_{G_1} \star \ldots S^{b1}_{T_{n_1}} \star S^{b1}_{G_{n_1}}, \tag{2.1}$$

where n_1 is the number of transitions in sub-domain **b1**. The ability to model abrupt transitions also allows us to model an arbitrary longitudinal profile by approximating it with many short waveguide sections connected by small abrupt transitions as shown in Fig. 2.1(b).

In the case of a uniformly filled waveguide sub-domain **b3** (also shown in Fig. 2.1(b)), where reflections from the gradual bends are negligible, it is sufficient to consider it as a straight section of the same waveguide having the length of the bent waveguide [44,45]. This reduces the amount of computation involved because the EGSM is simply

$$\mathbf{S^{b3}} = S^{b3}_{G_0}. \tag{2.2}$$

Fig. 2.1(b) also emphasizes that aperture connections are allowed to cross inside the plate; this is because an EGSM once determined for a transition or section is coordinate shift invariant. Furthermore, the apertures on either side of the plate are not required to penetrate the plate completely, as in the case of reflection only surfaces shown in Fig. 2.1(c) where an arbitrary corrugation filled with multilayered dielectrics is broken down into sections and transitions, where

$$\mathbf{S^{b4}} = \mathbf{S^{b4}_{11}} = S^{b4}_{G_0} \star S^{b4}_{T_1} \star S^{b4}_{G_1} \star \ldots S^{b4}_{T_{n_4}} \star S^{b4}_{G_{n_4}} \star S^{b4}_{T_{n_4+1}}. \tag{2.3}$$

The additional transition $S^{b4}_{T_{n_4+1}}$ at the end represents the short. In fact, an aperture is allowed to connect to other apertures on the same side of the plate; this kind of co-connection is also shown in Fig. 2.1(c), where

$$\mathbf{S^{b5}} = \mathbf{S^{b5}_{22}} = S^{b5}_{T_0} \star S^{b5}_{G_0} \star S^{b5}_{T_1} \star S^{b5}_{G_1} \star \ldots S^{b5}_{T_{n_5}} \star S^{b5}_{G_{n_5}}, \tag{2.4}$$

with $S^{b5}_{T_0}$ representing the short on the left. In general

$$\mathbf{S^{bq}} = \underbrace{(S^{bq}_{T_0}\star)}_{\text{reflect}} \underbrace{S^{bq}_{G_0} \star S^{bq}_{T_1} \star S^{bq}_{G_1} \star \ldots S^{bq}_{T_{n_q}} \star S^{bq}_{G_{n_q}}}_{\text{through}} \underbrace{(\star S^{bq}_{T_{n_q+1}})}_{\text{reflect}}. \tag{2.5}$$

Because EGSMs $\mathbf{S^{b4}}$ and $\mathbf{S^{b5}}$ are decoupled inside the plate, it is convenient mathematically to combine sub-domains **b5** and **b4** into a single sub-domain **b6** such that,

$$\mathbf{S^{b6}} = \begin{bmatrix} \mathbf{S^{b4}_{11}} & \mathbf{0} \\ \mathbf{0} & \mathbf{S^{b5}_{22}} \end{bmatrix}. \tag{2.6}$$

We chose the labeling scheme of $\mathbf{S^{b4}}$ and $\mathbf{S^{b5}}$ to emphasize the fact that the numbers of corrugations on the left and right-hand side of the plate are in general different. In the case where there are n and p corrugations on the left- and right-hand sides of the plate respectively, it is always possible to assemble them in a single large EGSM, where

$$\mathbf{S^{bk}} = \text{diag}\{\mathbf{S^{bL_1}_{11}} \ldots \mathbf{S^{bL_n}_{11}}, \mathbf{S^{bR_1}_{22}} \ldots \mathbf{S^{bR_p}_{22}}\}. \tag{2.7}$$

In actual implementation, we use (2.7) because it encapsulates all of the corrugations into a single EGSM.

Having shown various types of longitudinal discontinuities, each of the relatively complex metal profiles in Fig. 2.1(a)-2.1(c) can now be stacked to form a generalized compound unit-cell. The EGSMs of the multi-layer dielectrics outside the metal plate are:

$$\mathbf{S^{a}} = S^{a}_{G_0} \star S^{a}_{T_1} \star S^{a}_{G_1} \star \ldots S^{a}_{T_{na}} \star S^{a}_{G_{na}}, \tag{2.8}$$

$$\mathbf{S^{c}} = S^{c}_{G_0} \star S^{c}_{T_1} \star S^{c}_{G_1} \star \ldots S^{c}_{T_{n_c}} \star S^{c}_{G_{n_c}}. \tag{2.9}$$

where n_a and n_c are the numbers of transitions on the left-hand and right-hand side of the metal plate respectively. In order to calculate the overall EGSM, the EGSMs outside of the metal plate $\mathbf{S^a}$ and $\mathbf{S^c}$ are cascaded through the transitions $\mathbf{S^{ab}}$ and $\mathbf{S^{bc}}$ with the EGSM $\mathbf{S^b}$ inside of the metal plate:

$$\mathbf{S} = \mathbf{S^a} \star \mathbf{S^{ab}} \star \mathbf{S^b} \star \mathbf{S^{bc}} \star \mathbf{S^c}, \tag{2.10}$$

where,

$$\mathbf{S^b} = \{\mathbf{S^{b1}} \dots \mathbf{S^{bq}}\}, \tag{2.11}$$

and $\{\}$ is the EGSM assembly operator defined in Appendix A.2.

In summary, by breaking a complex structure into sections and transitions and representing them by equivalent EGSMs, we are able to reduce the overall problem of scattering to the determination of the individual EGSMs. One advantage of this approach is that the individual EGSMs can be calculated separately and often *a priori* in a coordinate system best suited for an analytical solution. Because the resulting EGSMs operate on mode amplitudes, they are easily cascaded via standard operators. This abstraction alleviates tedious coordinate notation and facilitates parallel computing.

Although not shown in Fig. 2.1(a), the vertical combination of Fig. 2.1(a)-2.1(c) can also be repeated horizontally to include structures that contain dielectric layers sandwiched between multiple thick-metal plates, each with its own corrugations and perforations. In this general case, the equation describing the overall EGSM is

$$\mathbf{S} = \mathbf{S^1} \star \mathbf{S^{12}} \star \mathbf{S^2} \star \mathbf{S^{23}} \star \dots \mathbf{S^{2j}} \star \mathbf{S^{(2j)(2j+1)}} \star \mathbf{S^{2j+1}}, \tag{2.12}$$

where we have replaced **a** and **ab** in (2.10) with **1** and **12**, **b** and **bc** with **2** and **23** etc., to show the general process of EGSM cascade for **j** metal plates alternated with $\mathbf{j+1}$ regions of multi-layer dielectrics (including the outer air regions). For

the common case where a metal layer $\mathbf{j_0}$ can be regarded as vanishingly thin, we handle that in the present method by setting:

$$\mathbf{S}^{\mathbf{j_0}} = \begin{bmatrix} \mathbf{0} & \mathbf{I} \\ \mathbf{I} & \mathbf{0} \end{bmatrix}, \tag{2.13}$$

for such a layer, where $\mathbf{I}$ is the identity matrix.

2.1.2 Transverse Dimension

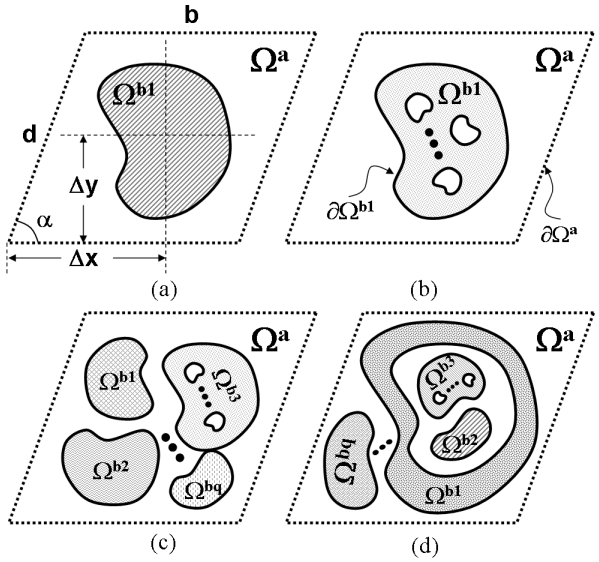

Figure 2.2: Transition classifications where shaded areas represent waveguide apertures and white spaces are metal. (a) is a simple unit-cell having a single-conductor waveguide at the interface. (b) is another simple unit-cell but with a multi-conductor waveguide at the junction. (c) is a compound unit-cell filled with q waveguides of type (a) and (b). (d) is a nested compound unit-cell where (a) is nested inside a metal island of (b).

Fig. 2.2 and its caption describe the classification of possible transverse cross-sections that correspond to the longitudinal slices in Fig. 2.1. For a periodic scatterer the largest domain $\mathbf{\Omega^a}$, shown as a parallelogram, represents the unit cell. The parallelogram angle α and periods d and b define a lattice whose field can be described by Floquet modes. Within each $\mathbf{\Omega^a}$, the q smaller aperiodic

sub-domains $\mathbf{\Omega^b} \subseteq \mathbf{\Omega^a}$ are described by $\mathbf{\Omega^b} = \{\Omega^{b1}, \ldots \Omega^{bq}\}$, each with its own set of eigenmodes. In the case of an aperiodic scatterer where there is no meaningful unit cell, the domain $\mathbf{\Omega^a}$ extends to infinity, and Floquet modes are replaced by a continuum of plane waves. In the case of a waveguide-to-waveguide transition, the domain $\mathbf{\Omega^a}$ is the larger waveguide, and its shape defines the boundary which is no longer restricted to a parallelogram. The fields on both sides of the transverse transition are expanded in terms of waveguide modes in this case. In summary, the transverse boundary $\partial\Omega^a$ can have an arbitrary shape and the fields inside can be expanded in terms of waveguide, Floquet or planewave modes depending on the problem.

2.2 Compound Periodic Formulation

To setup notation and illustrate the mathematical procedure, let us assume initially $\Omega^b \subseteq \Omega^a$ and expand the fields in Ω^a and Ω^b as follows:

$$\vec{E}^a_T(\vec{\rho}, z) = \sum_m (a^+_m(z) + a^-_m(z))\vec{E}^a_{T_m}(\vec{\rho}), \tag{2.14}$$

$$\vec{H}^a_T(\vec{\rho}, z) = \sum_m (a^+_m(z) - a^-_m(z))\vec{H}^a_{T_m}(\vec{\rho}), \tag{2.15}$$

$$\vec{E}^b_T(\vec{\rho}, z) = \sum_q \sum_{p_q} (b^{q+}_{p_q}(z) + b^{q-}_{p_q}(z))\vec{E}^{bq}_{T_{p_q}}(\vec{\rho}), \tag{2.16}$$

$$\vec{H}^b_T(\vec{\rho}, z) = \sum_q \sum_{p_q} (b^{q+}_{p_q}(z) - b^{q-}_{p_q}(z))\vec{H}^{bq}_{T_{p_q}}(\vec{\rho}), \tag{2.17}$$

where $a^\pm_m(z) = A^\pm_m e^{\mp\gamma^a_m z}$ and $b^{q\pm}_{p_q}(z) = B^{q\pm}_{p_q} e^{\mp\gamma^{bq}_{p_q} z}$. The transverse position vector is $\vec{\rho} = x\hat{x} + y\hat{y}$, q is the sub-domain identifier in Ω^b and subscripts m and p_q are mode designations in Ω^a and Ω^{bq}, respectively. In practice, these subscripts expand to contain multiple indices in order to capture specific mode-types such as TE, TM, TEM, etc. The magnitude and phase dependence on the longitudinal coordinate z is captured in $a^\pm_m(z)$ and $b^{q\pm}_{p_q}(z)$, where the $+$ and $-$ superscripts

are used to designate forward and reverse modes respectively. $A_m^{\pm}$ and γ_m^a are the amplitude and propagation constant of the mth mode of Ω^a. Similarly, $B_{p_q}^{q\pm}$ and $\gamma_{p_q}^{bq}$ are the amplitude and propagation constant of the p_qth mode of Ω^{bq}. The transverse modal field distributions $\vec{E}_{T_m}^a$, $\vec{H}_{T_m}^a$, $\vec{E}_{T_{p_q}}^{bq}$ and $\vec{H}_{T_{p_q}}^{bq}$ are vector functions of the cross-sectional coordinates only and depend on the waveguide type in Ω^{bq}. The mode fields are assumed to be normalized in some convenient way (see, e.g., (2.23) below). Without loss of generality, we choose the junction between Ω^a and Ω^b to be at $z = 0$, and enforce the continuity of tangential electric fields (including metal losses) through the following set of equations:

$$\sum_m (A_m^+ + A_m^-)\vec{E}_{T_m}^a(\vec{\rho}) = \begin{cases} \displaystyle\sum_q \sum_{p_q} (B_{p_q}^{q+} + B_{p_q}^{q-})\vec{E}_{T_{p_q}}^{bq}(\vec{\rho}), & \vec{\rho} \in \Omega^{bq}, \\ \pm Z_s \hat{z} \times \displaystyle\sum_m (A_m^+ - A_m^-)\vec{H}_{T_m}^a(\vec{\rho}), & \vec{\rho} \in \Omega^a - \Omega^b; \end{cases} \tag{2.18}$$

where $\hat{z}$ is the unit vector along the z-axis. The choice of the $+$ or $-$ sign depends on whether the outward normal from the conductor $\Omega^a - \Omega^b$ is $+\hat{z}$ or $-\hat{z}$, respectively. The first statement of (2.18) ensures that the tangential electric field is continuous across each Ω^{bq}. The second statement of (2.18) enforces a surface impedance boundary condition on the tangential fields over the metal surfaces inside Ω^a but outside of all Ω^{bq}. The parameter

$$Z_s = \sqrt{\frac{\mu_c(x, y, \omega)}{\epsilon_c(x, y, \omega) - j\sigma_c(x, y, \omega)/\omega}} \tag{2.19}$$

is the equivalent surface impedance given by the complex wave impedance for a plane wave in a non-PEC medium. The parameters $\mu_c(x, y, \omega)$, $\epsilon_c(x, y, \omega)$, $\sigma_c(x, y, \omega)$ are the permeability, permittivity, and conductivity of the metal as functions of transverse coordinates and angular frequency, respectively. For readability, we hereafter suppress the notation of transverse coordinate dependence.

We first take the cross product of both sides of (2.18) by $\vec{H}^{a*}_{T_n}, n = 1, 2 \ldots m$, then take the dot product with $\hat{z}$ and integrate over Ω^a to obtain:

$$\sum_m (A^+_m + A^-_m) \underbrace{\int_{\Omega^a} \vec{E}^a_{T_m} \times \vec{H}^{a*}_{T_n} \cdot \hat{z}\, dS}_{Y^{a*}_{mn}} = \sum_q \sum_{p_q} (B^{q+}_{p_q} + B^{q-}_{p_q}) \underbrace{\int_{\Omega^{bq}} \vec{E}^{bq}_{T_{p_q}} \times \vec{H}^{a*}_{T_n} \cdot \hat{z}\, dS}_{C^q_{p_q n}} + \sum_m (A^+_m - A^-_m) \underbrace{\int_{\Omega^a - \Omega^b} (\mp Z_s) \vec{H}^a_{T_m} \cdot \vec{H}^{a*}_{T_n}\, dS}_{Y^s_{mn}}. \quad (2.20)$$

Equation (2.20) although general, often produces matrices that are full for sub-domains having hybrid-modes. However, in the case where Ω^a is filled with a homogeneous medium, the transverse fields $\vec{E}^{a*}_{T_n}$ and $\vec{H}^{a*}_{T_n}$ are related by

$$\vec{H}^{a*}_{T_n} = Y^{a*}_n \hat{z} \times \vec{E}^{a*}_{T_n}, \quad (2.21)$$

where Y^a_n is the admittance of mode n given by

$$Y^a_n = \begin{cases} \frac{\gamma^a_{1n}}{j\omega\mu^a}, & \text{TE}, \\ \frac{j\omega\epsilon^a}{\gamma^a_{2n}}, & \text{TM}. \end{cases} \quad (2.22)$$

The additional subscripts $_1$ and $_2$ in γ^a designate TE and TM modes, respectively. Utilizing (2.21) and the orthonormal condition

$$\int_{\Omega^a} \vec{E}^a_{T_m} \cdot \vec{E}^{a*}_{T_n}\, dS = \delta_{mn}, \quad (2.23)$$

the overlap integrals in (2.20) reduce to:

$$Y^{a*}_{mn} = Y^{a*}_n \int_{\Omega^a} \vec{E}^a_{T_m} \cdot \vec{E}^{a*}_{T_n}\, dS = Y^{a*}_n \delta_{mn}, \quad (2.24)$$

$$C^q_{p_q n} = Y^{a*}_n \int_{\Omega^{bq}} \vec{E}^{bq}_{T_{p_q}} \cdot \vec{E}^{a*}_{T_n}\, dS, \quad (2.25)$$

$$Y^s_{mn} = \mp\, Y^a_m Y^{a*}_n \int_{\Omega^a - \Omega^b} Z_s \vec{E}^a_{T_m} \cdot \vec{E}^{a*}_{T_n}\, dS. \quad (2.26)$$

If Z_s is not a function of the transverse coordinates, (2.26) reduces to:

$$Y^s_{mn} = \mp Z_s Y^a_m Y^{a*}_n \left(\delta_{mn} - \int_{\Omega^b} \vec{E}^a_{T_m} \cdot \vec{E}^{a*}_{T_n} \, dS \right). \tag{2.27}$$

Further reductions of the overlap integrals in (2.25) and (2.27) are possible through the use of identities provided in [46, 47]. Specifically, the conversion of (2.25) and (2.27) to contour integrals can significantly improve the speed of the MM procedure when numerical methods such as FEM is used to determine $\vec{E}^a_{T_m}(\vec{\rho})$ or $\vec{E}^{bq}_{T_{pq}}(\vec{\rho})$. Let

$$\mathbf{A}^{\pm} = \begin{bmatrix} A^{\pm}_1 \\ \vdots \\ A^{\pm}_m \end{bmatrix}, \quad \mathbf{Y^{a*}} = \begin{bmatrix} Y^{a*}_1 & 0 & 0 \\ 0 & \ddots & 0 \\ 0 & 0 & Y^{a*}_m \end{bmatrix}, \tag{2.28}$$

$$\mathbf{B^{\pm}_q} = \begin{bmatrix} B^{q\pm}_1 \\ \vdots \\ B^{q\pm}_{p_q} \end{bmatrix}, \quad \mathbf{C_q} = \begin{bmatrix} C^q_{11} & \cdots & C^q_{1m} \\ \vdots & \ddots & \vdots \\ C^q_{p_q 1} & \cdots & C^q_{p_q m} \end{bmatrix}, \tag{2.29}$$

and

$$\mathbf{Y^s} = \begin{bmatrix} Y^s_{11} & \cdots & Y^s_{1m} \\ \vdots & \ddots & \vdots \\ Y^s_{m1} & \cdots & Y^s_{mm} \end{bmatrix}. \tag{2.30}$$

Equation (2.20) becomes a matrix equation of the form:

$$\begin{aligned} \left(\mathbf{Y^{a^*}} - \mathbf{Y^{s^t}} \right) \mathbf{A}^+ + \left(\mathbf{Y^{a^*}} + \mathbf{Y^{s^t}} \right) \mathbf{A}^- & \\ = [\mathbf{C^t_1} \cdots \mathbf{C^t_q}] \left(\begin{bmatrix} \mathbf{B^+_1} \\ \vdots \\ \mathbf{B^+_q} \end{bmatrix} + \begin{bmatrix} \mathbf{B^-_1} \\ \vdots \\ \mathbf{B^-_q} \end{bmatrix} \right) & \\ \equiv [\mathbf{C^t}] \left([\mathbf{B}^+] + [\mathbf{B}^-] \right), & \end{aligned} \tag{2.31}$$

where $\mathbf{t}$ indicates the matrix transpose and $*$ the matrix complex conjugate.

Having enforced the continuity of the tangential electric field, we now enforce the continuity of the tangential magnetic field at the transition between Ω^a and Ω^b through the following set of equations:

$$\sum_m (A_m^+ - A_m^-)\vec{H}^a_{T_m}(\vec{\rho}) = \begin{cases} \sum_{p_1}(B_{p_1}^{1+} - B_{p_1}^{1-})\vec{H}^{b1}_{T_{p_1}}(\vec{\rho}), & \vec{\rho} \in \Omega^{b1}, \\ \vdots & \vdots \\ \sum_{p_q}(B_{p_q}^{1+} - B_{p_q}^{1-})\vec{H}^{bq}_{T_{p_q}}(\vec{\rho}), & \vec{\rho} \in \Omega^{bq}. \end{cases} \tag{2.32}$$

For each sub-domain q, we first take the cross product of both sides of (2.32) with $\vec{E}^{bq*}_{T_{n_q}}, n_q = 1, 2 \ldots p_q$, then take the dot product with $\hat{z}$ and integrate over Ω^{bq} to obtain:

$$\sum_m (A_m^+ - A_m^-) \underbrace{\int_{\Omega^{bq}} \vec{E}^{bq*}_{T_{n_q}} \times \vec{H}^a_{T_m} \cdot \hat{z}\, dS}_{C^{q*}_{n_q m}} = \sum_{p_q}(B_{p_q}^{q+} - B_{p_q}^{q-}) \underbrace{\int_{\Omega^{bq}} \vec{E}^{bq*}_{T_{n_q}} \times \vec{H}^{bq}_{T_{p_q}} \cdot \hat{z}\, dS}_{Y^{bq}_{n_q p_q}}. \tag{2.33}$$

In the case where Ω^{bq} is filled with a homogeneous medium, the transverse fields $\vec{E}^{bq}_{T_{p_q}}$ and $\vec{H}^{bq}_{T_{p_q}}$ are related by

$$\vec{H}^{bq}_{T_{p_q}} = Y^{bq}_{p_q} \hat{z} \times \vec{E}^{bq}_{T_{p_q}}, \tag{2.34}$$

where $Y^{bq}_{p_q}$ is the admittance of mode p_q in sub-domain Ω^{bq} given by

$$Y^{bq}_{p_q} = \begin{cases} \frac{\gamma^{bq}_{1p_q}}{j\omega\mu^{bq}}, & \text{TE}, \\ \frac{j\omega\epsilon^{bq}}{\gamma^{bq}_{2p_q}}, & \text{TM}. \end{cases} \tag{2.35}$$

The additional subscripts $_1$ and $_2$ in γ^{bq} designate TE and TM modes, respectively. Utilizing (2.34) and the orthonormal condition

$$\int_{\Omega^{bq}} \vec{E}^{bq*}_{T_{n_q}} \cdot \vec{E}^{bq}_{T_{p_q}}\, dS = \delta_{n_q p_q}, \tag{2.36}$$

the integrals in (2.33) reduce to the complex conjugate of (2.25) and

$$Y^{bq}_{n_q p_q} = Y^{bq}_{n_q} \int_{\Omega^{bq}} \vec{E}^{bq*}_{T_{n_q}} \cdot \vec{E}^{bq}_{T_{p_q}} \, dS = Y^{bq}_{n_q} \delta_{n_q p_q}. \tag{2.37}$$

Let

$$\mathbf{Y^{bq}} = \begin{bmatrix} Y^{bq}_1 & 0 & 0 \\ 0 & \ddots & 0 \\ 0 & 0 & Y^{bq}_{p_q} \end{bmatrix}, \tag{2.38}$$

and making use of (2.28) and (2.29), the combined equations of (2.33) for all q sub-domains form a matrix equation:

$$\begin{aligned} \begin{bmatrix} \mathbf{C^*_1} \\ \vdots \\ \mathbf{C^*_q} \end{bmatrix} (\mathbf{A}^+ - \mathbf{A}^-) &\equiv [\mathbf{C}^*] \left(\mathbf{A}^+ - \mathbf{A}^-\right) \\ &= \begin{bmatrix} \mathbf{Y^{b1}} & \mathbf{0} & \mathbf{0} \\ \mathbf{0} & \ddots & \mathbf{0} \\ \mathbf{0} & \mathbf{0} & \mathbf{Y^{bq}} \end{bmatrix} \left(\begin{bmatrix} \mathbf{B^+_1} \\ \vdots \\ \mathbf{B^+_q} \end{bmatrix} - \begin{bmatrix} \mathbf{B^-_1} \\ \vdots \\ \mathbf{B^-_q} \end{bmatrix} \right) \\ &\equiv [\mathbf{Y^b}]([\mathbf{B}^+] - [\mathbf{B}^-]). \end{aligned} \tag{2.39}$$

It is seen from the above that overlap integrals are necessary for the MM procedure; they are calculated either analytically (see Appendix B.2) or numerically using FEM.

2.2.1 Transition EGSM Formulations

Collecting the two most important equations (2.31) and (2.39) from the previous section, we obtain two matrix equations which relate the field amplitudes of all the modes on either side of the transition:

$$\left(\mathbf{Y^{a^*}} - \mathbf{Y^{s^t}}\right) \mathbf{A}^+ + \left(\mathbf{Y^{a^*}} + \mathbf{Y^{s^t}}\right) \mathbf{A}^- = \mathbf{C^t} \left(\mathbf{B}^+ + \mathbf{B}^-\right), \tag{2.40}$$

$$\mathbf{C}^* \left(\mathbf{A}^+ - \mathbf{A}^-\right) = \mathbf{Y^b}(\mathbf{B}^+ - \mathbf{B}^-). \tag{2.41}$$

Equations (2.40) and (2.41) are rearranged according to the standard S-matrix convention to give,

$$\underbrace{\begin{bmatrix}\mathbf{A}^- \\ \mathbf{B}^+\end{bmatrix}}_{\text{away from the transition}} = \begin{bmatrix}\mathbf{S}_{\mathbf{11}}^{\mathbf{ab}} & \mathbf{S}_{\mathbf{12}}^{\mathbf{ab}} \\ \mathbf{S}_{\mathbf{21}}^{\mathbf{ab}} & \mathbf{S}_{\mathbf{22}}^{\mathbf{ab}}\end{bmatrix} \underbrace{\begin{bmatrix}\mathbf{A}^+ \\ \mathbf{B}^-\end{bmatrix}}_{\text{towards the transition}}. \tag{2.42}$$

We obtain $\mathbf{S}_{\mathbf{11}}^{\mathbf{ab}}$ and $\mathbf{S}_{\mathbf{12}}^{\mathbf{ab}}$ by solving for $\mathbf{B}^+$ in (2.41) and substituting the results into (2.40); similarly, $\mathbf{S}_{\mathbf{21}}^{\mathbf{ab}}$ and $\mathbf{S}_{\mathbf{22}}^{\mathbf{ab}}$ are obtained by solving for $\mathbf{A}^+$ in (2.40) and substituting the results into (2.41). Collectively the blocks of the resulting EGSM for the transition are given by:

$$\mathbf{S}_{\mathbf{11}}^{\mathbf{ab}} = -\mathbf{D}_{\mathbf{R}}\left[\mathbf{Y}^{\mathbf{a}^*} - \mathbf{Y}^{\mathbf{s}^{\mathbf{t}}} - \mathbf{C}^{\mathbf{t}}\mathbf{Y}^{\mathbf{b}^{-1}}\mathbf{C}^*\right], \tag{2.43}$$

$$\mathbf{S}_{\mathbf{12}}^{\mathbf{ab}} = \mathbf{2}\mathbf{D}_{\mathbf{R}}\mathbf{C}^{\mathbf{t}}, \tag{2.44}$$

$$\mathbf{S}_{\mathbf{21}}^{\mathbf{ab}} = \mathbf{D}_{\mathbf{T}}\mathbf{C}^*\left[\mathbf{I} + (\mathbf{Y}^{\mathbf{a}^*} + \mathbf{Y}^{\mathbf{s}^{\mathbf{t}}})^{-\mathbf{1}}(\mathbf{Y}^{\mathbf{a}^*} - \mathbf{Y}^{\mathbf{s}^{\mathbf{t}}})\right], \tag{2.45}$$

$$\mathbf{S}_{\mathbf{22}}^{\mathbf{ab}} = \mathbf{D}_{\mathbf{T}}\left[\mathbf{Y}^{\mathbf{b}} - \mathbf{C}^*(\mathbf{Y}^{\mathbf{a}^*} + \mathbf{Y}^{\mathbf{s}^{\mathbf{t}}})^{-\mathbf{1}}\mathbf{C}^{\mathbf{t}}\right], \tag{2.46}$$

and

$$\mathbf{D}_{\mathbf{R}} = \left[\mathbf{Y}^{\mathbf{a}^*} + \mathbf{Y}^{\mathbf{s}^{\mathbf{t}}} + \mathbf{C}^{\mathbf{t}}\mathbf{Y}^{\mathbf{b}^{-1}}\mathbf{C}^*\right]^{-\mathbf{1}}, \tag{2.47}$$

$$\mathbf{D}_{\mathbf{T}} = \left[\mathbf{Y}^{\mathbf{b}} + \mathbf{C}^*(\mathbf{Y}^{\mathbf{a}^*} + \mathbf{Y}^{\mathbf{s}^{\mathbf{t}}})^{-\mathbf{1}}\mathbf{C}^{\mathbf{t}}\right]^{-\mathbf{1}}. \tag{2.48}$$

In the case where $Z_s = 0$ (PEC) and $\Omega^b = \{\Omega^{b1}\}$ (simple periodic), (2.43)-(2.46) reduce to eq. (6.12) of [41] with $\mathbf{Q}^{\mathbf{a}} \propto \mathbf{Y}^{\mathbf{a}^*}$ and $\mathbf{Q}^{\mathbf{b}*} \propto \mathbf{Y}^{\mathbf{b}}$. In the beginning of this section, we had assumed $\Omega^b \subseteq \Omega^a$. If $\Omega^a \subseteq \Omega^b$, $\mathbf{S}^{\mathbf{ba}}$ is found by $\mathbf{S}_{\mathbf{11}}^{\mathbf{ba}} = \mathbf{S}_{\mathbf{22}}^{\mathbf{ab}}$, $\mathbf{S}_{\mathbf{12}}^{\mathbf{ba}} = \mathbf{S}_{\mathbf{21}}^{\mathbf{ab}}$, $\mathbf{S}_{\mathbf{21}}^{\mathbf{ba}} = \mathbf{S}_{\mathbf{12}}^{\mathbf{ab}}$ and $\mathbf{S}_{\mathbf{22}}^{\mathbf{ba}} = \mathbf{S}_{\mathbf{11}}^{\mathbf{ab}}$. However, at the transition between Ω^a and Ω^b, there is a possibility where the overlapping space $\Omega^{cq} = \Omega^a \cap \Omega^{bq}$ is a proper subset of both domains. In this case the fields in each Ω^{cq} are expanded and $\mathbf{\Omega^c}$ is first mode-matched to $\mathbf{\Omega^a}$ then separately to $\mathbf{\Omega^b}$. The resulting EGSM scattering matrices $\mathbf{S}^{\mathbf{ac}}$ and $\mathbf{S}^{\mathbf{cb}}$ are subsequently cascaded by the $\star$ operator to obtain $\mathbf{S}^{\mathbf{ab}}$.

2.2.2 Section EGSM Formulations

The section EGSM of a waveguide q having p_q modes and length z is S_{G^q}, where $S_{G^q_{11}} = S_{G^q_{22}} = 0$ and $S_{G^q_{12}} = S_{G^q_{21}} = \mathbf{diag}\{e^{-\gamma_{q_1} z}, \ldots, e^{-\gamma_{q_{p_q}} z}\}$. Let a guided-section S_G be a collection of q such waveguides sharing a pair of adjacent transition planes located z apart, then the section EGSM $S_G = \mathbf{diag}\{S_{G^1}, \ldots, S_{G^q}\}$.

2.3 Aperiodic Extension

Suppose that Ω^a is infinite in extent and is the domain of excitation. The representation of the fields as a sum of discrete modes in (2.14) and (2.15) has to be replaced by a superposition of continuous modes whose variation with x and y is proportional to $e^{-j(\alpha x+\beta y)}$, where $\alpha = k\sin\theta\cos\phi$, $\beta = k\sin\theta\sin\phi$ and k is the propagation constant. Because Ω^{bq} is no longer periodic, the transverse field expansions of (2.14) and (2.15) at $z = 0$ now take the form

$$\vec{E}^a_T(\vec{\rho}, 0) = \iint_{-\infty}^{+\infty} (A^+_{\alpha,\beta} + A^-_{\alpha,\beta})\vec{E}^a_T(\alpha, \beta)d\alpha d\beta, \tag{2.49}$$

$$\vec{H}^a_T(\vec{\rho}, 0) = \iint_{-\infty}^{+\infty} (A^+_{\alpha,\beta} - A^-_{\alpha,\beta})\vec{H}^a_T(\alpha, \beta)d\alpha d\beta, \tag{2.50}$$

and are essentially the two-dimensional Inverse Fourier Transform (IFT) representation of the continuous spatial vector functions $\vec{E}^a_T(\vec{\rho})$ and $\vec{H}^a_T(\vec{\rho})$. Instead of discretizing the above integrals right away, we first expand $A^{\pm}_{\alpha,\beta}$ into the following:

$$A^{\pm}_{\alpha,\beta} = \sum_d A^{\pm}_d \delta(\alpha - \alpha_d)\delta(\beta - \beta_d) + A'^{\pm}_{\alpha,\beta}, \tag{2.51}$$

where (α_d, β_d) correspond to directions of plane waves of amplitudes $A^{\pm}_d$, while $A'^{\pm}_{\alpha,\beta}$ contain no delta-function singularities. Substituting (2.51) into (2.49) and

(2.50) and using the sifting property of the delta functions we obtain:

$$\begin{aligned}\vec{E}_T^a(\vec{\rho}) =& \sum_d (A_d^+ + A_d^-)\vec{E}_T^a(\alpha_d, \beta_d) \\ &+ \iint_{-\infty}^{+\infty} (A'^+_{\alpha,\beta} + A'^-_{\alpha,\beta})\vec{E}_T^a(\alpha,\beta)d\alpha d\beta, \qquad (2.52)\\ \vec{H}_T^a(\vec{\rho}) =& \sum_d (A_d^+ - A_d^-)\vec{H}_T^a(\alpha_d, \beta_d) \\ &+ \iint_{-\infty}^{+\infty} (A'^+_{\alpha,\beta} - A'^-_{\alpha,\beta})\vec{H}_T^a(\alpha,\beta)d\alpha d\beta. \qquad (2.53)\end{aligned}$$

Enforcing the continuity of tangential electric fields (including metal losses) at the transition between Ω^a and Ω^b:

$$\vec{E}_T^a(\vec{\rho}) = \begin{cases} \sum_q \sum_{p_q} (B_{p_q}^{q+} + B_{p_q}^{q-})\vec{E}_{T_{pq}}^{bq}(\vec{\rho}), & \vec{\rho} \in \Omega^{bq}, \\ \pm Z_s \hat{z} \times \vec{H}_T^a(\vec{\rho}), & \vec{\rho} \in \Omega^a - \Omega^b. \end{cases} \qquad (2.54)$$

Substituting (2.52) and (2.53) into (2.54), we first take the cross-product of both sides with $\vec{H}_T^{a*}(\alpha', \beta')$, and then take the dot product with $\hat{z}$ and integrate over Ω^a to obtain:

$$\begin{aligned}&\sum_d (A_d^+ + A_d^-) \underbrace{\int_{\Omega^a} \vec{E}_T^a(\alpha_d, \beta_d) \times \vec{H}_T^{a*}(\alpha', \beta') \cdot \hat{z}\, dS}_{Y_d^{a*}} \\ &+ \iint_{-\infty}^{+\infty} (A'^+_{\alpha,\beta} + A'^-_{\alpha,\beta}) Y'^{a*} d\alpha d\beta \\ =& \sum_q \sum_{p_q} (B_{p_q}^{q+} + B_{p_q}^{q-}) \underbrace{\int_{\Omega^{bq}} \vec{E}_{T_{pq}}^{bq}(\vec{\rho}) \times \vec{H}_T^{a*}(\alpha', \beta') \cdot \hat{z}\, dS}_{C'^q_{pq,\alpha',\beta'}} \\ &+ \underbrace{\int_{\Omega^a - \Omega^b} (\mp Z_s) \vec{H}_T^a(\vec{\rho}) \cdot \vec{H}_T^{a*}(\alpha', \beta')\, dS}_{Q}, \qquad (2.55)\end{aligned}$$

where

$$Y'^{a*} = \int_{\Omega^a} \vec{E}_T^a(\alpha, \beta) \times \vec{H}_T^{a*}(\alpha', \beta') \cdot \hat{z}\, dS. \qquad (2.56)$$

Although $Y_d^{a^*}$ and Y'^{a^*} depend on (α_d, β_d) and (α', β'), this dependence has been suppressed to simplify notation.

In the case where Ω^a is filled with a homogeneous medium, the transverse fields $\vec{E}_T^{a*}$ and $\vec{H}_T^{a*}$ are related by

$$\vec{H}_T^{a*}(\alpha', \beta') = Y_{\alpha',\beta'}^{a*} \hat{z} \times \vec{E}_T^{a*}(\alpha', \beta'), \tag{2.57}$$

where $Y_{\alpha',\beta'}^a$ is the wave admittance. Utilizing (2.57), the integrals in (2.55) reduce to:

$$Y_d^{a*} = 4\pi^2 Y_{\alpha',\beta'}^{a*} \delta(\alpha_d - \alpha')\delta(\beta_d - \beta'), \tag{2.58}$$

$$Y'^{a*} = 4\pi^2 Y_{\alpha',\beta'}^{a*} \delta(\alpha - \alpha')\delta(\beta - \beta'), \tag{2.59}$$

$$C'^q_{p_q,\alpha',\beta'} = Y_{\alpha',\beta'}^{a*} \int_{\Omega^{bq}} \vec{E}^{bq}_{T_{pq}}(\vec{\rho}) \cdot \vec{E}_T^{a*}(\alpha', \beta')\, dS, \tag{2.60}$$

$$Q = \sum_d (A_d^+ - A_d^-) Q_d^s + \iint_{-\infty}^{+\infty} (A'^+_{\alpha,\beta} - A'^-_{\alpha,\beta}) Q^s d\alpha d\beta, \tag{2.61}$$

where, for $\Delta\Omega = \Omega^a - \Omega^b$,

$$Q_d^s = Y_{\alpha_d,\beta_d}^a Y_{\alpha',\beta'}^{a*} \int_{\Delta\Omega} (\mp Z_s) \vec{E}_T^a(\alpha_d, \beta_d) \cdot \vec{E}_T^{a*}(\alpha', \beta')\, dS, \tag{2.62}$$

$$Q^s = Y_{\alpha,\beta}^a Y_{\alpha',\beta'}^{a*} \int_{\Delta\Omega} (\mp Z_s) \vec{E}_T^a(\alpha, \beta) \cdot \vec{E}_T^{a*}(\alpha', \beta')\, dS. \tag{2.63}$$

In the case where Z_s is independent of transverse coordinates,

$$\begin{aligned} Q_d^s = {} & (\mp Z_s) Y_{\alpha_d,\beta_d}^a Y_{\alpha',\beta'}^{a*} 4\pi^2 \delta(\alpha_d - \alpha')\delta(\beta_d - \beta') \\ & \underbrace{-(\mp Z_s) Y_{\alpha_d,\beta_d}^a Y_{\alpha',\beta'}^{a*} \int_{\Omega^b} \vec{E}_T^a(\alpha_d, \beta_d) \cdot \vec{E}_T^{a*}(\alpha', \beta')\, dS}_{Y_d'^s}, \end{aligned} \tag{2.64}$$

$$\begin{aligned} Q^s = {} & (\mp Z_s) Y_{\alpha,\beta}^a Y_{\alpha',\beta'}^{a*} 4\pi^2 \delta(\alpha - \alpha')\delta(\beta - \beta') \\ & \underbrace{-(\mp Z_s) Y_{\alpha,\beta}^a Y_{\alpha',\beta'}^{a*} \int_{\Omega^b} \vec{E}_T^a(\alpha, \beta) \cdot \vec{E}_T^{a*}(\alpha', \beta')\, dS}_{Y'^s}. \end{aligned} \tag{2.65}$$

Matching coefficients of $\delta(\alpha_d - \alpha')\delta(\beta_d - \beta')$ on both sides of (2.55) results in:

$$A_d^- = \frac{(\mp Z_s) Y_{\alpha_d,\beta_d}^a - 1}{(\mp Z_s) Y_{\alpha_d,\beta_d}^a + 1} A_d^+ \equiv \Gamma_{\alpha_d,\beta_d} A_d^+. \tag{2.66}$$

The part of equation (2.55) not involving delta functions is:

$$Y'^{a*}\left(A'^{+}_{\alpha',\beta'}+A'^{-}_{\alpha',\beta'}\right)= \sum_q\sum_{p_q}(B^{q+}_{p_q}+B^{q-}_{p_q})C'^{q}_{p_q,\alpha',\beta'}+\sum_d(A^+_d-A^-_d)Y'^{s}_d + \iint_{-\infty}^{+\infty}(A'^{+}_{\alpha,\beta}-A'^{-}_{\alpha,\beta})Y'^{s}d\alpha d\beta. \quad (2.67)$$

Having enforced the continuity of the tangential electric field, we now enforce the continuity of the tangential magnetic field at the transition between Ω^a and Ω^b through the following set of equations:

$$\vec{H}^a_T(\vec{\rho})=\begin{cases}\sum_{p_1}(B^{1+}_{p_1}-B^{1-}_{p_1})\vec{H}^{b1}_{T_{p_1}}(\vec{\rho}), & \vec{\rho}\in\Omega^{b1},\\ \vdots & \vdots\\ \sum_{p_q}(B^{1+}_{p_q}-B^{1-}_{p_q})\vec{H}^{bq}_{T_{pq}}(\vec{\rho}), & \vec{\rho}\in\Omega^{bq}.\end{cases} \quad (2.68)$$

For each sub-domain q, we first take the cross product of both sides of (2.68) with $\vec{E}^{bq*}_{T_{n_q}}, n_q=1,2\ldots p_q$, then take the dot product with $\hat{z}$ and integrate over Ω^{bq} to obtain:

$$\sum_m(A^+_d-A^-_d)\underbrace{\int_{\Omega^{bq}}\vec{E}^{bq*}_{T_{n_q}}\times\vec{H}^a_T(\alpha_d,\beta_d)\cdot\hat{z}\,dS}_{C^{q*}_d} + \iint_{-\infty}^{+\infty}(A'^{+}_{\alpha,\beta}-A'^{-}_{\alpha,\beta})\underbrace{\int_{\Omega^{bq}}\vec{E}^{bq*}_{T_{n_q}}\times\vec{H}^a_T(\alpha,\beta)\cdot\hat{z}\,dS}_{C^{q*}_{n_q,\alpha,\beta}}\,d\alpha d\beta = \sum_{p_q}(B^{q+}_{p_q}-B^{q-}_{p_q})\underbrace{\int_{\Omega^{bq}}\vec{E}^{bq*}_{T_{n_q}}\times\vec{H}^{bq}_{T_{p_q}}\cdot\hat{z}\,dS}_{Y^{bq}_{n_q p_q}}. \quad (2.69)$$

In the case where Ω^{bq} is filled with a homogeneous medium, the transverse fields $\vec{E}^{bq}_T$ and $\vec{H}^{bq}_T$ are related by (2.34) and the integrals in (2.69) reduce to (2.37), the complex conjugate of (2.60) and

$$C^{q*}_{n_q,\alpha_d,\beta_d}=Y^a_{\alpha_d,\beta_d}\int_{\Omega^{bq}}\vec{E}^{bq*}_{T_{n_q}}\cdot\vec{E}^a_T(\alpha_d,\beta_d)\,dS. \quad (2.70)$$

We now apply discretization to α, β and α', β' such that the indices (m, n) represent pairs of the discretized α, β and α', β', respectively. This results in $\vec{E}^a_T(\alpha, \beta) \Rightarrow \vec{E}^a_{T_m}$ and $\vec{E}^a_T(\alpha', \beta') \Rightarrow \vec{E}^a_{T_n}$. We replace the continuum of α by N_α discrete values, chosen so as to best approximate the original integral by a Riemann sum. Similarly the range of β is discretized by N_β selected values. An appropriate choice of the largest value of discretized $|\alpha|$ and $|\beta|$ depends on the minimum scatter cross-section; small scatterers require large spectral content. The EGSM representation of (2.66), (2.67) and (2.69) is

$$\mathbf{A}^-_{\mathbf{d}} = \mathbf{\Gamma_d} \mathbf{A}^+_{\mathbf{d}}, \tag{2.71}$$

$$\begin{aligned}(\mathbf{Y'^{a^*}} - \mathbf{Y'^{s^t}})\mathbf{A'^+} + (\mathbf{Y'^{a^*}} + \mathbf{Y'^{s^t}})\mathbf{A'^-} \\ = \mathbf{C'^t}(\mathbf{B}^+ + \mathbf{B}^-) + \mathbf{Y'^{s^t}_d}(\mathbf{A}^+_{\mathbf{d}} - \mathbf{A}^-_{\mathbf{d}}),\end{aligned} \tag{2.72}$$

$$\mathbf{C'^*}(\mathbf{A'^+} - \mathbf{A'^-}) = \mathbf{Y^b}(\mathbf{B}^+ - \mathbf{B}^-) - \mathbf{C^*_d}(\mathbf{A}^+_{\mathbf{d}} - \mathbf{A}^-_{\mathbf{d}}). \tag{2.73}$$

Equations (2.71)-(2.73) are rearranged according to the standard S-matrix convention to give,

$$\begin{bmatrix} \mathbf{A}^-_{\mathbf{d}} \\ \mathbf{A'^-} \\ \mathbf{B}^+ \end{bmatrix} \equiv \underbrace{\begin{bmatrix} \mathbf{\Gamma_d} & \mathbf{0} & \mathbf{0} \\ \mathbf{R} & \mathbf{S'^{ab}_{11}} & \mathbf{S'^{ab}_{12}} \\ \mathbf{T} & \mathbf{S'^{ab}_{21}} & \mathbf{S'^{ab}_{22}} \end{bmatrix}}_{\mathbf{S^{ab}}} \begin{bmatrix} \mathbf{A}^+_{\mathbf{d}} \\ \mathbf{A'^+} \\ \mathbf{B}^- \end{bmatrix}, \tag{2.74}$$

where

$$\mathbf{S^{ab}_{21}} \equiv \mathbf{R} = \mathbf{D'_R}\left[\mathbf{C'^t Y^{b^{-1}} C^*_d} + \mathbf{Y'^{s^t}_d}\right][\mathbf{I} - \mathbf{\Gamma_d}], \tag{2.75}$$

$$\mathbf{S^{ab}_{22}} = -\mathbf{D'_R}\left[\mathbf{Y'^{a^*}} - \mathbf{Y'^{s^t}} - \mathbf{C'^t Y^{b^{-1}} C'^*}\right], \tag{2.76}$$

$$\mathbf{S^{ab}_{23}} = 2\mathbf{D'_R C'^t}, \tag{2.77}$$

$$\mathbf{S^{ab}_{31}} \equiv \mathbf{T} = \mathbf{D'_T}\left[\mathbf{C^*_d} - \mathbf{C'^*}(\mathbf{Y'^{a^*}} + \mathbf{Y'^{s^t}})^{-1}\mathbf{Y'^{s^t}_d}\right][\mathbf{I} - \mathbf{\Gamma_d}], \tag{2.78}$$

$$\mathbf{S^{ab}_{32}} = \mathbf{D'_T C'^*}\left[\mathbf{I} + (\mathbf{Y'^{a^*}} + \mathbf{Y'^{s^t}})^{-1}(\mathbf{Y'^{a^*}} - \mathbf{Y'^{s^t}})\right], \tag{2.79}$$

$$\mathbf{S^{ab}_{33}} = \mathbf{D'_T}\left[\mathbf{Y^b} - \mathbf{C'^*}(\mathbf{Y'^{a^*}} + \mathbf{Y'^{s^t}})^{-1}\mathbf{C'^t}\right], \tag{2.80}$$

and

$$\mathbf{D}'_{\mathbf{R}} = \left[\mathbf{Y}'^{\mathbf{a}^*} + \mathbf{Y}'^{\mathbf{s}^{\mathbf{t}}} + \mathbf{C}'^{\mathbf{t}}\mathbf{Y}^{\mathbf{b}^{-1}}\mathbf{C}'^{*}\right]^{-1}, \tag{2.81}$$

$$\mathbf{D}'_{\mathbf{T}} = \left[\mathbf{Y}^{\mathbf{b}} + \mathbf{C}'^{*}(\mathbf{Y}'^{\mathbf{a}^*} + \mathbf{Y}'^{\mathbf{s}^{\mathbf{t}}})^{-\mathbf{1}}\mathbf{C}'^{\mathbf{t}}\right]^{-1}. \tag{2.82}$$

The close resemblance in form of (2.76), (2.77), (2.79) and (2.80) to (2.43)-(2.46) is the key that allows us to utilize the same computation code with little alteration for both periodic and aperiodic surfaces. We have stressed this fact by utilizing the $'$ designations for variables with common names, e.g. $\mathbf{S}^{\mathbf{ab}}_{\mathbf{11}}$ in the periodic case vs. $\mathbf{S}'^{\mathbf{ab}}_{\mathbf{11}}$ in the aperiodic case, where additional assembly of $\mathbf{\Gamma_d}$, $\mathbf{R}$ and $\mathbf{T}$ is required because of the separate treatment of discrete plane-wave terms.

Chapter 3

Results

It's not that I'am so smart, it's just that I stay with problems longer.

— Albert Einstein, 1879 - 1955

3.1 Grating Comparisons

In this section we illustrate a few features of our method while providing numerical validations with existing literature. Although the discussion is about gratings, the criteria to be discussed are applicable to all aforementioned surfaces.

3.1.1 Simple Transmission Gratings

Since the discovery of extraordinary optical transmission through periodically perforated silver films with hole diameters much smaller than the wavelength of excitation [48], there has been renewed interest in the study of similar phenomena in one-dimensional periodic gratings [49]. In this section we compare our scattering results with [49] for the case of a simple $N = 1$ transmissive thick grating in the terahertz regime ($28.6 - 342.9\,\mathrm{THz}$). The geometry of the problem is given in Fig. 3.1(a), where the slit width $a = 0.3\,\mu\mathrm{m}$ is $\sim 17\%$ of the period $d = 1.75\,\mu\mathrm{m}$

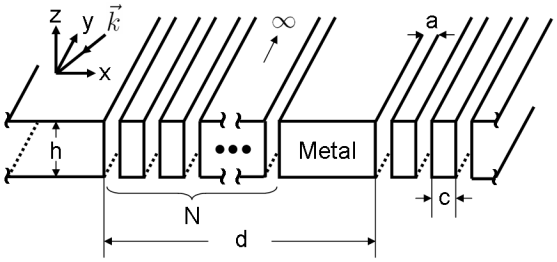

(a) A compound transmission grating with N slits per unit-cell

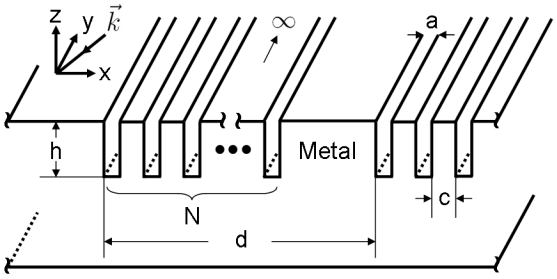

(b) A compound corrugated surface with N grooves per unit-cell

Figure 3.1: One-dimensional periodic (a) transmissive and (b) reflective surfaces where d is the period, a is the slit width, c is the slit spacing and N the number of perforations or corrugations.

and the excitation wavelength varies from $0.5d \approx 2.9a$ to $6d \approx 35a$.

Rather than repeating the observations by Garcia-Vidal *et al.*, we present a more general discussion using the EGSM methodology regarding the origin of the transmittance peak locations. Let us represent the grating problem by its equivalent EGSM representation where the first air-slit transition and the subsequent slit section are represented by $\mathbf{S^{ab}}$ and $\mathbf{S^{b}}$, respectively. To keep the discussion general, we allow $\mathbf{S^{bc}} \neq \mathbf{S^{ba}}$ for non-symmetrical connections. In the case where $\mathbf{b}$ is a simple slit section having $\mathbf{S^{b}_{11}} = \mathbf{S^{b}_{22}} = \mathbf{0}$ and $\mathbf{S^{b}_{12}} = \mathbf{S^{b}_{21}} = \mathbf{diag}\{\mathbf{e}^{-\gamma_1^{\mathbf{b}}\mathbf{h}}, \ldots \mathbf{e}^{-\gamma_n^{\mathbf{b}}\mathbf{h}}\}$, the overall EGSM $\mathbf{S^{ac}}$ is,

$$\mathbf{S^{ac}} = \mathbf{S^{ab}} \star \mathbf{S^{b}} \star \mathbf{S^{bc}}. \tag{3.1}$$

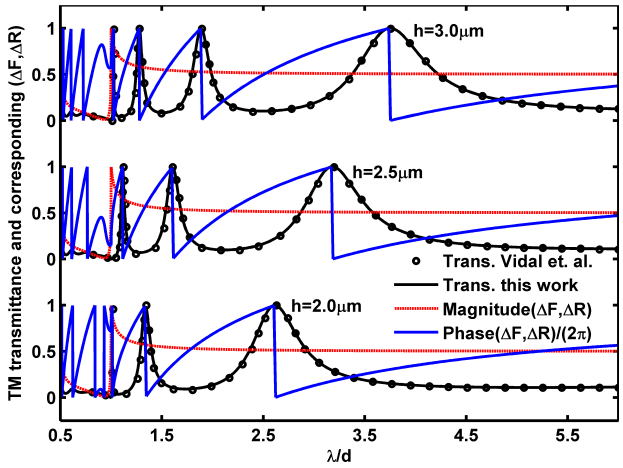

(a) TM transmittance comparisons

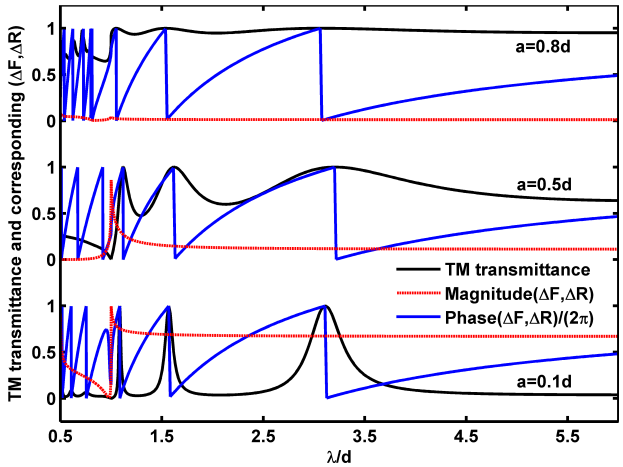

(b) Magnitude and phase of $\mathbf{\Delta_{F,R}}$

Figure 3.2: Comparisons of simulated (a) zero-order TM transmittance at normal incidence with García-Vidal *et al.* [49] as a function of λ/d for a simple ($N = 1$), thick transmission PEC grating with $d = 1.75\,\mu$m, $a = 0.3$ μm at thickness $h = \{2.0, 2.5, 3.0\}\,\mu$m. The magnitude and phase of $\mathbf{\Delta_{F,R}}$ for the fundamental slit-mode is displayed together showing that jumps of 2π in the phase of $\mathbf{\Delta_{F,R}}$ correspond to the transmittance peaks whenever $|\mathbf{\Delta_{F,R}}| \geq 0.5$ for $a/d \approx 1/6$. (b) shows that the Q of the resonances decreases for large a/d and resonance peak locations are insensitive to a/d for $h = 2.5\,\mu$m.

Application of (A.2)-(A.5) from Appendix A results in:

$$\mathbf{S_{11}^{ac}} = \mathbf{S_{11}^{ab}} + \mathbf{S_{12}^{ab}}\mathbf{S_{12}^{b}}\left[\mathbf{I} - \mathbf{\Delta_R}\right]^{-1}\mathbf{S_{11}^{bc}}\mathbf{S_{21}^{b}}\mathbf{S_{21}^{ab}}, \tag{3.2}$$

$$\mathbf{S_{12}^{ac}} = \mathbf{S_{12}^{ab}}\mathbf{S_{12}^{b}}\left[\mathbf{I} - \mathbf{\Delta_R}\right]^{-1}\mathbf{S_{12}^{bc}}, \tag{3.3}$$

$$\mathbf{S_{21}^{ac}} = \mathbf{S_{21}^{bc}}\left[\mathbf{I} - \mathbf{\Delta_F}\right]^{-1}\mathbf{S_{21}^{b}}\mathbf{S_{21}^{ab}}, \tag{3.4}$$

$$\mathbf{S_{22}^{ac}} = \mathbf{S_{22}^{bc}} + \mathbf{S_{21}^{bc}}\left[\mathbf{I} - \mathbf{\Delta_F}\right]^{-1}\mathbf{S_{21}^{b}}\mathbf{S_{22}^{ab}}\mathbf{S_{12}^{b}}\mathbf{S_{12}^{bc}}, \tag{3.5}$$

where

$$\mathbf{\Delta_R} = \mathbf{S_{11}^{bc} S_{21}^{b} S_{22}^{ab} S_{12}^{b}}, \tag{3.6}$$

$$\mathbf{\Delta_F} = \mathbf{S_{21}^{b} S_{22}^{ab} S_{12}^{b} S_{11}^{bc}}, \tag{3.7}$$

and subscripts $_{\mathbf{R}}$ and $_{\mathbf{F}}$ are used to designate reverse and forward scattering channels, respectively. In the case where only the fundamental mode of the slit section is considered, i.e. $\lambda \gg a$, and the grating is symmetrical and lossless, $\mathbf{S^{bc}} = \mathbf{S^{ba}}$, and $\gamma_1 = jk_1$, (3.2)-(3.5) reduce to equations (3) and (4) of [49].

By inspecting (3.3), (3.4), (3.6) and (3.7) one can conclude that the forward and reverse transmission resonances in the specular and non-specular directions occur when

$$\angle \mathbf{\Delta_{F,R}} = \mathbf{2}\pi\ \mathbf{diag}\{\mathbf{n_1}, \ldots, \mathbf{n_m}\}, \tag{3.8}$$

where $\mathbf{n_m}$ is an integer and $_{\mathbf{m}}$ is the total number of modes in $\mathbf{\Omega_b}$. The magnitudes of the transmission resonances depend on the relative magnitudes of the numerator (non-inverse part) as compared to the denominator (inverse part) in matrix equations (3.3)-(3.4); unity transmission peaks occur when their magnitudes are equal which occur for the specular order at normal incidence when $\lambda/d > 1$, i.e. there are no grating lobes. The Q of these resonances depend on $|\mathbf{\Delta_{F,R}}|$. For example, in the case where $h = 2.0\,\mu$m, there is a sharp resonance at $\lambda/d \approx 1.011$ where $|\mathbf{\Delta_{F,R}}| \to 1$ and a broad resonance at $\lambda/d \approx 2.62$ where $|\mathbf{\Delta_{F,R}}| \approx 0.5$. Fig. 3.2(b) shows the dependence of $|\mathbf{\Delta_{F,R}}|$ on the slit-width to period ratio a/d for the case $h = 2.5\,\mu$m; large a/d leads to smaller $|\mathbf{\Delta_{F,R}}|$ and lowers the Q of the transmittance resonances. The quasi-static limit of $|\mathbf{\Delta_{F,R}}|$ approaches unity for small a/d leading to sharp resonance peaks in transmittance at wavelengths comparable to the period d. By increasing the a/d ratio, broad-band resonances can be achieved; we use this idea in Chapter 4 to reduce undesired nulls between transmittance peaks.

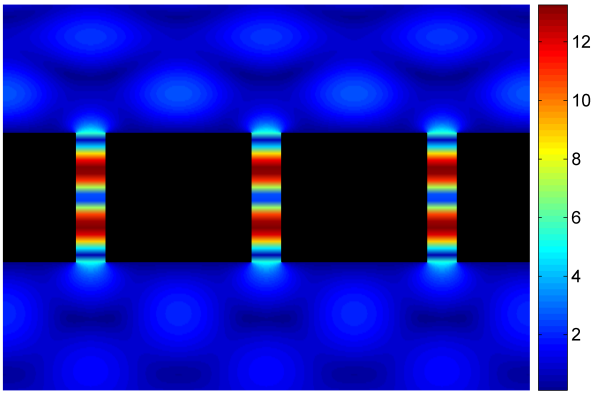

(a) $\mathbf{E_x}$ field intensity at resonance $\lambda/d \simeq 1.011$

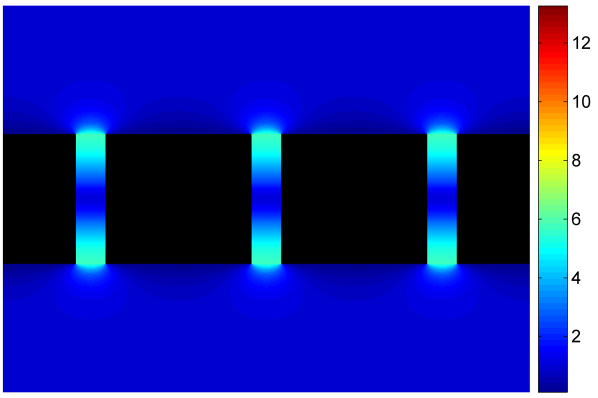

(b) $\mathbf{E_x}$ field intensity at resonance $\lambda/d \simeq 2.62$

Figure 3.3: Plot of the $\mathbf{E_x}$ field intensity over three periods of transmission gratings with geometrical parameters $d = 1.75\,\mu$m, $a = 0.3\,\mu$m, and $h = 2.0\,\mu$m. The magnitude displayed in color scale is the square root of the intensity of the total $\mathbf{E_x}$ field normalized to the incoming $\mathbf{E_x}$ field. The two figures correspond to the two resonances appearing in the transmittance spectrum (see Fig. 3.2(a)) at (a) $\lambda = 1.769\,\mu$m or $f = 169.56\,$THz and (b) $\lambda = 4.585\,\mu$m or $f = 65.43\,$THz.

Fig. 3.3 shows plots of the field intensity at two of the resonances where (3.8) are satisfied for the case of a thick-metal grating with $h = 2\ \mu\text{m} \approx 1.14d$. The high-Q resonance in Fig. 3.3(a) at $\lambda/d \simeq 1.011$ shows a 13-fold field intensity enhancement inside the slit section and field focusing above and below the metal plate in comparison to the cavity resonance at $\lambda/d \simeq 2.62$ in Fig. 3.3(b). As the grating gets thicker, more resonant peaks appear at higher frequencies while

existing peaks shift to lower frequencies (Fig. 3.2(a)) as required by the condition that the phases of the diagonal elements in (3.6)-(3.7) remain at $n2\pi$.

3.1.2 Compound Transmission Gratings

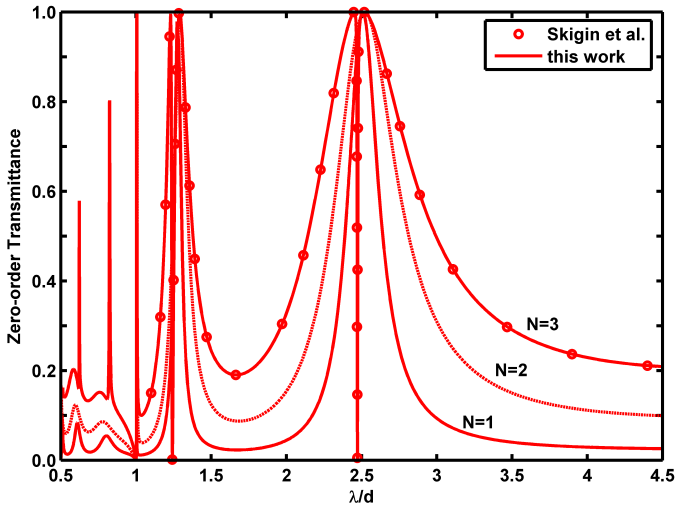

(a) Zero-order TM Transmittance

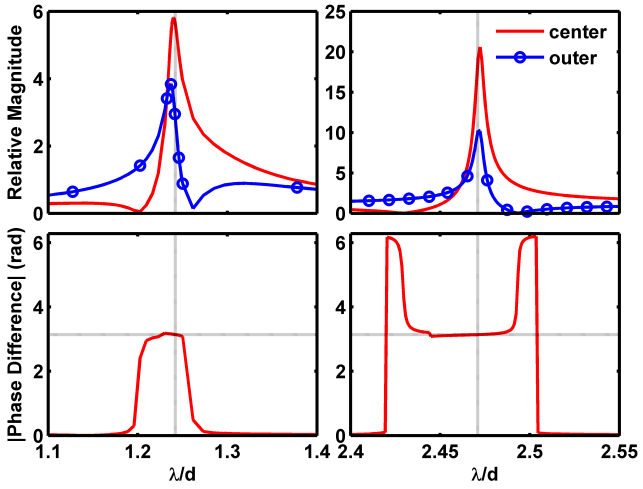

(b) Relative magnitude and phase differences between slits

Figure 3.4: Comparisons of (a) simulated zero-order TM transmittance at normal incidence with Skigin *et al.* as a function of λ/d for a compound ($N = 3$), thick transmission PEC grating with $a/d = c/d = 0.08$ and $h/d = 1.14$. $N = 1$ and $N = 2$ are included for comparison. (b) Relative magnitudes of the dominant slit modes and their phase differences in the center and outer slits at resonant anomalies near $\lambda/d = 1.242$ and 2.472.

A transmission anomaly in thick compound periodic gratings was first reported by Skigin *et al.* using the R-Matrix method [50]. In Fig. 3.4(a), we show a comparison of the transmitted intensity vs. wavelength, for a compound grating with three slits in a period [50]. The geometry of the problem is shown in Fig. 3.1(a) where $a/d = c/d = 0.08$, $N = 3$ and $h/d = 1.14$. Broad maxima at $\lambda/d \approx 1.25$ and 2.5 appear with a sharp dip in each peak. At normal incidence, symmetry dictates that the phases of the fundamental modes in the outer two slits must be equal, while that of the center slit can be different. At $\lambda/d \approx 1.242$ and 2.472, the mutual coupling between the three closely spaced slits has caused the field in the central slit to have twice the magnitude and be 180° out of phase with respect to the fields in the outer slits (Fig. 3.4(b)); the transmitted wave is then largely canceled, leading to a so-called π resonance similar to that observed in [15]. The broadening of transmission maxima (lowering of the Q) as more slits are added per period (Fig. 3.4(a)) is attributed to the increased effective a/d ratio.

3.1.3 Simple and Compound Corrugated Surfaces

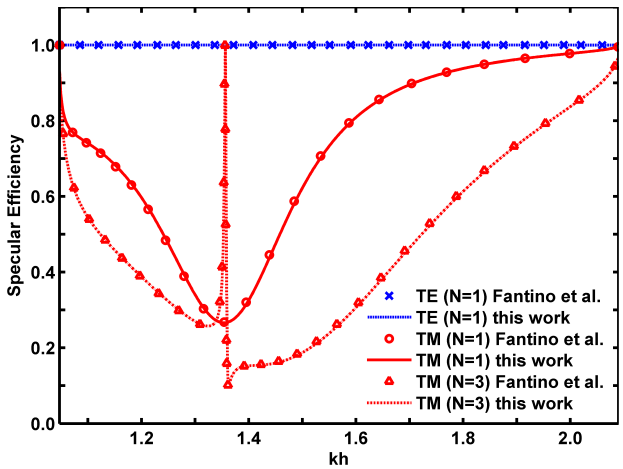

Figure 3.5: Comparisons of simulated specular efficiencies defined as $|\mathbf{S}_{\mathbf{11}}^{\mathbf{ac}}|^2$ at normal incidence with Fantino *et al.* [51] as a function of kh for $N = 1$ (simple) and $N = 3$ (compound) corrugated PEC surface where $a/h = 0.3$, $d/h = 6$ and $c/h = 0.2$.

Corrugated surfaces are essentially shorted transmission gratings. Using the EGSM methodology similar to the previous section; let $\mathbf{S^{bc}} = \mathbf{S_{11}^{bc}} = -\mathbf{I}$ represent a PEC short, then

$$\mathbf{S_{11}^{ac}} = \mathbf{S_{11}^{ab}} - \mathbf{S_{12}^{ab}}\mathbf{S_{12}^{b}}\left[\mathbf{I} - \mathbf{\Delta_R}\right]^{-1}\mathbf{S_{21}^{b}}\mathbf{S_{21}^{ab}}, \tag{3.9}$$

$$\mathbf{\Delta_R} = -\mathbf{S_{21}^{b}}\mathbf{S_{22}^{ab}}\mathbf{S_{12}^{b}}. \tag{3.10}$$

Resonance condition (3.8) requires the phases of $\mathbf{S_{21}^{b}}\mathbf{S_{22}^{ab}}\mathbf{S_{12}^{b}}$ to be odd multiples of π. In the case where phase contributions from $\mathbf{S_{22}^{ab}}$ are negligible, this phase requirement translates to a $h \approx \lambda/4$ slit section. In Fig. 3.5, we compare simulated specular efficiency vs. the slit's electrical length kh with [51]. The geometry of the problem is shown in Fig. 3.1(b) with $a/h = 0.3$, $d/h = 6$ and $c/h = 0.2$. As predicted, the dip in reflection for the case with $N = 1$ slit per unit cell occurs at $kh \approx 1.354 = \pi/2 - 0.217$. The deviation from $kh = \pi/2$ is attributed to the phase of $\mathbf{S_{22}^{ab}}$. Perfect reflection occurs at $kh \approx 1.354$ in the case of $N = 3$ slits; this is because at this frequency the field magnitude of the center slit is about twice as large and 180° out of phase with respect to the fields in the outer slits (see Fig. 3 of [51]).

One interesting result follows from (3.9): in the limit where the length of the guided-section $\mathbf{S^{b}}$ is zero, i.e. $\mathbf{S_{12}^{b}} = \mathbf{S_{21}^{b}} = \mathbf{I}$, the PEC short originally located at transition **bc** is now moved to transition **ab** and as a consequence

$$\mathbf{S_{11}^{ac}} = -\mathbf{I} = \mathbf{S_{11}^{ab}} - \mathbf{S_{12}^{ab}}\left[\mathbf{I} + \mathbf{S_{22}^{ab}}\right]^{-1}\mathbf{S_{21}^{ab}}, \tag{3.11}$$

which can be shown directly from equations (2.43)-(2.46). In the case of PEC transitions, identity (3.11) provides time reduction in computing the full EGSM matrix $\mathbf{S^{ab}}$ since only three out of four sub-EGSM matrices are independent.

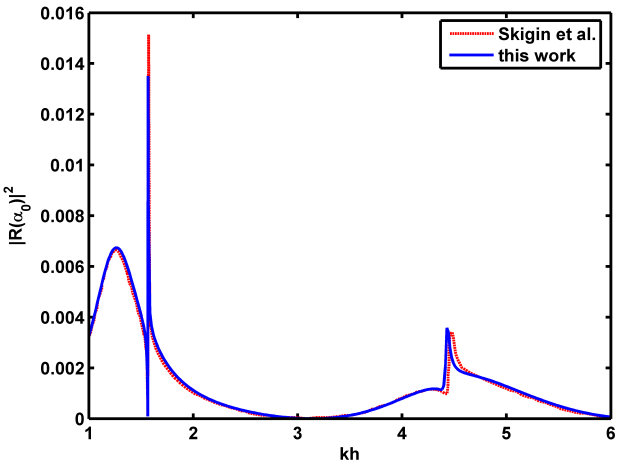

Figure 3.6: Comparisons of scattered field intensity in the normal direction $|R(\alpha_0)|^2$ with Skigin et. al. [15] as a function of kh for $N = 3$ (compound) corrugated PEC aperiodic surface where $a/h = 0.2$, $c/h = 0.1$ and $d = \infty$.

3.1.4 Aperiodic Gratings

Scattering calculations from aperiodic surfaces are much more computationally intensive than the periodic case because large EGSM matrices form as a result of fine spectral-variable discretization. Our initial simulations show promise when compared with [15] for the case of a $N = 3$ compound aperiodic corrugated PEC surface (Fig. 3.6). The high-Q resonance at $kh = 1.56936$ is attributed to the excitation of the π mode where the phase difference between the fields of the central and outer slits is π, a condition similar to that depicted in Fig. 3.2(b) for the compound periodic case where zero-transmittance occurs.

3.2 FSS Comparisons

3.2.1 Simple FSS

Design, simulation and measurement of simple thick-metal FSS's perforated by 2D periodic array of holes are covered in detail in Chapter 4.2. Due to the large amount of available literature on simple thin-metal FSS's (see for example [1]);

loss, convergence and singularity studies of simple thick-metal FSS's are discussed next.

3.2.2 Loss

Losses are important in the design of metal GT's and FSS's beyond terahertz frequencies [16]. For the purpose of validation with existing literature, the examples thus far were all simulated using PEC and loss-free dielectrics. In the EGSM formulation, metal loss at the air to metal transition is computed by enforcing the impedance boundary condition on the tangential fields (2.18) over surfaces of finite conductivity using (2.26). Wall losses inside guided sections are computed as a perturbation of the propagation constant γ for all modes using standard methods [52] (See also Appendix B.3). Dielectric losses are accounted for by a complex ϵ. To study how each of the aforementioned loss mechanisms affects transmittance, simulations of a thick FSS [53] with an unit cell shown in Fig. 3.7 are carried out next.

Dielectric Loss

To isolate the effect of dielectric loss ($\tan\delta \neq 0$), PEC is assumed for all metal parts of the unit cell shown in Fig. 3.7. Fig. 3.8(a) shows that the simulated attenuation in TE and TM transmittance is less than 10% for low-loss microwave dielectrics with $\tan\delta \leq 0.0020$ in the simulated frequency range. Attenuation can be as high as $\sim 50\%$ for a dielectric loss tangent of $\tan\delta = 0.0200$ and is observed to increase near resonances and decrease away from waveguide cutoff. Inspection of the TE_{11} mode attenuation constant due to dielectric loss α_d inside the circular perforation (Fig. 3.8(b)) reveals that it is higher near cutoff. Due to the relative small difference between β_d ($\tan\delta = 0.0200$) and β_0, the shift in resonant frequency of the transmittance peaks is barely noticeable. Because transmittance change or

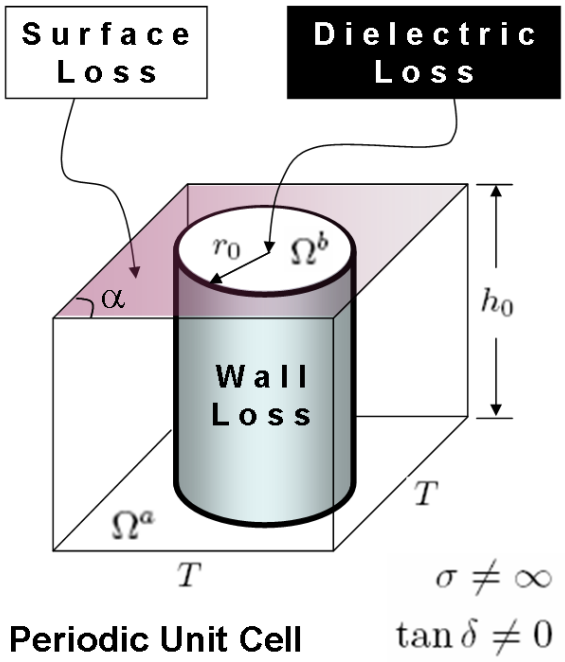

Figure 3.7: Various loss mechanisms of a thick ($h_0 = 9.24\,\text{mm}$) FSS with its unit cell consists of a cylindrical perforation filled by Parafin wax ($\epsilon_r = 2.33$). The hole radius $r_0 = 3.2639\,\text{mm}$. The lattice parameters are $T = 8.24\,\text{mm}$ and $\alpha = 60°$.

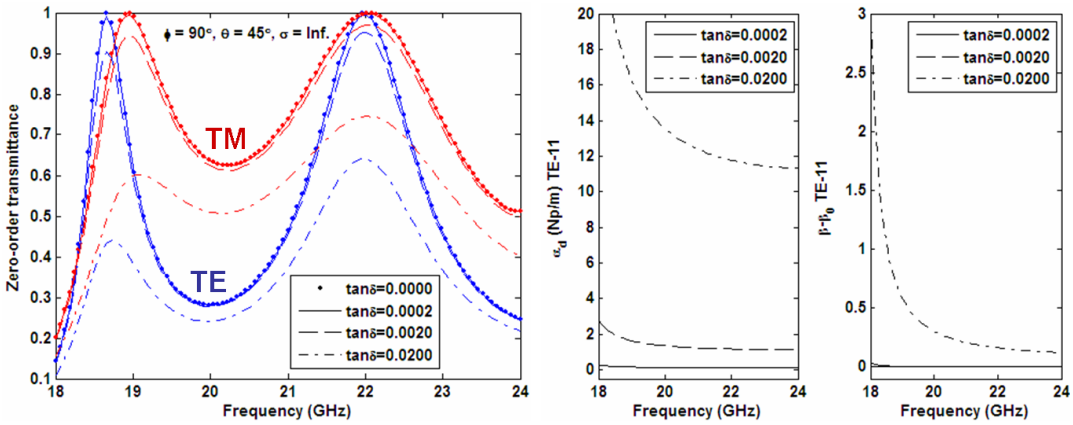

(a) (b)

Figure 3.8: (a) Simulated zero-order TE and TM transmittances at $\phi = 90°$ and $\theta = 45°$ for $\tan\delta = 0$, 0.0002, 0.0020 and 0.0200. (b) Comparison of TE_{11} mode attenuation constant α_d and the change in propagation constant $\beta_d - \beta_0$ due to dielectric loss.

attenuation for $\tan\delta \leq 0.0020$ is difficult to discern from Fig. 3.8(a), Fig. 3.9(a) shows it as $|S_{21}^{\text{ideal}}|^2 - |S_{21}^{\text{loss}}|^2$. The maximum transmittance change in the case

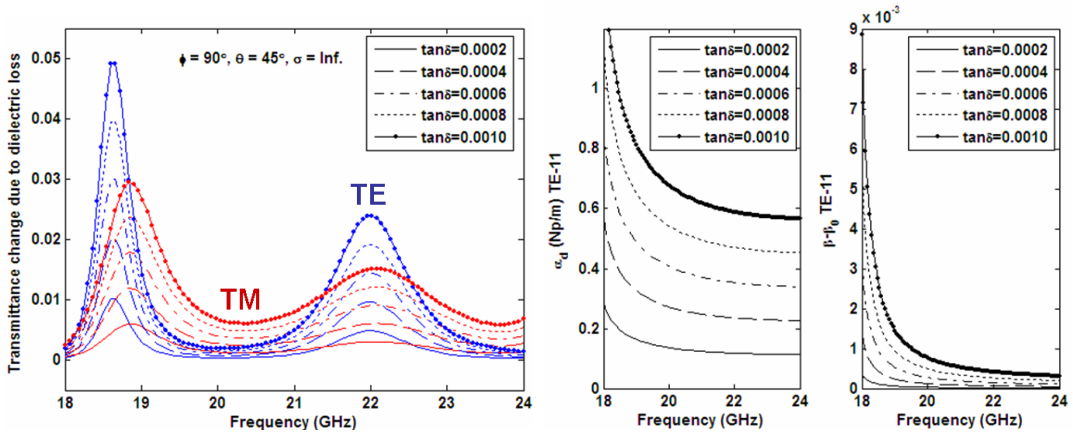

(a) (b)

Figure 3.9: (a) Simulated zero-order TE and TM transmittance change at $\phi = 90°$ and $\theta = 45°$ for $\tan\delta = 0.0002$, 0.0004, 0.0006, 0.0008 and 0.0010. (b) Comparison of TE_{11} mode attenuation constant α_d and the change in propagation constant $\beta_d - \beta_0$ due to dielectric loss.

of $\tan\delta = 0.0010$ is less than 5% for TE and 3% for TM polarized excitations, respectively. The corresponding TE_{11} mode attenuation and propagation constant changes for each variation of $\tan\delta$ are shown in Fig. 3.9(b).

Metal Loss

As a result of finite metal conductivity, loss occurs at the perforation walls (wall loss) and metal-dielectric transitions (surface loss) $\Omega^a - \Omega^b$ within the unit cell shown in Fig. 3.7. To isolate transmittance change due to metal loss, dielectric loss tangent of the filling material is set to zero. For the case of wall loss without surface loss, Fig. 3.10(a) shows that the maximum TE and TM transmittance change for silver, copper, gold and aluminum is less than 1.2%. Other than lead, transmittance changes due to finite conductivity of the perforation walls are comparable to results from low-loss dielectric fillings where $\tan\delta \leq 0.0002$ (see Fig. 3.9(a)). For lossy-dielectrics with $\tan\delta > 0.0002$, transmittance change due to dielectric loss is several times larger than those due to finite conductivity of the

perforation walls and therefore is the primary contributor to the overall loss. This is also made apparent by comparing the attenuation constant of the fundamental TE_{11} propagating mode α_d in Fig. 3.9(b) to α_c in Fig. 3.10(b). Similar to the lossy-dielectric case, the dispersion curve of the attenuation constant is responsible for the larger transmittance change near cut-off. Although the change in propagation constant $\beta_c - \beta_0$ due to finite conductivity of the perforation wall is two orders of magnitude larger than $\beta_d - \beta_0$ due to lossy dielectric fillings, its effects on the transmittance resonance location is difficult to discern because $(\beta_c - \beta_0)/\beta_0$ is small. Transmittance attenuation is larger in the case of TE than TM due to $h_z \neq 0$ which induces flow of axial directed conduction currents along the perforation walls. As the perforation wall area increases with increasing plate

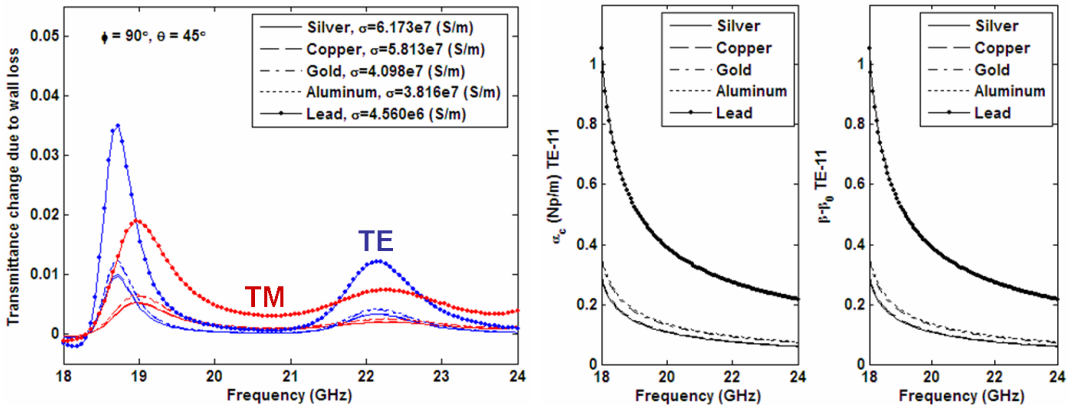

(a) (b)

Figure 3.10: (a) Simulated zero-order TE and TM transmittance change due to wall loss at $\phi = 90°$ and $\theta = 45°$ for silver, copper, gold, aluminum and lead. (b) Comparison of TE_{11} mode attenuation constant α_c and the change in propagation constant $\beta_c - \beta_0$ due to metal loss.

thickness (Fig. 3.11(a)), attenuation due to wall loss also increases (Fig. 3.11(b)). Although thickness variations does not affect propagation constant β_c, resonance frequency red-shifts as a result of the larger round-trip phase difference between aperture openings (discontinuities) on both sides of the plate (3.8).

For the case of surface loss without wall loss (i.e. the walls of the perforations

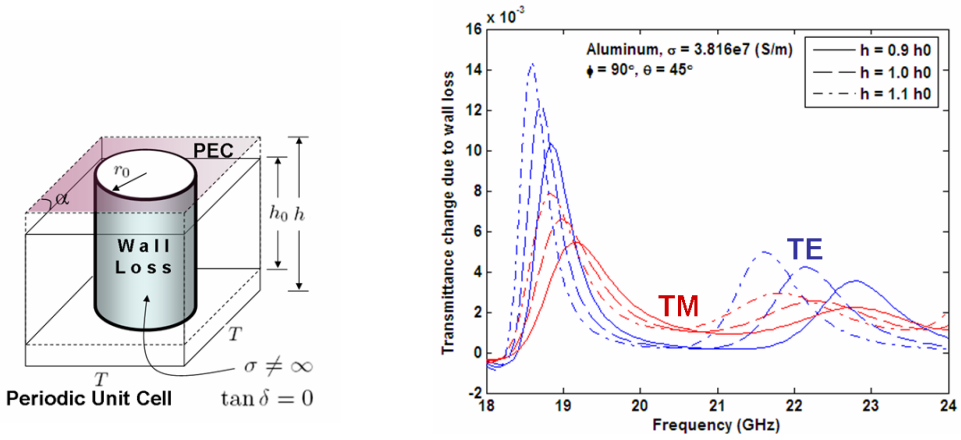

(a) (b)

Figure 3.11: (a) Geometry of a unit cell with varying thickness. (b) Simulated zero-order TE and TM transmittance change due to wall loss at $\phi = 90°$ and $\theta = 45°$ for $h = \{0.9, 1.0, 1.1\}\, h0$.

are assumed to be PEC), Fig. 3.12(a) shows that the maximum TE and TM transmittance attenuation for silver, copper, gold and aluminum is 0.06% which is 5% of the attenuation due to wall loss alone (see Fig. 3.10(a)). In the case of lead with a much lower conductivity, transmittance change due to surface loss is 5 times less than the attenuation due to low-loss dielectrics (see Fig. 3.9(a), $\tan\delta = 0.0002$). These results suggest that finite metal conductivity at transition interfaces do not contribute significantly to the overall loss at GHz frequencies in agreement with observations made by Luebbers and Munk [54]. If the unit-cell size and thickness are kept the same but the perforation radius is varied (see Fig. 3.12(b)), the resonance frequency blue-shifts and attenuation due to surface loss increases as radius decreases (Fig. 3.12(c)). Although resonance-frequency shift from radius variations is large compared to that of thickness variations (Fig. 3.11(b)), the increase in surface area as a result of a 10% decrease in radius contributes less than 0.1% to the over all attenuation.

Because time-domain spectroscopy measurements of FSS's below 0.5 THz do not show significant attenuation due to metal loss [55], simulation from 1.8 to 2.4

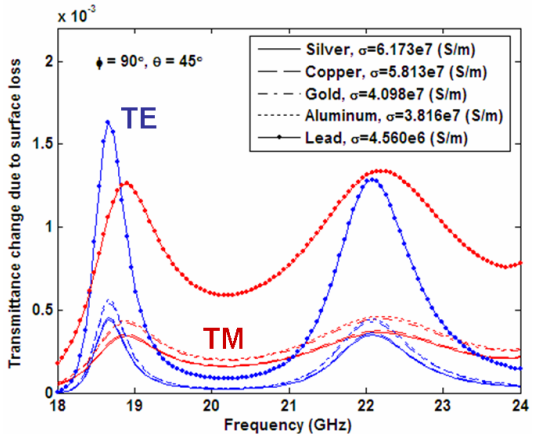

(a)

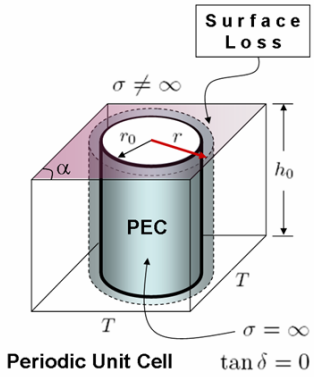

(b)

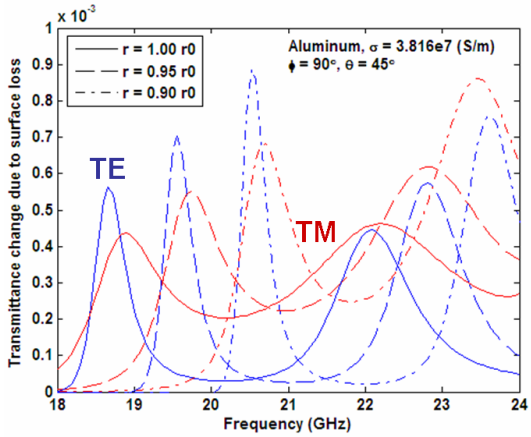

(c)

Figure 3.12: (a) Simulated zero-order TE and TM transmittance change due to surface loss at $\phi = 90°$ and $\theta = 45°$ for silver, copper, gold, aluminum and lead. (b) Geometry of a unit cell with varying radius. (c) Simulated zero-order TE and TM transmittance change due to aluminum surface loss at $\phi = 90°$ and $\theta = 45°$ for $r = \{0.90, 0.95, 1.00\}\, r0$.

THz is performed by reducing the dimensions of the unit cell shown in Fig. 3.7 by a factor of 100. In order to isolate the effect of metal loss, dielectric loss tangent is kept low at $\tan\delta = 0.0002$. Fig. 3.13 shows that attenuation due to finite conductivity of aluminum at THz frequencies is 10 times larger than attenuation at GHz frequencies.

In order to validate the theoretical formulation and the numerical implementation of the EGSM algorithm involving loss, simulation results are next compared

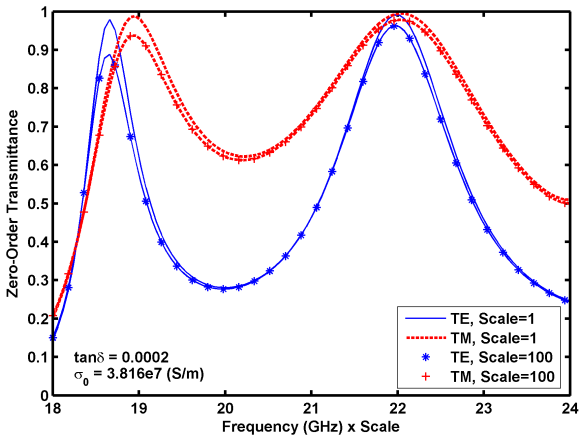

Figure 3.13: Transmittance comparison to that of a frequency scaled unit cell from $1.8 - 2.4$ THz.

with experiment. Fig. 3.14 shows that simulated transmittance including metal losses is comparable in magnitude to transmittance measured by Siegel *et al.* [56] for the case of a copper plate perforated periodically by square holes. Minor differences in spectral resonance location and curve shape are attributed to the lack of surface roughness estimation in the simulation.

3.2.3 Convergence

Convergence of modal methods in the analysis of the junction discontinuity between waveguides of arbitrary transverse cross section is known to depend on the truncation of modes used in each waveguide to represent the fields [57]. Based on the phase-synchronism principle, Veselov *et al.* [58] showed that a necessary condition for convergence requires the ratio between the number of modes used in each waveguide be comparable to the ratio between the corresponding waveguide transversal areas. Besides mode-number ratio, Il'inskii *et al.* [59] and Fa Dai [40] suggested that mode selection should be based on the closeness of the cut-off wave-numbers of the highest order modes in the two waveguides. Recently, Bhattacharrya [60] additionally pointed out that the MoM solution using the same

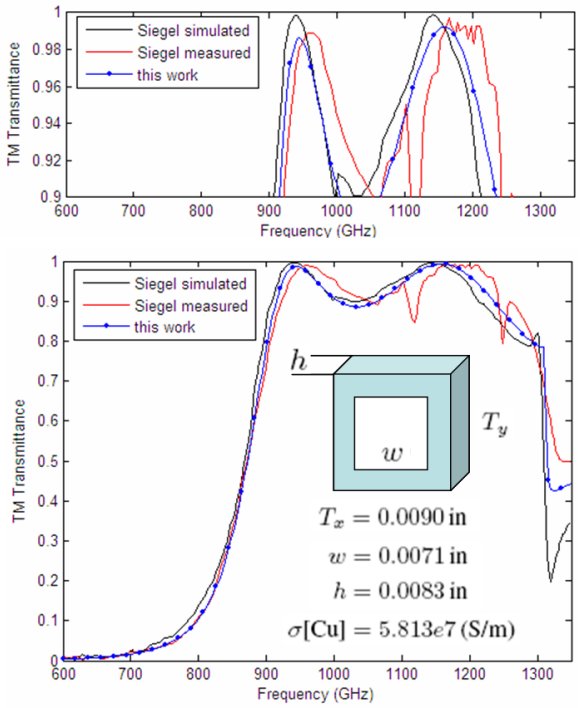

Figure 3.14: Comparison with measurements by Siegel *et al.* [56] for a thick $h = 0.0083$ in copper plate perforated periodically by square holes of width $w = 0.0071$ in in a square lattice $T_x = 0.0090$ in at normal incidence.

number of identical basis and expansion functions in the analysis of infinitely-thin strip gratings produces erroneous results.

The general consensus for acceptable MM convergence is that the mode with the highest spatial frequency content on one side of the junction determines the highest-order mode used on the other side of the junction with a comparable spatial frequency content. Because the spatial frequency content of modes in most cases is proportional to the transverse cut-off wave-number k_c, plots of the TE and TM convergence of a thick FSS at a mid-range angle of incidence of 45°, along with the maximum Floquet/waveguide $max(k_{c_{\text{fq}}})/max(k_{c_{\text{wg}}})$ mode ratio, are shown in Fig. 3.15. The difference in TM convergence behavior for $N > 2$ is due to the inclusion of the propagating TM_{11} mode in the simulation. In all cases, convergence is observed for a k_c ratio larger than 1. Only the rate of convergence

is affected (see [61]).

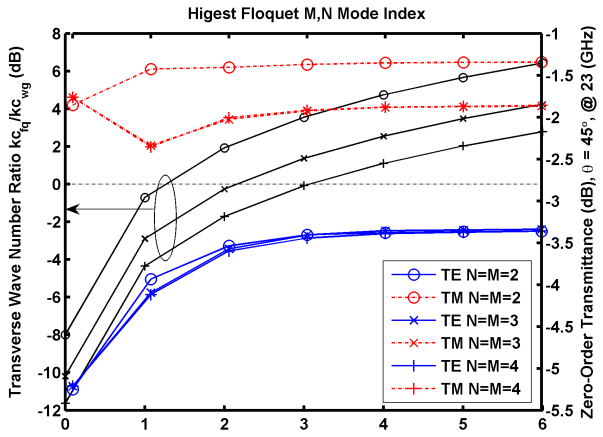

Figure 3.15: TE and TM convergence at 23 GHz for a thick ($h = 9.24$ mm) FSS with straight holes filled by parafin wax ($\epsilon_r = 2.33$). The hole radius is $r_0 = 3.2639$ mm and the lattice parameters are $b = d = 8.24$ mm and $\alpha = 60°$.

3.2.4 Singularity

Singularities can occur in simulations where zero-thickness layers are used to study infinitely-thin metal FSS's or iris discontinuities. A detailed mathematical discussion of their origin and corresponding solution is given in Appendix A.4. Example geometries where singularity is of concern are shown in Fig. 3.16. By using more modes in the field expansion of the outer waveguides than the center section, matrix singularity is avoided. Simulation results in Fig. 3.17 successfully show that scattering coefficients for Fig. 3.16(a) and Fig. 3.16(b) converge to different values in their respective geometrical limits. Because Fig. 3.16(b) reduces to a smooth waveguide in the limit, results in Fig. 3.17(b) agree with intuition. Simulations of the small iris case (Fig. 3.17(a)) are verified with circuit models using formulas given by Marcuvitz [62]. Because the circuit-equivalent model is limited in both frequency range and iris size, normalized shunt susceptance for different

frequencies over the full range of iris radii is computed from simulated S_{11} using

$$-\frac{B}{Y_0} = \frac{2jS_{11}}{1+S+11}, \tag{3.12}$$

where Y_0 is the TE_{11} mode admittance.

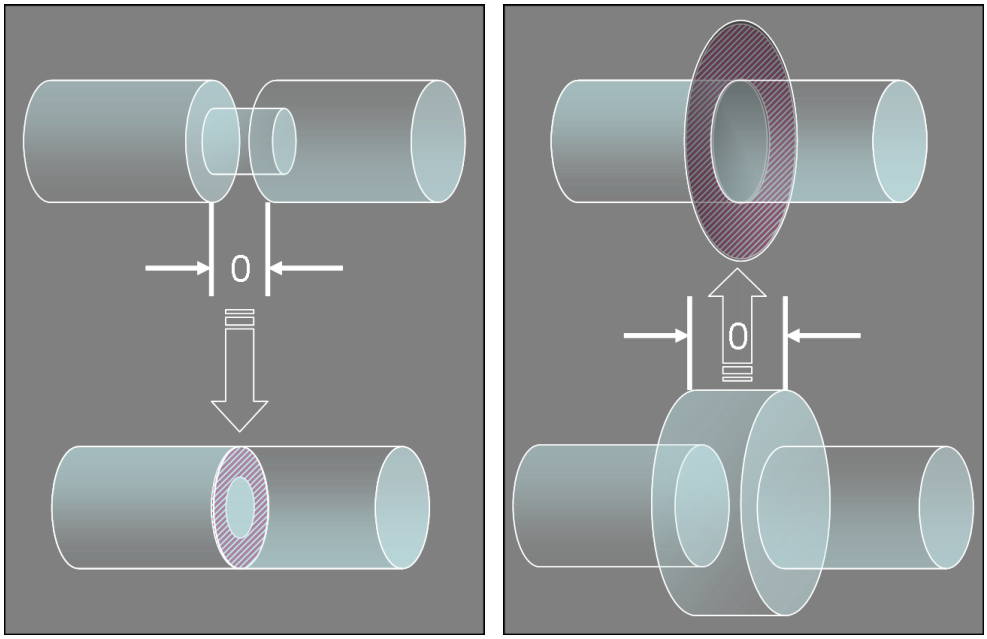

(a) (b)

Figure 3.16: (a) Infinitely-thin iris occurs as the length of the center waveguide approaches zero. (b) A smooth waveguide results as the length of the center waveguide approaches zero.

Fig. 3.18 shows that the calculated normalized shunt susceptance for each frequency using EGSM cascade compares favorably to result obtained by Scharstein *et al.* [63] using direct boundary MoM formulation. Comparisons with perturbation results by Marcuvitz [62] shows that the approximation formulas for the normalized susceptance is valid only for $b/a \leq 0.45$ and $ka \leq 2.5$. Predicted results for shunt-susceptance zero at $b/a \simeq 0.68$ and phase conjugation at $b/a \simeq 0.74$ are incorrect.

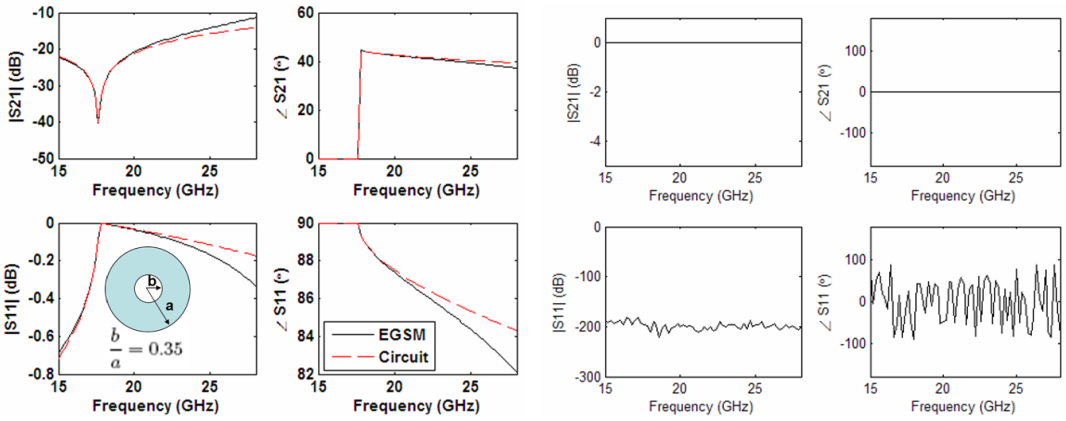

(a) (b)

Figure 3.17: (a) TE_{11} transmission and reflection coefficient comparisons with circuit approximations [62] for a cylindrical waveguide of radius $a = 3.264\,\text{mm}$ having an infinitely-thin iris of radius $b = 0.35\,a$. (b) Simulated transmission and reflection coefficients of the same cylindrical waveguide with an infinitely-thin iris of radius $b = 1.5\,a$.

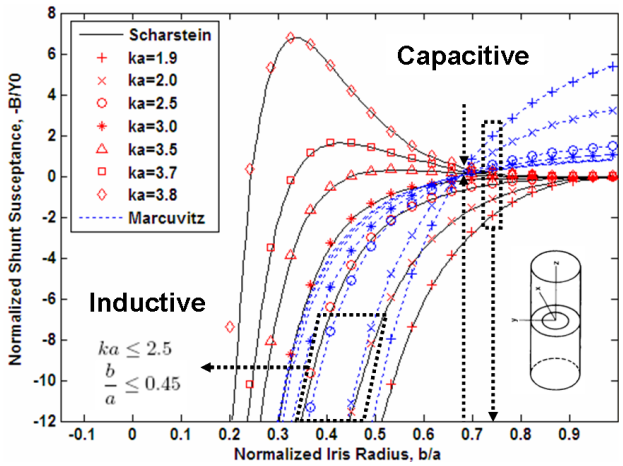

Figure 3.18: Normalized shunt-susceptance comparisons between this work (EGSM cascade (markers)), Scharstein *et al.* (direct boundary MoM [63]) and Marcuvitz (circuit equivalent via perturbation theory [62]) for infinitely-thin irises of different radii inside a cylindrical waveguide. a and b are cylindrical radii of the waveguide and iris, respectively.

3.2.5 Compound FSS

The earliest known free-space scattering analysis of the multiple aperture per unit-cell problem was done by Reed and Byrne [64] based on extensions to the method of Chen [65]. Their analysis focused on the idealized case of a perfectly-conducting,

infinitely-thin metal plate perforated with identical groups of N dissimilar rectangular apertures excited by a normally incident TE-polarized plane wave. They showed that by varying the rectangular aperture length in alternating columns, it was possible to produce narrow-band resonance peaks at longer wavelengths in addition to the expected resonance for the simple periodic case. Furthermore, the spectral location and bandwidth of the narrow-band resonances are observed to depend on relative length variations of the apertures. Fig. 3.19 shows excellent agreement between the two methods for alternating row/column configurations (see insets of Fig. 3.19(a) and Fig. 3.19(b)) of the infinitely-thin compound periodic case. In our case, equation (2.13) is applied with care so that the ratio of the number of modes in air to that of the aperture regions is suitable [60]. Good convergence was observed using 1058 Floquet modes in air and 19 waveguide modes in each aperture; the mode number ratio of ~ 55 is somewhat larger than the unit-cell to aperture area ratio ~ 36. Also included are the case where the apertures are $0.5\,\mu$m thick for each variation of $a2$; results in Fig. 3.19 show increased attenuation and frequency shift for $a1 \neq a2$.

Closer examination of field amplitudes inside adjacent apertures of the compound unit cell shown in Fig. 3.19(a) reveals that sharp resonance peaks occur whenever large differences in mode magnitudes exist out of phase with respect to each other (see Fig. 3.20). The transmittance zeros at $\lambda/d = 13.4$ ($a2 = 4.0\,\mu$m) and $\lambda/d = 13.9$ ($a2 = 4.5\,\mu$m) occur because the dominant mode magnitudes of the two adjacent apertures are the same except 180° out of phase.

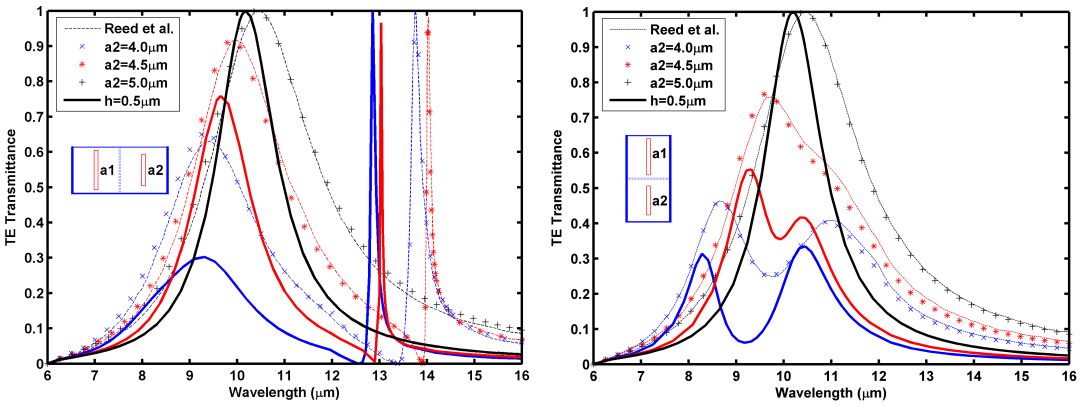

(a) (b)

Figure 3.19: Comparison between this work (markers) and Reed *et al.* (dashed lines) for alternating (a) column and (b) row unit-cell configurations of an infinitely thin compound periodic FSS. The $12\,\mu\text{m} \times 6\,\mu\text{m}$ rectangular unit-cell is filled with two rectangular apertures having the same width $0.5\,\mu\text{m}$ but of different length $a1 = 5.0\,\mu\text{m}$ and $a2$. The thick solid lines correspond to predicted results for the case where the PEC plate is $0.5\,\mu\text{m}$ thick.

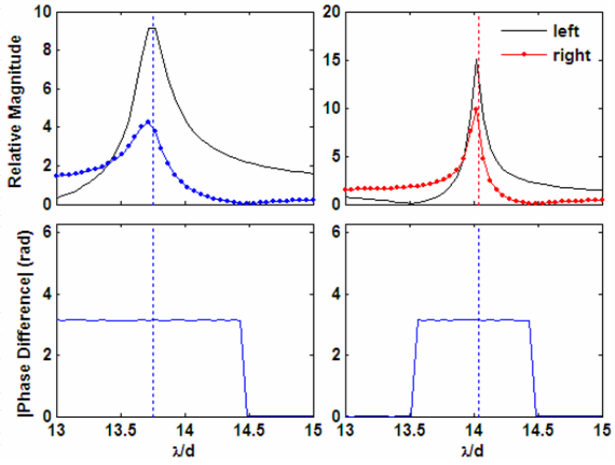

Figure 3.20: Field amplitude comparisons near sharp resonance peaks for the case $a2 = 4.0\,\mu\text{m}$ (left) and $a2 = 4.5\,\mu\text{m}$ (right) shown in Fig. 3.19(a).

Chapter 4

Application

In science the credit goes to the man who convinces the world, not to the man to whom the idea first occurs.

— Sir William Osler 1849-1919

FSS's and GT's of various shapes and sizes integrate into our modern lifestyle with such ease that their utility can sometimes be overlooked. A common example of FSS usage is in the door of a modern microwave oven where a periodically perforated thin-metal sheet embedded in dielectric passes light (high frequency) to the eye but confines the microwave (low frequency) used for cooking. These seemingly ordinary surfaces have extraordinary properties and are currently still under investigation [66]. Standard utilization of FSS's in the millimeter and sub-millimeter regimes occurs in applications related to radome engineering [67], dichroic subreflectors [3] and compact antennas [68].

Applications of GT's and FSS's at quasi-optical frequencies are discussed in detail in [69]. At these frequencies, FSS's are commonly used as a beam splitting element that spatially demultiplexes the received broadband signal from a single broadband aperture antenna and redirect it to multiple detectors according to frequency content [70]. Other applications of FSS's such as photovoltaic research

extend well into the infrared range of the spectrum [71]. Recently, the most exciting investigations has been in the area of extraordinary optical transmission [48]. A FSS lens made from stacked periodic wire arrays interconnected through phase-conjugating circuitry also produces negative refraction and sub-wavelength focusing [72].

4.1 Metal Radomes

Unlike conventional circuit filters, the transmission and reflection frequency responses of FSSs are functions of incident excitation profile, polarization and direction. Fig. 4.2(a) and Fig. 4.2(b) show simulated plane-wave excitation responses for a thick-metal FSS perforated with straight holes and filled by dielectrics; as the incidence excitation direction is varied from 0° to 75°, transmission responses shift and change shape for transverse electric (TE, E-field perpendicular to the plane of incidence) and transverse magnetic (TM, H-field perpendicular to the plane of incidence) polarized excitations. This is highly undesirable in many applications. One especially problematic situation is in sending a high-power EM beam through a thick-metal nose cone shown in Fig. 4.1.

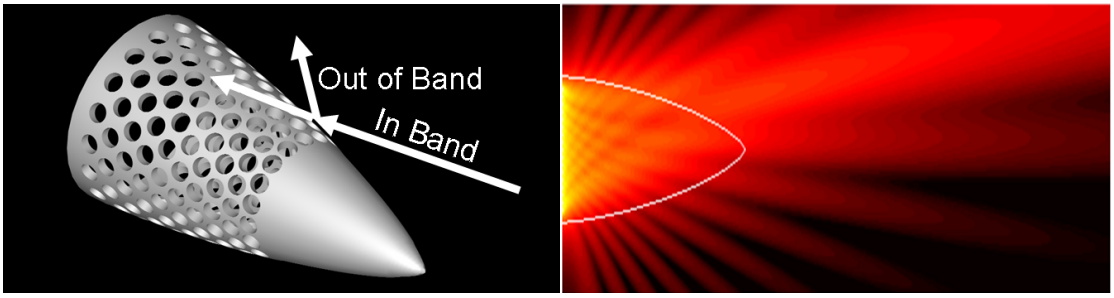

(a) Futuristic Metal Radome (b) Antenna beam passing through the radome

Figure 4.1: (a) Conceptual drawing of a futuristic metal radome allowing in-band signals to pass-through while deflecting out-of-band signals for missile or aircraft high-G nose cones. (b) The same metal radome allowing ideal transmission of a high-power spatial-scanning beam.

A thick-metal FSS surface is an appropriate choice for this application due to its superior power handling and structural strength. In addition, its filtering characteristics allow in-band signals to pass while deflecting out-of-band signals away from the observer (Fig.4.1(a)). The angle requirement of such a surface in a radome application is made evident by studying various radome cross-sections in relation to the radiator positions using the superquadric equation [73].

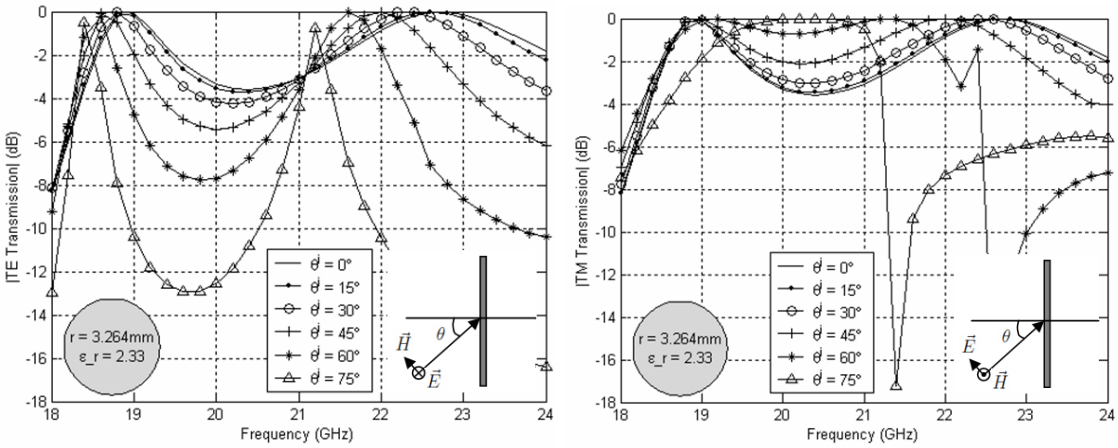

(a) TE transmittance

(b) TM transmittance

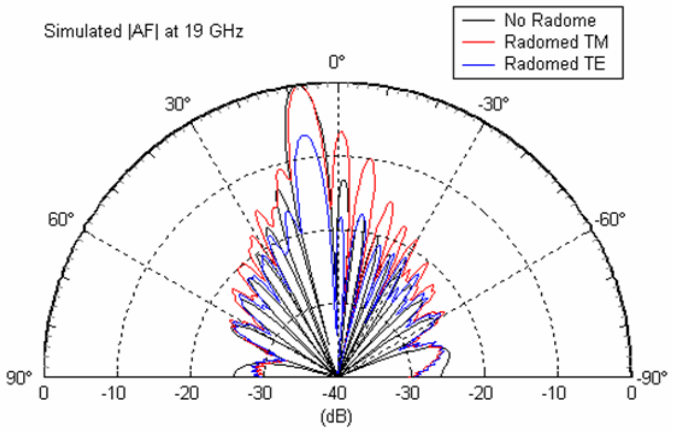

(c) Array factor at 19 GHz

Figure 4.2: Estimated effect (c) on the transmitted beam by a thick-metal FSS radome at 19 GHz. (a) and (b) are TE and TM plane-wave transmittance of a planar straight-hole thick-FSS plate as a function of incidence angle.

Geometric-optics approximation of how a thick-metal radome affects transmitted beam is shown in Fig. 4.2(c) for a Von-Karman metal nose-cone (Fig. 4.1(a))

perforated with straight holes and filled by dielectrics. The approximation uses the transmittance curves of Fig. 4.2(a) and Fig. 4.2(b) by assuming that the radome is locally planar for each incident ray. Therefore, a planar modeling tool is worth while to develop as it can be applied to conformal surfaces. Fig. 4.2(c) shows that at 19 GHz, the array factor (beam) for TE polarization is significantly different than the TM response in the presence of the radome; this is attributed to the more sensitive angle dependence of the TE response at 19 GHz (Fig.4.2(a)) as compared to the TM response (Fig.4.2(b)). Furthermore, there is an apparent change in the direction (boresight error) of the beam with respect to the case where no radome is present.

Thick surfaces with angle-stable but narrow-band responses can be achieved by adding complementary metal patches to the aperture openings [1]; however, a nominal patch radius change of ~ 0.5 mil resulted in frequency shift of more than half the transmission bandwidth. Transmission degradation due to manufacturing tolerance is a common problem in traditional multi-layered FSSs using thin-metal patterns and thick dielectrics. It is very difficult to maintain thermal coefficients between the various layers in extreme environments and to find suitable bonding materials. Since preventing metal expansion < 0.5 mil under heating is difficult, more robust designs are needed to handle high-power applications that require broad bandwidth. Initial work on thick-metal plates with special perforations having broad-band, angle and polarization stable response is shown in Section 4.3. Before going on to the design of these surfaces, it is necessary to establish a measurement technique for characterizing them.

4.2 Measurement

Due to large beam-width and far-field distance, measurements of FSS's using standard horns require the construction of large FSS panels to avoid strong edge diffractions. Precision lens and horn measurement setups can be very expensive. To save cost, a measurement technique using open-ended waveguide probes is used. A typical setup for measuring transmission responses of thick-metal FSS is shown in Fig. 4.3, where the sample under-test is mounted on a rotating platform placed in-between two open-ended waveguide probes. Because the aperture dimensions of the probes are small, their far field radius is short; this allows the probes to be placed closer to the FSS at high incidence angles and still maintain good plane-wave excitation.

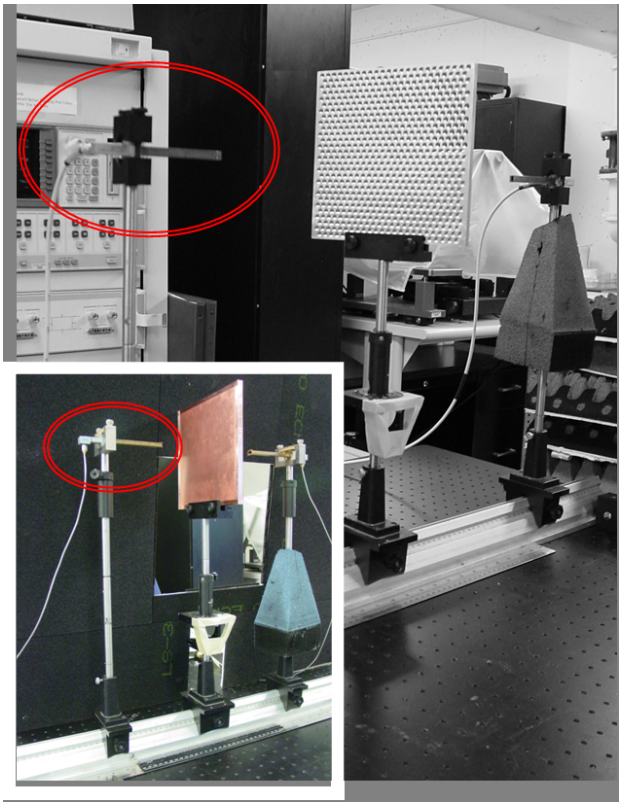

Figure 4.3: Transmission measurement setup using waveguide probes.

A simple thick K-band FSS (Fig. 4.4) is designed and constructed next so

that simulation and measurement can be compared. Circular waveguide dimensions and lattice spacing of the perforated plate are determined initially based on waveguide and array theory. Using $\epsilon = 2.24$ for paraffin wax, the diameter of the cylindrical element is calculated to be 6.5 mm by setting the cutoff frequency of the fundamental TE_{11} mode at the lower K-band band edge (18 GHz). Lattice spacing is chosen to avoid grating lobes for all scan angles ($\pm 90°$); for a hexagonal lattice this corresponds to (8.24 mm at 21 GHz). The thickness of the FSS is selected to be half the guided wavelength, which at $f = 21$ GHz and for $f_c = 18$ GHz is 9.24 mm. Using these dimensions, an aluminum plate was milled with periodic cylindrical holes and the holes were filled with melted paraffin wax. Once the plate cooled, excess wax was scraped off to produce the FSS shown in Fig. 4.4.

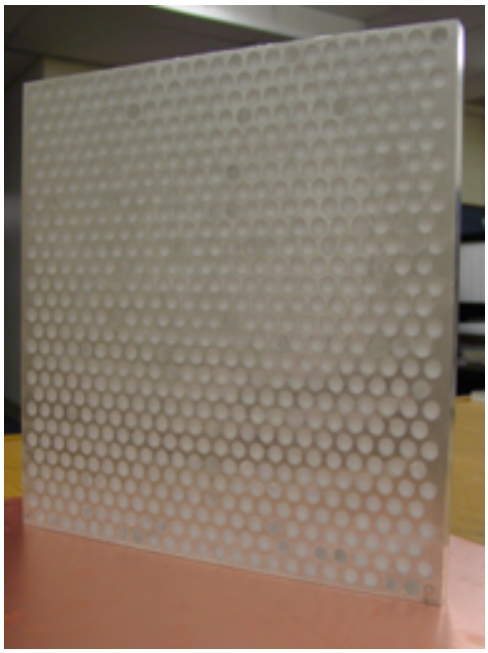

Figure 4.4: A K-band metallic FSS. 6.5 mm holes were milled in the aluminum plate in a hexagonal lattice, and filled with paraffin wax. The lattice spacing is 8.24 mm; the width and thickness of the aluminum plate are 20.32 cm and 9.24 cm, respectively.

Simulation of the structure over all scan angles for both TE and TM incidence show satisfactory convergence when mode matching 242 Floquet modes in

air to 59 waveguide modes is performed. Results in Fig. 4.2(a) and Fig. 4.2(b) show that peak transmission near normal incidence for both TE and TM cases occur at 19 GHz and 22.6 GHz, corresponding to $\lambda_g/3$ and $2\lambda_g/3$, where λ_g is the guided wavelength of the cylindrical waveguide. The TM response shifts less with frequency for incidence angles up to 60° compared to the TE response, whose transmission bandwidth narrows with increasing incidence angles.

Measurements of the FSS's K-band frequency response and scan characteristics were performed using open-ended WR-42 waveguides with added E-plane flanges (circled in Fig. 4.3) by an HP-8510C vector network analyzer. The added flanges aid in back radiation reduction by choking backward traveling currents. Measured probe radiation patterns are shown in Fig. 4.5(a). The back-radiation is at around -15 dB. More sophisticated probes can be constructed to have even lower back-radiation levels while preserving their aperture dimensions to reduce the far-field distance. Shorter far-field distance allows smaller panels to be measured with minimum diffraction effects. The optimum position of the waveguide probe is located where the surface of the FSS is tangential to the far-field sphere of the probe:

$$R_{\text{opt}} = \frac{\frac{2D^2}{\lambda} + \frac{t}{2}}{\cos(\theta^{\text{inc}}_{\text{max}})} \tag{4.1}$$

where D is the largest dimension of the probe, t is the plate thickness and $\theta^{\text{inc}}_{\text{max}}$ is the maximum incidence angle measured from the normal of the FSS. Substituting the near field distance into 4.1, minimal distance of the probe is determined. At a maximum incidence of 90° , the maximum position can be obtained by adding half of the FSS plate width ($w/2$) to the probe's far-field radius. In practice incidence angles close to 90° cannot be measured, therefore, positions calculated using the 90° incidence angle serve as indicators of the maximum distance relative to the origin of the probe placement. Beyond this distance, a large portion of

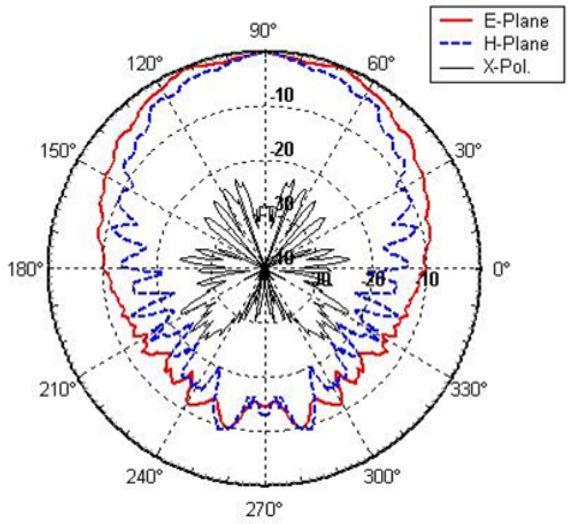

(a) Probe pattern

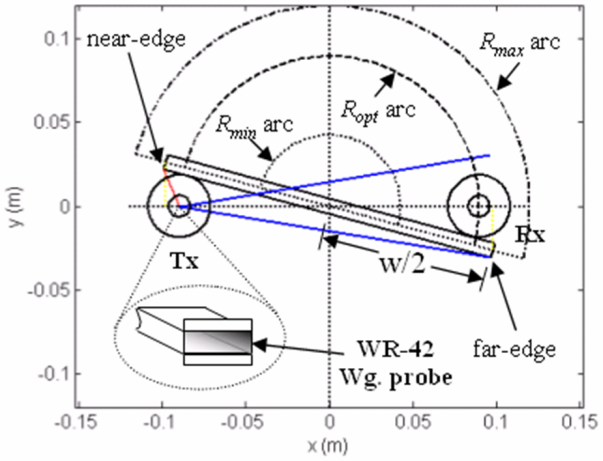

(b) Diagram of the measurement setup

Figure 4.5: (a) Measured normalized-gain radiation pattern of a WR-42 open-ended waveguide probe with $\lambda/4$ E-plane flange at 21 GHz. E and H-plane HPBW are about 30° and cross-polarization level is below -22 dB. (b) Diagram (top view) of the experimental setup at the maximum incidence angle of 75°. The circles represent the far-field and near-field boundaries of the transmitter and receiver probes at 21 GHz.

the probe's main lobe will see the near-edge of the FSS resulting in significant scattering at large incidence angles. The accuracy and simplicity of this measurement is a result of the low back-radiation of the waveguide probe. By observing the measured probe radiation pattern from Fig. 4.5(a), it can be concluded from

Fig. 4.5(b) that the diffraction from the FSS near edge is reduced as compared to its far edge due to the reduced back radiation of the probe.

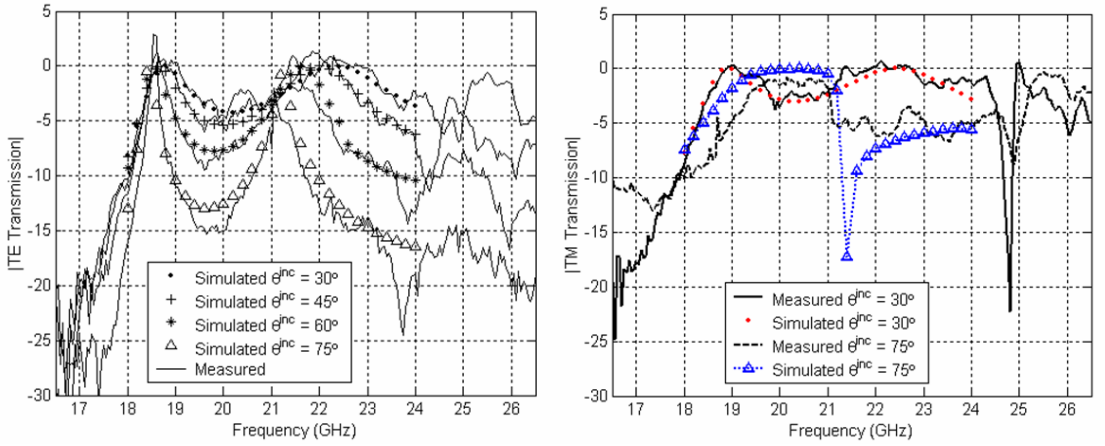

(a) Measured TE transmittance

(b) Measured TM transmittance

Figure 4.6: (a) Measured vs. simulated transmission response for TE incidence at 30°, 45° , 60° and 75°. (b) Measured vs. simulated transmission response for TM incidence at 30° and 75°.

One of the published permittivity values of paraffin at X-band, $\epsilon_r = 2.24$, was used for the initial design, but in addition to the operating frequency difference, the effects of melting are unknown. It was found that a value of $\epsilon_r = 2.33$ in the simulation agrees best with measured results shown in Fig. 4.6. Because the optimum probe location is inversely proportional to wavelength (4.1), at frequencies above 24 GHz, the probe location becomes significantly less than specified by (4.1); this causes the FSS to protrude into the far-field sphere of the probe at moderate incidence angles thus producing erroneous results. At incidence angles near 75°, the measured TE response (Fig. 4.6(a)) matches better with simulation than the TM case (Fig. 4.6(b)); this could be due to the rectangular nature of the probe. Edge absorbers and time-gating measurement techniques can be used to remove some of the ripples and overshoots in the response.

4.3 Tapered FSS

Thick-metal plates perforated by a periodic array of straight holes have multiple sharp resonances in both TE and TM transmittances at moderate angles of incidence [53]. The sharpness of these resonances limits the usable bandwidth because the transmittance peaks shift in frequency with increasing angle. In order to stabilize transmission for both polarizations and to increase the desired bandwidth, the Q of each of the resonances must be reduced. This is accomplished by increasing the ratio of the radius r_0 to the periods b and d following observations made in chapter . For thick FSSs, the dominant factors affecting the phase of $\mathbf{\Delta_{F,R}}$ in (3.8) are $\mathbf{S_{21}^b}$ and $\mathbf{S_{12}^b}$ which depend on plate thickness. Other factors in $\mathbf{\Delta_{F,R}}$, $\mathbf{S_{22}^{ab}}$ and $\mathbf{S_{11}^{bc}}$ model internal slit reflections at the aperture-air boundaries and contribute additional phase and amplitude scaling to $\mathbf{\Delta_{F,R}}$; this scaling decreases with increasing ratio a/d and lowers the Q of the resonances for the case of simple thick gratings.

In the unit cell shown in Fig. 4.7, the aperture-air boundaries of a thick, straight-hole FSS is modified by enlarging the radius of its perforation at the surface for the reason stated above. Because transmittance is dependent on metal

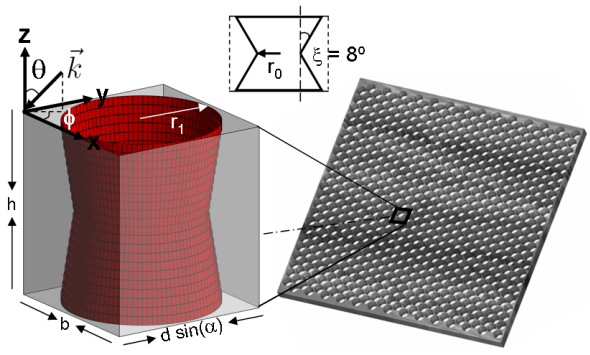

Figure 4.7: A thick ($h = 9.24\,\text{mm}$) FSS with tapered holes filled with parafin wax ($\epsilon_r = 2.33$). The hole radius tapers linearly from the outer surface where $r_1 = 3.9116\,\text{mm}$ to the plate center where $r_0 = 3.2639\,\text{mm}$ with a taper angle $\xi \approx 8°$. The lattice parameters are $b = d = 8.24\,\text{mm}$ and $\alpha = 60°$.

content (zero metal content equals perfect transmission), enlarging the aperture should provide better transmittance. In order to do this and still obtain structural integrity, the hole radius is tapered from the outer surface towards the center symmetrically from both sides of the plate. A total of 21 straight waveguide sections, each 0.44 mm thick, are used to represent the taper. Simulation is performed using 32 waveguide-modes in each section and 98 Floquet-modes in air. Comparison with measurement data is shown in Fig. 4.8. Due to the larger effective aperture, cutoff frequencies of the guided sections shifted lower in frequency and as a consequence the overall transmission response shifted down as well. However, as expected the included taper has reduced the pass-band ripple between the two dominant resonance peaks in the TE and TM responses of Fig. 4.8 by as much as 3 dB.

Because the EGSM implementation accepts a vector input of layer radii, longitudinal profiles other than the simple linear taper can be investigated. One such profile studied is given by the equation:

$$r(z) = r_1 \left(0.7 + 0.3 \left|\cos\left(\frac{\pi}{2} + \frac{\pi}{h} z\right)\right|\right), \quad -\frac{h}{2} \leq z \leq \frac{h}{2}. \tag{4.2}$$

A total of 31 straight waveguide sections, each 0.298 mm thick with $r_1 = 3.2639$ mm and $h = 9.24$ mm, are used to represent the taper shown in Fig. 4.9(a). Simulation is performed using 18 waveguide-modes in each section and 242 Floquet-modes in air. Geometry comparisons with linear taper $r_0 = 0.7\, r_1$ and straight hole $r_2 = 0.9\, r_1$ are shown in Fig. 4.9(b). Before comparing transmittance results for these three cases, it is interesting to point out that the profile described by (4.2) bares a close resemblance to the compound parabolic profiles used by Winston *et al.* [74] in the design of non-imaging solar concentrators. Because the wavelength of operation in their case is significantly less than the dimensions of the perforations, ray-tracing method was used in their analysis. The basic idea is illustrated in Fig. 4.10(a) where extreme rays at angle θ_{inc} are deflected by the linear ta-

per but are passed by the compound parabolic taper. Fig. 4.10(b) illustrates the closeness of the cosine taper to that of a truncated compound parabolic taper with a maximum transmission angle $\theta_{\max} = 45°$. Fig. 4.11 shows that in addition to reducing the pass-band ripple when compared to the straight hole, the cosine taper also produces a wider transmittance band width than the straight taper. The extension of the lower pass-band edge is due to the gradual change of cut-off frequencies of waveguide layers near the metal-air interface.

To illustrate the correctness of our implementation and the speed of the mode-matching algorithm, comparison with commercial Ansoft-HFSS FEM simulation software for the analysis of junction discontinuity between two on-axis cylindrical waveguides is performed. This analysis is representative of a single junction discontinuity in the cascade of 21 and 31 waveguide sections in the respective case of linear and cosine tapered perforations. Results in Fig. 4.12 demonstrate that good agreement between the two method is reached in the case where 120-sided polyhedrons are used to represent the cylinders in HFSS. The default straight-cylinder model in HFSS produces reflection coefficients that are frequency shifted. Our formulation is 489 and 4369 times faster in comparison to results using straight-cylinder and 120-sided polyhedron models in HFSS, respectively.

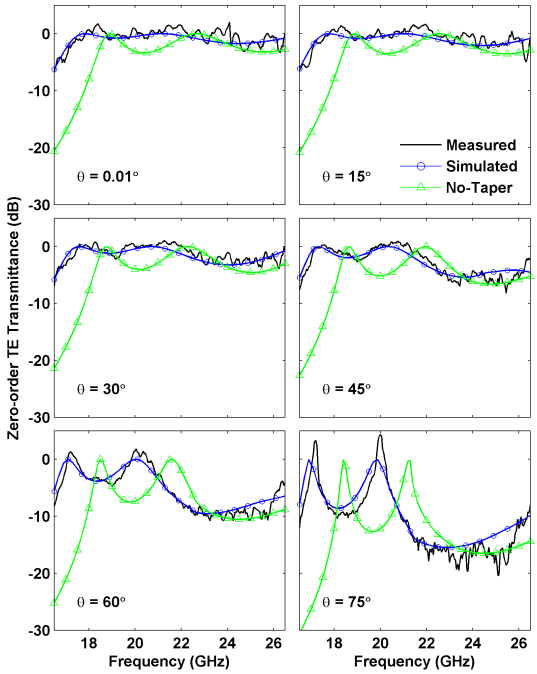

(a) Zero-order TE transmittance vs. frequency

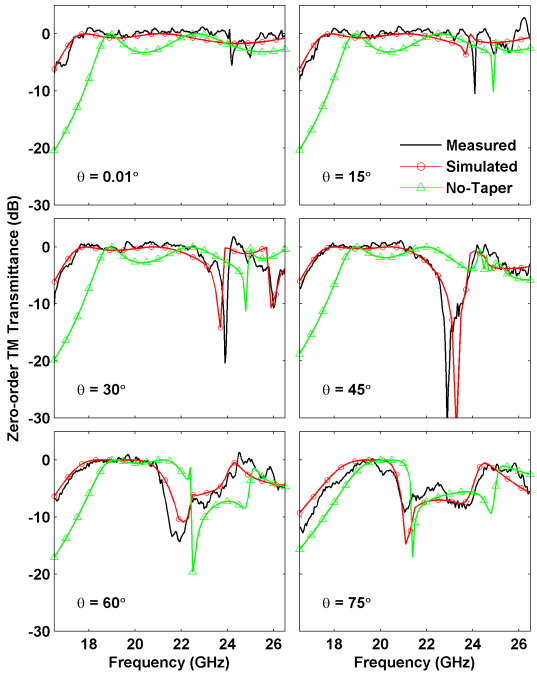

(b) Zero-order TM transmittance vs. frequency

Figure 4.8: Zero-order (a) TE and (b) TM transmittance as a function of frequency for the thick FSS shown in Fig. 4.7. The plane of incidence is $\phi = 90°$, where $\theta = \{0.01°, 15°, 30°, 45°, 60°, 75°\}$. Simulations of an FSS with identical center radius $r_0 = 3.264\,\text{mm}$ and no taper are included for comparison.

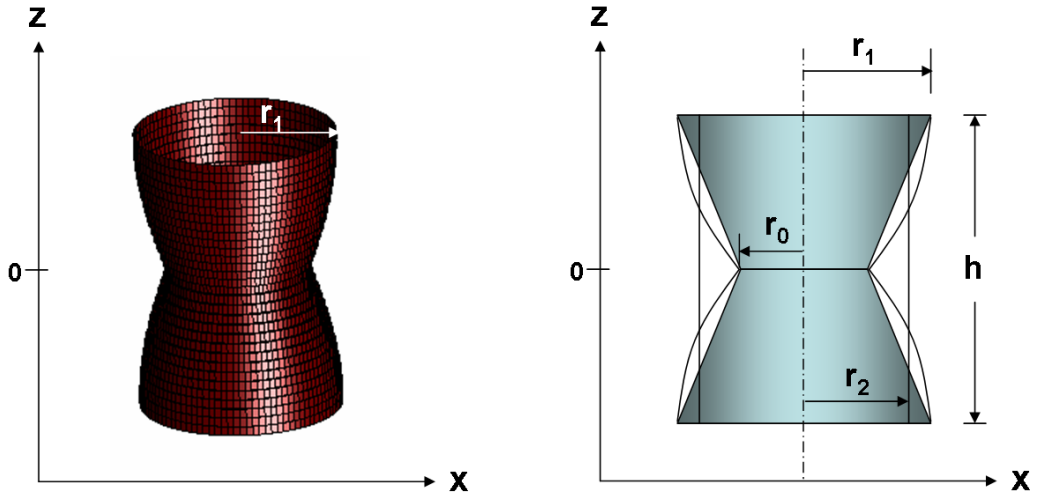

(a) (b)

Figure 4.9: (a) Cosine profile showing 31 layers of straight waveguide sections each 0.298 mm thick with radius given by (4.2) where $r_1 = 3.2639$ mm. (b) Geometry comparisons to that of a linear taper with $r_0 = 0.7\,r_1$ and a straight perforation with $r_2 = 0.9\,r_1$.

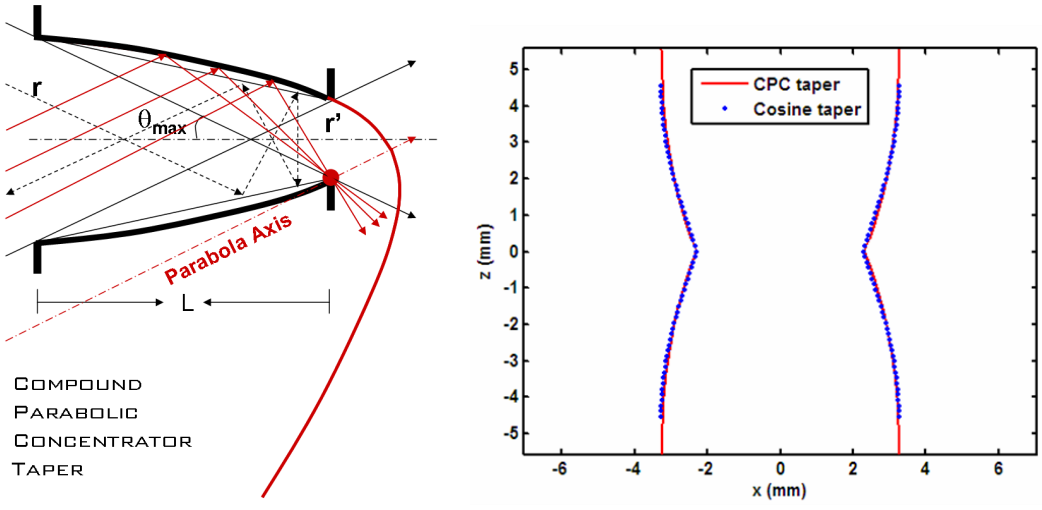

(a) (b)

Figure 4.10: (a) Ray tracing analysis of compound parabolic concentrator as compared to a linear taper. (b) Profile comparison between the cosine taper (4.2) and the compound parabolic taper with $\theta_{\max} = 45^\circ$ and $r' = r_0$.

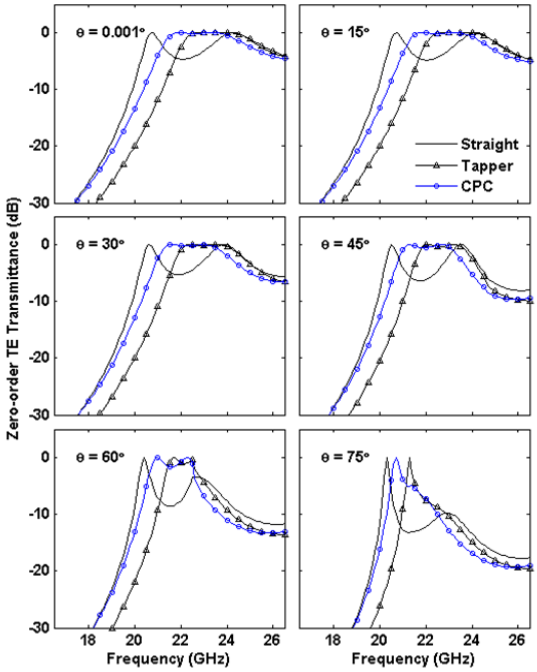

(a) Zero-order TE transmittance vs. frequency

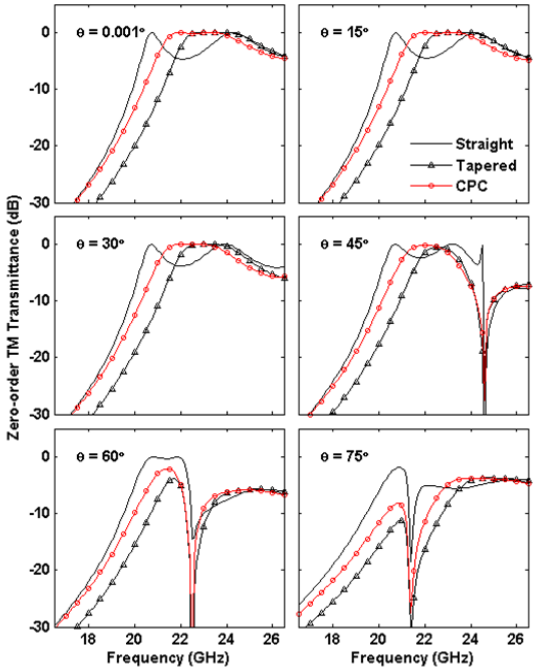

(b) Zero-order TM transmittance vs. frequency

Figure 4.11: Zero-order (a) TE and (b) TM transmittance as a function of frequency for thick FSSs ($h = 9.24\,\text{mm}$) with unit cell perforations shown in Fig. 4.9(b). The perforations are filled with parafin wax ($\epsilon_r = 2.33$). The plane of incidence is $\phi = 90°$, where $\theta = \{0.001°, 15°, 30°, 45°, 60°, 75°\}$. The lattice parameters are $b = d = 8.24\,\text{mm}$ and $\alpha = 60°$.

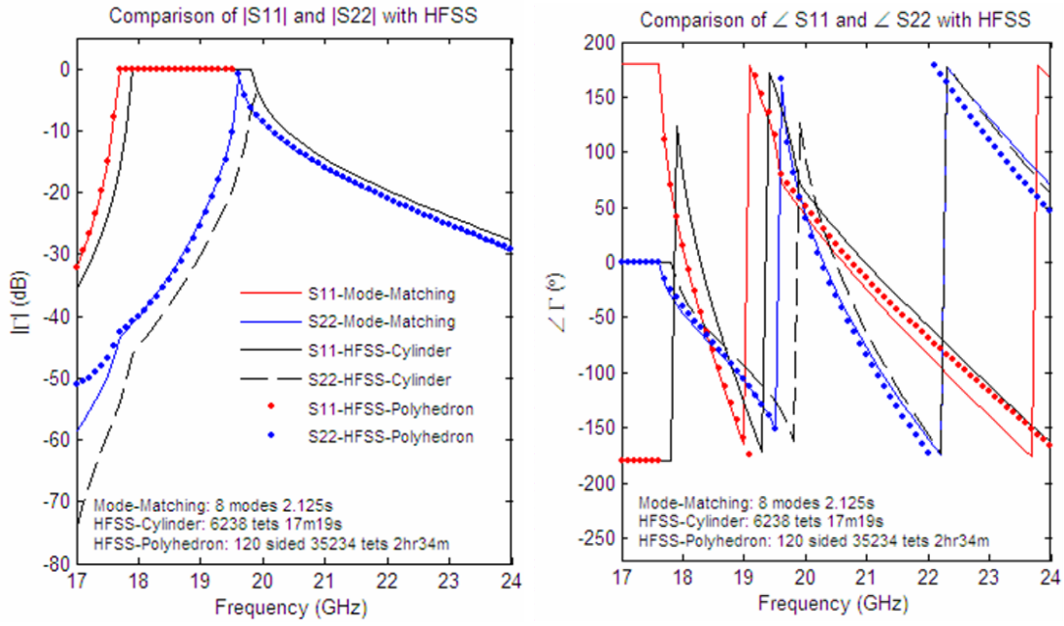

(a) (b)

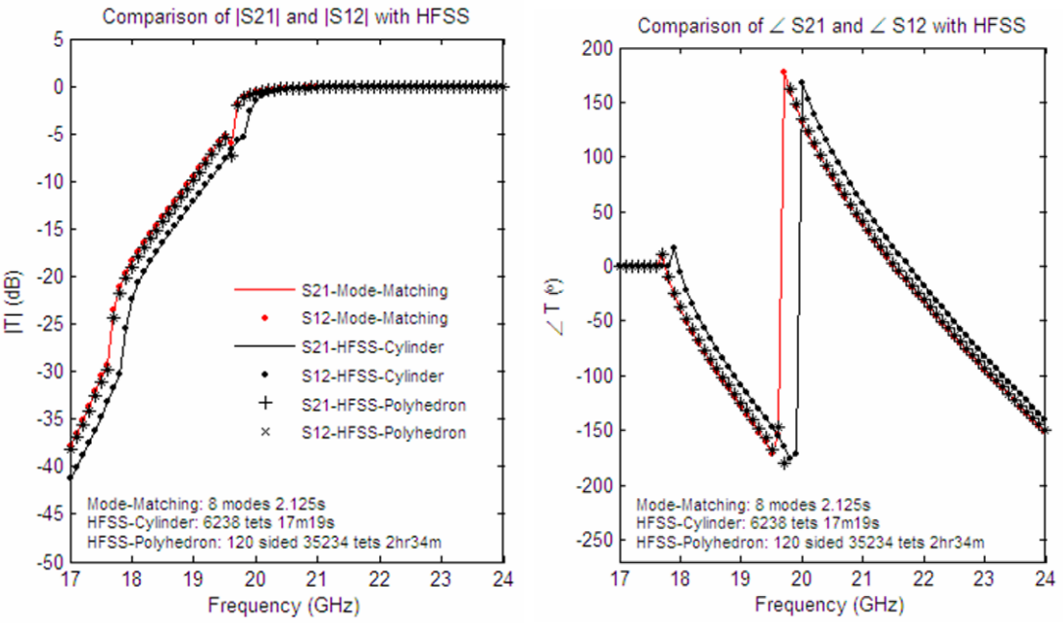

(c) (d)

Figure 4.12: Comparison of (a) $|S_{11}|$ and $|S_{22}|$, (b) $\angle S_{11}$ and $\angle S_{22}$, (c) $|S_{21}|$ and $|S_{12}|$, and (d) $\angle S_{21}$ and $\angle S_{12}$ with Ansoft HFSS analysis of the junction discontinuity between two on-axis cylindrical waveguides where $\rho_b = 0.9\rho a = 2.9376\,\text{mm}$. Solution data are compared with both cylinder and 120-sided polyhedron representations of the cylindrical waveguides in HFSS.

Chapter 5

Conclusion

No matter who you are, what you do or how you live, treat others as your equal; for given the same life circumstances that you are so privileged to have, there is at least the possibility that they could achieve far more good.

— Hung Loui

This thesis demonstrates successful implementation and verification of the MM-EGSM method for analyzing EM scattering from various periodic and aperiodic surfaces. We have retained the advantages of published MM-GSM methods, added new formulations to enable efficient implementation of compound unit cells and unified the theoretical approach for one/two-dimensional periodic and aperiodic surfaces.

5.1 Contributions

5.1.1 Theoretical Contributions

Utilizing the EGSM terminology, the general expressions (3.2)-(3.10) for the resonances of both transmission and reflection surfaces are developed. In addition, we provide a simple EGSM property (3.11) for reducing the computational load

at PEC transitions. Some of the contributions of the Mode Matching-Extended Generalized Scattering Matrix (MM-EGSM) analysis method presented here include:

- The inclusion of the compound unit cell concept into the MM procedure as applied to EM wave scattering from one- and two-dimensional planar, thick-metal, multi-layered, periodic and aperiodic surfaces;

- The extension of GSM network analysis to handle arbitrary internal connections between apertures on both sides of a compound unit cell;

- The utilization of impedance boundary conditions and perturbation theory during the MM procedure to handle external and internal metal losses, respectively.

One of the conclusions of the theoretical formulation presented here is that increasing the aperture-to-period ratio in gratings and FSSs can lead to lowering of the Q of various resonances, thus producing a less polarization-sensitive yet broadband transmission response for wide incidence angles. Recognizing that a large aperture-to-period ratio is equivalent to increasing the level of cross-coupling between adjacent apertures, direct internal connections between adjacent apertures (Fig. 1.2) become a potential design parameter for obtaining desired transmittance and reflectance behavior.

5.1.2 Numerical Contributions

Numerical implementation and algorithm development of the proposed MM-EGSM method were performed using the MATLAB's matrix-friendly scripting language. Although a large amount of coding effort has been devoted to software development, we will only list a few here due to length considerations:

- Transition EGSM redundancy checking to speed up multi-transition simulations.

- EGSM auto assembly, cascade and data extraction.

- 3D modeling with internal/external field computation and visualization.

The largest contribution from this numerical effort is the prediction of new scattering responses of novel compound thick FSS's.

5.2 Future Work

The method presented in this paper can be applied to a number of problems across the EM spectrum. Examples are radomes and dichroic plates for spatial demultiplexing applications [70]. In addition, low-loss components such as filters and polarizers can be designed for millimeter-wave and terahertz imaging and spectroscopy. We are also motivated by applications in the higher microwave through optical regions of the spectrum. For example, the field enhancements shown in Fig. 3.3(a) can be further exploited by filling the perforations with nonlinear materials for spatial modulation of beams in the microwave and optical regimes. Another motivation is the analysis and design of broadband, wide-angle, polarization-insensitive, structurally strong thick-metal surfaces for stealthy radomes covering high-power electronically-steerable antennas. Such a radome can replace the traditional approach which requires lamination of multiple layers of thin-metal patterns sandwiched between dielectrics. Due to thermal expansion when operated under harsh conditions [67], laminations can result in misalignment causing performance degradation [1]. Besides studying various passive structures allowed by the developed theory, rigid and compact tunable surfaces are also subjects of future work. By embedding active devices in the space provided by the thickness of the

FSS plate, scattering characteristics can be altered in a controlled manner. To facilitate optimization and interfacing with electronic circuitry, equivalent circuit models should be developed at junction discontinuities.

Although the current measurement setup is adequate for general transmission comparisons with simulation, it is not accurate for loss and phase characterizations. Future work include the development of a state-of-the-art measurement apparatus (Fig. 5.1) for the purpose of accurate characterization of EM transmission through FSS samples.

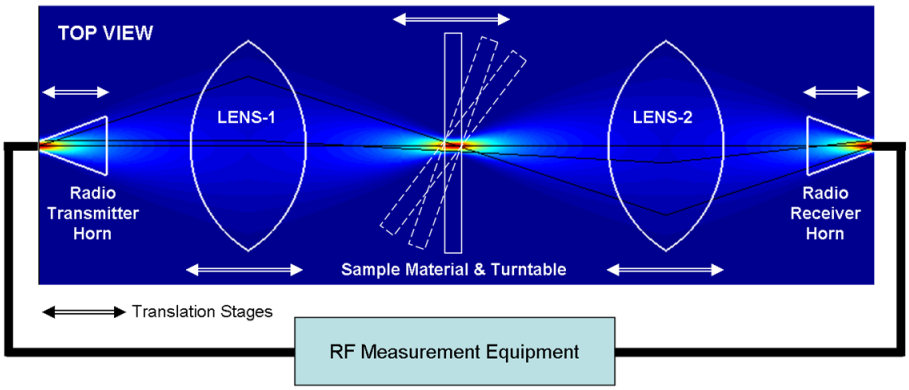

Figure 5.1: A Gaussian beam measurement setup for the characterization of passive and active FSSs.

The proposed measurement setup is similar in design to those deployed in the field of optics. However, due to the relatively large wavelength of operation (millimeter vs. nanometer), lenses, fixtures, tables, and sources in the millimeter-wavelength regime are much larger than in optics. This means accurate positioning devices are not readily available to handle the added weight. To maximize usability and mobility, the proposed apparatus is modular in design and scalable in size. The primary components of the system are sets of large lenses, transmitter/receiver horn antennas and sample holders. The translation stages associated with each component allow for flexible calibration. The proposed measurement system is necessary because EM radiation from an antenna spreads quickly. This

fact complicates EM measurement of materials using only antennas because their radiation will scatter off of anything and everything in its path, including the material sample. Measurement of this type therefore requires a specialized room where expansive absorbers lining the inside walls are used to minimize unwanted reflections so that only scattering from the sample under test is measured. Even with an anechoic chamber, due to finite sample size, it is very difficult to separate signal transmission through the FSS plate from transmission around the FSS plate even with time-gating. A focused Gaussian-beam system does not suffer from the above fact and the scattering process can be analyzed by the theory provided using the principle of superposition.

Bibliography

[1] T. K. Wu, Ed., *Frequency Selective Surface and Grid Array.* New York: John Wiley and Sons, Inc., 1995.

[2] J. C. Vardaxoglou, *Frequency Selective Surfaces: Analysis and Design*, ser. Electronic & Electrical Engineering Research Studies Antenna Series. New York: John Wiley and Sons, Inc., 1997.

[3] B. A. Munk, *Frequency Selective Surfaces Theory and Design.* New York: John Wiley and Sons, Inc., 2000.

[4] R. Petit, *Electromagnetic Theory of Gratings*, ser. Topics in Current Physics. Berlin: Springer-Verlag, 1980, vol. 22.

[5] R. Petit and M. Cadilhac, "Electromagnetic theory of gratings: some advances and some comments on the use of the operator formalism," *J. Opt. Soc. Am. A*, vol. 7, no. 9, pp. 1666–1674, Sept. 1990.

[6] J.-F. Ma and R. Mittra, "Analysis of multiple FSS screens of unequal periodicity using an efficient cascading technique," *IEEE Trans. Microwave Theory Tech.*, vol. 53, no. 4, pp. 1401–1414, Apr. 2005.

[7] J. C. Chen and P. H. Stanton, "Theoretical and experimental results for a thick skew-grid FSS with rectangular apertures at oblique incidence," in *Proc.*

IEEE Antennas and Propagat. Society International Symposium, vol. 3, June 1991, pp. 1866–1869.

[8] C.-C. Chen, "Transmission of microwave through perforated flat plates of finite thickness," *IEEE Trans. Microwave Theory Tech.*, vol. 21, no. 1, pp. 1–6, Jan. 1973.

[9] R. Mittra, C. H. Chan, and T. Cwik, "Techniques for analyzing frequency selective surfaces - a review," *Proceedings of the IEEE*, vol. 76, no. 12, pp. 1593–1615, Dec. 1988.

[10] B. J. Rubin, "Scattering from a periodic array of apertures or plates where the conductors have arbitrary shape, thickness and resistivity," *IEEE Trans. Antennas Propagat.*, vol. 34, no. 11, pp. 1356–1365, Nov. 1986.

[11] S. D. Gedney and R. Mittra, "Analysis of the electromagnetic scattering by thick gratings using a combined FEM/MM solution," *IEEE Trans. Antennas Propagat.*, vol. 39, no. 11, pp. 1605–1614, Nov. 1991.

[12] R. Kastner and R. Mittra, "Iterative analysis of finite-sized planar frequency selective surfaces with rectangular patches or perforations," *IEEE Trans. Antennas Propagat.*, vol. 35, no. 4, pp. 372–377, Apr. 1987.

[13] W. L. Ko and R. Mittra, "Scattering by a truncated periodic array," *IEEE Trans. Antennas Propagat.*, vol. 36, no. 4, pp. 496–503, Apr. 1988.

[14] R. A. Depine and D. C. Skigin, "Scattering from metallic surfaces having a finite number of rectangular grooves," *J. Opt. Soc. Am. A*, vol. 11, no. 11, pp. 2844–2850, Nov. 1994.

[15] D. C. Skigin, V. V. Veremey, and R. Mittra, "Superdirective radiation from finite gratings of rectangular grooves," *IEEE Trans. Antennas Propagat.*, vol. 47, no. 2, pp. 376–383, Feb. 1999.

[16] M. E. MacDonald, A. Alexanian, R. A. York, and Z. Popović, "Spectral transmittance of lossy printed resonant-grid terahertz bandpass filters," *IEEE Trans. Microwave Theory Tech.*, vol. 48, no. 4, pp. 712–718, Apr. 2000.

[17] E. Toro and R. Deleuil, "Application of a rigorous modal theory to electromagnetic diffraction from biperiodic rough surface," *IEEE Trans. Antennas Propagat.*, vol. 33, no. 5, pp. 540–548, May 1985.

[18] L. Li, "Multilayer modal method for diffraction gratings of arbitrary profile, depth and permittivity," *J. Opt. Soc. Am. A*, vol. 10, no. 12, pp. 2581–2591, Dec. 1993.

[19] J. A. Kong, A. Priou, and T. Itoh, Eds., *Electromagnetic Applications of Photonic Band Gap Materials and Structures, Progress In Electromagnetics Research*. Cambridge, Massachusetts: EMW Publishing, 2003, vol. 41.

[20] C. L. Holloway, E. F. Kuester, J. Baker-Jarvis, and P. Kabos, "A double negative DNG composite medium composed of magnetodielectric spherical particles embedded in a matrix," *IEEE Trans. Antennas Propagat.*, vol. 51, no. 10, pp. 2596–2603, Oct. 2003.

[21] T. Itoh, *Numerical Techniques for Microwave and Millimeter-Wave Passive Structures*. New York: John Wiley and Sons, Inc., 1989.

[22] R. C. Booton, *Computational Methods for Electromagnetics and Microwaves*. New York: John Wiley and Sons, Inc., 1992.

[23] I. Anderson, "On the theory of self-resonant grids," *Bell Syst. Tech. J.*, vol. 54, no. 10, pp. 1725–1731, Dec. 1975.

[24] C. K. Lee and R. J. Langley, "Equivalent circuit models for frequency selective surfaces at oblique angles of incidence," *IEE Proc. H*, vol. 132, no. 6, pp. 395–399, Oct. 1985.

[25] C. T. Tai, "A study of the E.M.F. method," *J. Appl. Phys.*, vol. 20, pp. 717–723, July 1949.

[26] Z. B. Popović, R. M. Weikle II, M. Kim, and D. B. Rutledge, "A 100-MESFET planar grid oscillator," *IEEE Trans. Microwave Theory Tech.*, vol. 39, pp. 193–200, Feb. 1991.

[27] S. C. Bundy and Z. B. Popović, "A generalized analysis for grid oscillator design," *IEEE Trans. Microwave Theory Tech.*, vol. 42, no. 12, pp. 2486–2491, Dec. 1994.

[28] A. Wexler, "Solution of waveguide discontinuities by modal analysis," *IEEE Trans. Microwave Theory Tech.*, vol. 15, no. 9, pp. 508–517, Sept. 1967.

[29] N. Amitay, V. Galindo, and C. P. Wu, *Theory and Analysis of Phased Array Antennas.* New York: John Wiley and Sons, Inc., 1972, pp. 37–45.

[30] E. W. Lucas and T. P. Fontana, "A 3-D hybrid finite element/boundary element method for the unified radiation and scattering analysis of general infinite periodic arrays," *IEEE Trans. Antennas Propagat.*, vol. 43, no. 2, pp. 145–153, Feb. 1995.

[31] T. F. Eibert, J. L. Volakis, D. R. Wilton, and D. R. Jackson, "Hybrid FE/BI modeling of 3-D doubly periodic structures utilizing triangular prismatic elements and an MPIE formulation accelerated by the Ewald transformation," *IEEE Trans. Antennas Propagat.*, vol. 47, no. 5, pp. 843–850, May 1999.

[32] D. B. Davidson, A. G. Smith, and J. J. van Tonder, "The analysis, measurement and design of frequency selective surfaces," in *Proc. 10th International Conference on Antennas and Propagat.*, vol. 1, Apr. 1997, pp. 156–160.

[33] P. Harms, R. Mittra, and W. Ko, "Implementation of the periodic boundary condition in the Finite-Difference Time-Domain Algorithm for FSS Struc-

tures," *IEEE Trans. Microwave Theory Tech.*, vol. 42, no. 9, pp. 1317–1324, Sept. 1994.

[34] M. I. Sobhy, M. H. A. El-Azeem, and K. W. Royer, "A new multi-grid 3-D TLM algorithm for simulation of microwave FSS," *IEEE MTT-S International Microwave Symposium Digest*, vol. 2, pp. 439–442, June 1996.

[35] N. Marcuvitz, *Waveguide Handbook*. Massachusetts: Boston Technical Publishers, Inc., 1964.

[36] P. Russer, M. Mongiardo, and L. B. Felson, "Electromagnetic field representations and computations in complex structures I-III," *International Journal of Numerical Modelling: Electronic Networks, Devices and Fields*, vol. 15, pp. 93–145, 2002.

[37] M. Mongiardo, P. Russer, C. Tomassoni, and L. B. Felsen, "Analysis of n-furcation in elliptical waveguides via the generalized network formulation," *IEEE Trans. Microwave Theory Tech.*, vol. 47, no. 12, pp. 2473–2478, Dec. 1999.

[38] S. Monni, "Frequency selective surfaces integrated with phased array antennas - analysis and design using multimode equivalent networks," Ph.D. dissertation, Tech. Univ. of Eindhoven, The Netherlands, June 2005.

[39] L. Li, "Formulation and comparison of two recursive matrix algorithms for modeling layered diffraction gratings," *J. Opt. Soc. Am. A*, vol. 13, no. 5, pp. 1024–1034, May 1996.

[40] F. Dai, "Scattering and transmission matrix representations of multiguide junctions," *IEEE Trans. Microwave Theory Tech.*, vol. 40, no. 7, pp. 1538–1544, July 1992.

[41] B. Widenberg, "A general mode matching technique applied to bandpass

radomes," Lund Institute of Technology Department of Electroscience, Lund, Sweden, Electromagnetic Theory Tech. Rep. TEAT-7098, Aug. 2001.

[42] A. Monorchio, P. Grassi, and G. Manara, "A hybrid mode-matching finite-elements approach to the analysis of thick dichroic screens with arbitrarily shaped apertures," *IEEE Antennas and Wireless Propagat. Letters*, vol. 1, no. 1, pp. 120–123, 2002.

[43] B. Widenberg, S. Poulsen, and A. Karlsson, "Thick screens perforated with a periodic array of apertures with arbitrary cross-section," Lund Institute of Technology Department of Electroscience, Lund, Sweden, Electromagnetic Theory Tech. Rep. TEAT-7082, June 1999.

[44] L. Lewin, D. C. Chang, and E. F. Kuester, *Electromagnetic Waves and Curved Structures*. Stevenage, England: Peter Peregrinus LTD., 1977.

[45] B. Z. Katsenelenbaum, L. M. del Río, M. Pereyaslavets, M. S. Ayza, and M. Thumm, *Theory of Nonuniform Waveguides - the cross-section method*. London, UK: IEE, 1998.

[46] G. G. Gentili, "Properties of TE-TM mode-matching techniques," *IEEE Trans. Antennas Propagat.*, vol. 39, no. 9, pp. 1669–1673, Sept. 1991.

[47] P. Guillot, P. Couffignal, H. Baudrand, and B. Theron, "Improvement in calculation of some surface integrals: Application to junction characterization in cavity filter design," *IEEE Trans. Microwave Theory Tech.*, vol. 41, no. 12, pp. 2156–2160, Dec. 1993.

[48] T. W. Ebbesen, H. J. Lezec, H. F. Ghaemi, T. Thio, and P. A. Wolff, "Extraordinary optical transmission through sub-wavelength hole arrays," *Nature*, vol. 391, no. 6668, pp. 667–669, Feb. 1998.

[49] F. J. Garcia-Vidal and L. Martin-Moreno, "Transmission and focusing of

light in one-dimensional periodically nanostructured metals," *Phys. Rev. B*, vol. 66, no. 15, p. 155412, Oct. 2002.

[50] D. C. Skigin and R. A. Depine, "Transmission resonances of metallic compound gratings with subwavelength slits," *Phys. Rev. Lett.*, vol. 95, no. 21, p. 217402, Nov. 2005.

[51] A. N. Fantino, S. I. Grosz, and D. C. Skigin, "Resonant effects in periodic gratings comprising a finite number of grooves in each period," *Phys. Rev. E*, vol. 64, p. 16605, June 2001.

[52] R. F. Harrington, *Time-Harmonic Electromagnetic Fields*. New York: John Wiley and Sons, Inc., 2001, pp. 317–380.

[53] H. Loui, E. Kuester, F. Lalezari, and Z. Popović, "Thick FSSs for large scan angle applications," in *Proc. IEEE Antennas and Propagat. Society International Symposium*, vol. 2, Monterey, CA, June 2004, pp. 2171–2174.

[54] R. J. Luebbers and B. A. Munk, "Analysis of thick rectangular waveguide windows with finite conductivity," *IEEE Trans. Microwave Theory Tech.*, vol. 21, no. 7, pp. 461–468, July 1973.

[55] M. Bozzi, L. Perregrini, J. Weinzierl, and C. Winnewisser, "Design, fabrication, and measurement of frequency-selective surfaces," *Optical Engineering*, vol. 39, no. 8, pp. 2263–2269, Aug. 2000.

[56] P. H. Siegel and J. A. Lichtenberger, "A technique for fabricating free standing electrically thick metallic mesh and parallel wire grids for use as submillimeter wavelength filters and polarizers," in *IEEE MTT-S International Microwave Symposium Digest*, vol. 3, May 1990, pp. 1311–1314.

[57] R. Mittra, T. Itoh, and T.-S. Li, "Analytical and numerical studies of the relative convergence phenomenon arrising in the solution of an integral equa-

tion by the moment method," *IEEE Trans. Microwave Theory Tech.*, vol. 20, no. 2, pp. 96–104, Feb. 1972.

[58] G. I. Veselov and V. M. Temnov, "The solution of some systems of equations in electrodynamics and the relative convergence phenomenon," *Radio Engineering and Electronic Physics*, vol. 26, no. 10, pp. 13–20, 1981.

[59] A. S. Il'inskii and E. Y. Fomenko, "Investigation of infinite-dimensional systems of linear algebraic equations of the second kind in waveguide diffraction problems," *Computational Mathematics and Mathematical Physics*, vol. 31, no. 3, pp. 1–11, 1991.

[60] A. K. Bhattacharyya, "On the convergence of MoM and mode matching solutions for infinite array and waveguide problems," *IEEE Trans. Antennas Propagat.*, vol. 51, no. 7, pp. 1599–1606, July 2003.

[61] C. Vassallo, Théorie des Guides d'Ondes Électromagnétiques, tome 2. Eyrolles: Paris, 1985, pp. 587–591.

[62] N. Marcuvitz, *Waveguide Handbook*. Massachusetts: Boston Technical Publishers, Inc., 1964, pp. 243–246.

[63] R. W. Scharstein and A. T. Adams, "Galerkin solution for the thin circular iris in a TE_{11}-mode circular waveguide," *IEEE Trans. Microwave Theory Tech.*, vol. 36, no. 1, pp. 106–113, Feb. 1988.

[64] J. A. Reed and D. M. Byrne, "Frequency-selective surfaces with multiple apertures within a periodic cell," *J. Opt. Soc. Am. A*, vol. 15, no. 3, pp. 660–668, Mar. 1998.

[65] C.-C. Chen, "Transmission through a conducting screen perforated periodically with apertures," *IEEE Trans. Microwave Theory Tech.*, vol. 18, no. 9, pp. 627–632, Sept. 1970.

[66] M. Beruete, M. Sorolla, I. Campillo, and J. S. Dolado, "Increase of the transmission in cut-off metallic hole arrays," *IEEE Microwave and Wireless Components Letters*, vol. 15, no. 2, pp. 116–118, Feb. 2005.

[67] J. D. W. Jr., Ed., *Radome Engineering Handbook Design and Principles.* NewYork, NY: Marcel Dekker, Inc., 1970, pp. 41–126.

[68] N. Guerin, C. Hafner, X. Cui, and R. Vahldieck, "Compact directive antennas using frequency selective surfaces," in *Proc. Asia-Pacific Microwave Conference*, vol. 1, Dec. 2005, pp. 4–7.

[69] P. F. Goldsmith, *Quasioptical Systems - Gaussian Beam Quasioptical Propagation and Applications.* New York: IEEE Press, 1998.

[70] R. Dickie, R. Cahill, H. S. Gamble, V. F. Fusco, A. G. Schuchinsky, and N. Grant, "Spatial demultiplexing in the submillimeter wave band using multilayer free-standing frequency selective surfaces," *IEEE Trans. Antennas Propagat.*, vol. 53, no. 6, pp. 1904–1911, June 2005.

[71] J. A. Bossard, D. H. Werner, T. S. Mayer, J. A. Smith, Y. U. Tang, R. P. Drupp, and L. Li, "The design and fabrication of planar multiband metallodielectric frequency selective surfaces for infrared applications," *IEEE Trans. Antennas Propagat.*, vol. 54, no. 4, pp. 1265–1276, Apr. 2006.

[72] O. Malyuskin, V. Fusco, and A. G. Schuchinsky, "Phase conugating wire FSS lens," *IEEE Trans. Antennas Propagat.*, vol. 54, no. 5, pp. 1399–1404, May 2006.

[73] P. L. Overfelt, "Superspheroids: A new family of radome shapes," *IEEE Trans. Antennas Propagat.*, vol. 43, no. 2, pp. 215–220, Feb. 1995.

[74] W. T. Welford and R. Winston, *The Optics of Nonimaging Concentrators Light and Solar Energy.* New York: Academic Press, 1978.

[75] H. Haskal, "Matrix description of waveguide discontinuities in the presence of evanescent modes," *IEEE Trans. Microwave Theory Tech.*, vol. 12, no. 2, pp. 184–188, Mar. 1964.

[76] D. M. Pozar, *Microwave Engineering*, 2nd ed. New York: John Wiley and Sons, Inc., 1998.

[77] E. Kuester, *Waveguides and Transmission Lines Course Notes*, University of Colorado at Boulder, CO, 2002, p. 103.

Appendix A

EGSM

The greatest good you can do for another is not just to share your riches but to reveal to him his own.

— Benjamin Disraeli, 1804 - 1881

A.1 EGSM Operator

The EGSM operator $\star$ used to cascade two EGSMs is defined by the operation

$$\mathbf{S^c} = \mathbf{S^a} \star \mathbf{S^b}, \tag{A.1}$$

where

$$\mathbf{S^c_{11}} = \mathbf{S^a_{11}} + \mathbf{S^a_{12}} \left(\mathbf{I} - \mathbf{S^b_{11}S^a_{22}}\right)^{-1} \mathbf{S^b_{11}S^a_{21}}, \tag{A.2}$$

$$\mathbf{S^c_{12}} = \mathbf{S^a_{12}} \left(\mathbf{I} - \mathbf{S^b_{11}S^a_{22}}\right)^{-1} \mathbf{S^b_{12}}, \tag{A.3}$$

$$\mathbf{S^c_{21}} = \mathbf{S^b_{21}} \left(\mathbf{I} - \mathbf{S^a_{22}S^b_{11}}\right)^{-1} \mathbf{S^a_{21}}, \tag{A.4}$$

$$\mathbf{S^c_{22}} = \mathbf{S^b_{22}} + \mathbf{S^b_{21}} \left(\mathbf{I} - \mathbf{S^a_{22}S^b_{11}}\right)^{-1} \mathbf{S^a_{22}S^b_{12}}. \tag{A.5}$$

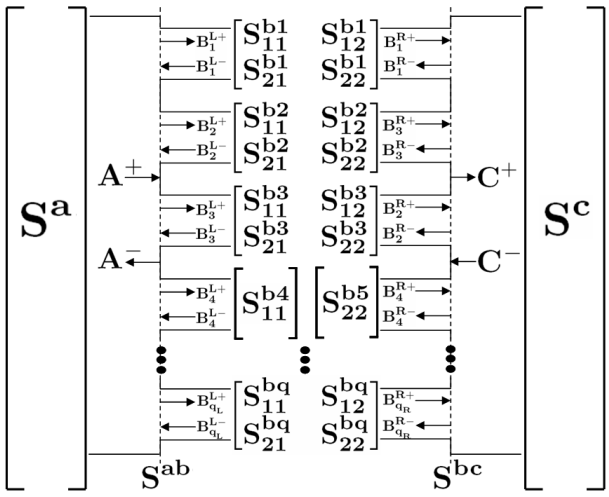

Figure A.1: EGSM equivalent representation of the structure shown in Fig. 2.1.

A.2 EGSM Assembly

Fig. A.1 is an EGSM matrix representation of the structure shown in Fig. 2.1. Each EGSM $\mathbf{S^{bq}}$ is allowed to contain multiple sub-EGSMs which relate field amplitudes at the ends of various junctions between two transitions; this is especially true when the waveguides connecting multiple apertures couple to each other internally. They are always presented in the form of a large 2×2 block EGSM regardless of the number of junctions at each transition; this is to emphasis the transition rather than the junction concept. For example:

$$\mathbf{B_1^{L\pm}} = \begin{bmatrix} \mathbf{B_{11}^{L\pm}} \\ \mathbf{B_{12}^{L\pm}} \\ \vdots \\ \mathbf{B_{1n_L}^{L\pm}} \end{bmatrix}, \quad \mathbf{B_1^{R\pm}} = \begin{bmatrix} \mathbf{B_{11}^{R\pm}} \\ \mathbf{B_{12}^{R\pm}} \\ \vdots \\ \mathbf{B_{1n_R}^{R\pm}} \end{bmatrix}, \tag{A.6}$$

where $\mathbf{n_L}$ and $\mathbf{n_R}$ are the number of apertures at the left and right-ends of $\mathbf{S^{b1}}$, respectively. Similarly,

$$\mathbf{B_4^{R+}} = \begin{bmatrix} \mathbf{B_{41}^{R+}} \\ \mathbf{B_{42}^{R+}} \end{bmatrix}, \quad \mathbf{B_4^{R-}} = \begin{bmatrix} \mathbf{B_{41}^{R-}} \\ \mathbf{B_{42}^{R-}} \end{bmatrix}. \tag{A.7}$$

In general $\mathbf{B}^{\mathbf{bq}\pm}_{\mathbf{qn_{L,R}}}$ is a column vector containing the amplitudes of all modes inside its aperture. Using Fig. A.1 as a guide, we can write down the following set of equations:

$$\begin{bmatrix} \mathbf{B}_{\mathbf{1}}^{\mathbf{L}-} \\ \mathbf{B}_{\mathbf{1}}^{\mathbf{R}+} \end{bmatrix} = \begin{bmatrix} \mathbf{S}_{\mathbf{11}}^{\mathbf{b1}} & \mathbf{S}_{\mathbf{12}}^{\mathbf{b1}} \\ \mathbf{S}_{\mathbf{21}}^{\mathbf{b1}} & \mathbf{S}_{\mathbf{22}}^{\mathbf{b1}} \end{bmatrix} \begin{bmatrix} \mathbf{B}_{\mathbf{1}}^{\mathbf{L}+} \\ \mathbf{B}_{\mathbf{1}}^{\mathbf{R}-} \end{bmatrix}, \tag{A.8}$$

$$\begin{bmatrix} \mathbf{B}_{\mathbf{2}}^{\mathbf{L}-} \\ \mathbf{B}_{\mathbf{3}}^{\mathbf{R}+} \end{bmatrix} = \begin{bmatrix} \mathbf{S}_{\mathbf{11}}^{\mathbf{b2}} & \mathbf{S}_{\mathbf{12}}^{\mathbf{b2}} \\ \mathbf{S}_{\mathbf{21}}^{\mathbf{b2}} & \mathbf{S}_{\mathbf{22}}^{\mathbf{b2}} \end{bmatrix} \begin{bmatrix} \mathbf{B}_{\mathbf{2}}^{\mathbf{L}+} \\ \mathbf{B}_{\mathbf{3}}^{\mathbf{R}-} \end{bmatrix}, \tag{A.9}$$

$$\begin{bmatrix} \mathbf{B}_{\mathbf{3}}^{\mathbf{L}-} \\ \mathbf{B}_{\mathbf{2}}^{\mathbf{R}+} \end{bmatrix} = \begin{bmatrix} \mathbf{S}_{\mathbf{11}}^{\mathbf{b3}} & \mathbf{S}_{\mathbf{12}}^{\mathbf{b3}} \\ \mathbf{S}_{\mathbf{21}}^{\mathbf{b3}} & \mathbf{S}_{\mathbf{22}}^{\mathbf{b3}} \end{bmatrix} \begin{bmatrix} \mathbf{B}_{\mathbf{3}}^{\mathbf{L}+} \\ \mathbf{B}_{\mathbf{2}}^{\mathbf{R}-} \end{bmatrix}, \tag{A.10}$$

$$\begin{bmatrix} \mathbf{B}_{\mathbf{4}}^{\mathbf{L}-} \end{bmatrix} = \begin{bmatrix} \mathbf{S}_{\mathbf{11}}^{\mathbf{b4}} \end{bmatrix} \begin{bmatrix} \mathbf{B}_{\mathbf{4}}^{\mathbf{L}+} \end{bmatrix}, \tag{A.11}$$

$$\begin{bmatrix} \mathbf{B}_{\mathbf{4}}^{\mathbf{R}+} \end{bmatrix} = \begin{bmatrix} \mathbf{S}_{\mathbf{22}}^{\mathbf{b5}} \end{bmatrix} \begin{bmatrix} \mathbf{B}_{\mathbf{4}}^{\mathbf{R}-} \end{bmatrix}, \tag{A.12}$$

$$\begin{bmatrix} \mathbf{B}_{\mathbf{q_L}}^{\mathbf{L}-} \\ \mathbf{B}_{\mathbf{q_L}}^{\mathbf{R}+} \end{bmatrix} = \begin{bmatrix} \mathbf{S}_{\mathbf{11}}^{\mathbf{bq}} & \mathbf{S}_{\mathbf{12}}^{\mathbf{bq}} \\ \mathbf{S}_{\mathbf{21}}^{\mathbf{bq}} & \mathbf{S}_{\mathbf{22}}^{\mathbf{bq}} \end{bmatrix} \begin{bmatrix} \mathbf{B}_{\mathbf{q_R}}^{\mathbf{L}+} \\ \mathbf{B}_{\mathbf{q_R}}^{\mathbf{R}-} \end{bmatrix}. \tag{A.13}$$

Notice, we have deliberately switched the junction field amplitude labels in $\mathbf{S}^{\mathbf{b2}}$ and $\mathbf{S}^{\mathbf{b3}}$ to match the junction crossing shown in Fig. 2.1(b). In order to utilize the EGSM cascade operator $\star$ it is necessary to rearrange or assemble the above set of equations such that field amplitudes away from a section are grouped together and related by an assembled EGSM to field amplitudes toward a section. Let

$$\mathbf{B}^{\mathbf{L}\pm} = \begin{bmatrix} \mathbf{B}_{\mathbf{1}}^{\mathbf{L}\pm} \\ \mathbf{B}_{\mathbf{2}}^{\mathbf{L}\pm} \\ \vdots \\ \mathbf{B}_{\mathbf{q_L}}^{\mathbf{L}+} \end{bmatrix}, \quad \mathbf{B}^{\mathbf{R}\pm} = \begin{bmatrix} \mathbf{B}_{\mathbf{1}}^{\mathbf{R}\pm} \\ \mathbf{B}_{\mathbf{2}}^{\mathbf{R}\pm} \\ \vdots \\ \mathbf{B}_{\mathbf{q_R}}^{\mathbf{R}\pm} \end{bmatrix}, \tag{A.14}$$

then

$$\begin{bmatrix} \mathbf{B}^{\mathbf{L}-} \\ \mathbf{B}^{\mathbf{R}+} \end{bmatrix} = \begin{bmatrix} \mathbf{S}_{\mathbf{11}}^{\mathbf{b}} & \mathbf{S}_{\mathbf{12}}^{\mathbf{b}} \\ \mathbf{S}_{\mathbf{21}}^{\mathbf{b}} & \mathbf{S}_{\mathbf{22}}^{\mathbf{b}} \end{bmatrix} \begin{bmatrix} \mathbf{B}^{\mathbf{L}+} \\ \mathbf{B}^{\mathbf{R}-} \end{bmatrix}. \tag{A.15}$$

For example,

$$\mathbf{S_{12}^{b}} = \begin{bmatrix} \mathbf{S_{12}^{b1}} & 0 & 0 & 0 & 0 & 0 \\ 0 & 0 & \mathbf{S_{12}^{b2}} & 0 & 0 & 0 \\ 0 & \mathbf{S_{12}^{b3}} & 0 & 0 & 0 & 0 \\ 0 & 0 & 0 & \mathbf{S_{12}^{b4}} & 0 & 0 \\ 0 & 0 & 0 & 0 & \ddots & 0 \\ 0 & 0 & 0 & 0 & 0 & \mathbf{S_{12}^{bq}} \end{bmatrix}. \tag{A.16}$$

The sub-EGSM matrices $\mathbf{S_{ij}^{b}}$ for $\mathbf{i,j} \in \{\mathbf{1},\mathbf{2}\}$ are usually sparse when there are no additional couplings among any predefined $\mathbf{S^{bq}}$; under this condition, it is possible to relabel the transitions so that they are purely diagonal. The current labeling scheme is chosen to illustrate the effect of junction crossings on EGSM assembly.

A.3 Operator Property

It can be shown using (A.2)-(A.5) that the $\star$ operator is associative:

$$(\mathbf{S^{a}} \star \mathbf{S^{b}}) \star \mathbf{S^{c}} = \mathbf{S^{a}} \star (\mathbf{S^{b}} \star \mathbf{S^{c}}). \tag{A.17}$$

This means that cascading multiple transitions or sections need not proceed in the same order as dictated by excitation relative to the geometry.

A.4 Singularity Analysis

Analysis of EM scattering from infinitely thin screens using the MM/()/EGSM method often leads to matrix singularities during the EGSM cascade process. This phenomenon also occurs in waveguide discontinuity problems where two guides are connected such that a common cross section of zero thickness intersect both partially. Let

$$\mathbf{S^{c}} = \mathbf{S^{ab}} \star \mathbf{S^{b}} \star \mathbf{S^{bc}} \tag{A.18}$$

represent the cascade of transition **ab**, section **b** and transition **bc** where

$$\mathbf{S^{ab}} = \begin{bmatrix} \mathbf{S_{11}^{ab}} & \mathbf{S_{12}^{ab}} \\ \mathbf{S_{21}^{ab}} & \mathbf{S_{22}^{ab}} \end{bmatrix}, \ \mathbf{S^{b}} = \begin{bmatrix} \mathbf{0} & \mathbf{S_{12}^{b}} \\ \mathbf{S_{21}^{b}} & \mathbf{0} \end{bmatrix}, \ \mathbf{S^{bc}} = \begin{bmatrix} \mathbf{S_{11}^{bc}} & \mathbf{S_{12}^{bc}} \\ \mathbf{S_{21}^{bc}} & \mathbf{S_{22}^{bc}} \end{bmatrix}, \tag{A.19}$$

and $\mathbf{P^{b}} = \mathbf{S_{12}^{b}} = \mathbf{S_{21}^{b}}$ be a reciprocal exponential propagator of **b**, then

$$\mathbf{S_{11}^{c}} = \mathbf{S_{11}^{ab}} + \mathbf{S_{12}^{ab}} \left(\mathbf{I} - \mathbf{P^{b}}\mathbf{S_{11}^{bc}}\mathbf{P^{b}}\mathbf{S_{22}^{ab}}\right)^{-1} \mathbf{P^{b}}\mathbf{S_{11}^{bc}}\mathbf{P^{b}}\mathbf{S_{21}^{ab}}, \tag{A.20}$$

$$\mathbf{S_{12}^{c}} = \mathbf{S_{12}^{ab}} \left(\mathbf{I} - \mathbf{P^{b}}\mathbf{S_{11}^{bc}}\mathbf{P^{b}}\mathbf{S_{22}^{ab}}\right)^{-1} \mathbf{P^{b}}\mathbf{S_{12}^{bc}}, \tag{A.21}$$

$$\mathbf{S_{21}^{c}} = \mathbf{S_{21}^{bc}}\mathbf{P^{b}} \left(\mathbf{I} - \mathbf{S_{22}^{ab}}\mathbf{P^{b}}\mathbf{S_{11}^{bc}}\mathbf{P^{b}}\right)^{-1} \mathbf{S_{21}^{ab}}, \tag{A.22}$$

$$\mathbf{S_{22}^{c}} = \mathbf{S_{22}^{bc}} + \mathbf{S_{21}^{bc}}\mathbf{P^{b}} \left(\mathbf{I} - \mathbf{S_{22}^{ab}}\mathbf{P^{b}}\mathbf{S_{11}^{bc}}\mathbf{P^{b}}\right)^{-1} \mathbf{S_{22}^{ab}}\mathbf{P^{b}}\mathbf{S_{12}^{bc}}. \tag{A.23}$$

In practice when transitions **ab** and **bc** are mirrors of one another, programmers often reuse computed results of $\mathbf{S^{ab}}$ for $\mathbf{S^{bc}}$ assuming the same number of modes in **c** as in **a** or $\mathbf{S_{11}^{bc}} = \mathbf{S_{22}^{ab}}$, $\mathbf{S_{12}^{bc}} = \mathbf{S_{21}^{ab}}$, $\mathbf{S_{21}^{bc}} = \mathbf{S_{12}^{ab}}$ and $\mathbf{S_{22}^{bc}} = \mathbf{S_{11}^{ab}}$. As a result,

$$\mathbf{S_{11}^{c}} = \mathbf{S_{11}^{ab}} + \mathbf{S_{12}^{ab}} \left(\mathbf{I} - \mathbf{P^{b}}\mathbf{S_{22}^{ab}}\mathbf{P^{b}}\mathbf{S_{22}^{ab}}\right)^{-1} \mathbf{P^{b}}\mathbf{S_{22}^{ab}}\mathbf{P^{b}}\mathbf{S_{21}^{ab}}, \tag{A.24}$$

$$\mathbf{S_{12}^{c}} = \mathbf{S_{12}^{ab}} \left(\mathbf{I} - \mathbf{P^{b}}\mathbf{S_{22}^{ab}}\mathbf{P^{b}}\mathbf{S_{22}^{ab}}\right)^{-1} \mathbf{P^{b}}\mathbf{S_{21}^{ab}}, \tag{A.25}$$

$$\mathbf{S_{21}^{c}} = \mathbf{S_{12}^{ab}}\mathbf{P^{b}} \left(\mathbf{I} - \mathbf{S_{22}^{ab}}\mathbf{P^{b}}\mathbf{S_{22}^{ab}}\mathbf{P^{b}}\right)^{-1} \mathbf{S_{21}^{ab}}, \tag{A.26}$$

$$\mathbf{S_{22}^{c}} = \mathbf{S_{11}^{ab}} + \mathbf{S_{12}^{ab}}\mathbf{P^{b}} \left(\mathbf{I} - \mathbf{S_{22}^{ab}}\mathbf{P^{b}}\mathbf{S_{22}^{ab}}\mathbf{P^{b}}\right)^{-1} \mathbf{S_{22}^{ab}}\mathbf{P^{b}}\mathbf{S_{21}^{ab}}. \tag{A.27}$$

Let,

$$\mathbf{A} = \mathbf{I} - \mathbf{P^{b}}\mathbf{S_{22}^{ab}}\mathbf{P^{b}}\mathbf{S_{22}^{ab}} = (\mathbf{I} + \mathbf{P^{b}}\mathbf{S_{22}^{ab}})(\mathbf{I} - \mathbf{P^{b}}\mathbf{S_{22}^{ab}}), \tag{A.28}$$

then if the determinant of **A**, $|\mathbf{A}| = 0$, matrix singularities will occur in the above equations. To show that this is indeed the case, recall

$$\mathbf{S_{22}^{ab}} = \left[\mathbf{Y^{b}} + \mathbf{C^{*}}(\mathbf{Y^{a^{*}}} + \mathbf{Y^{as}})^{-1}\mathbf{C^{t}}\right]^{-1} \left[\mathbf{Y^{b}} - \mathbf{C^{*}}(\mathbf{Y^{a^{*}}} + \mathbf{Y^{as}})^{-1}\mathbf{C^{t}}\right], \tag{A.29}$$

where admittance matrixes $\mathbf{Y^{b}}$, $\mathbf{Y^{a}}$ and $\mathbf{Y^{as}}$ are square diagonal and the mode coupling matrix (usually not square) **C** is computed from field overlapping inte-

grals. Let $\mathbf{Y_F^c} = \mathbf{C}^*(\mathbf{Y^{a^*}} + \mathbf{Y^{as}})^{-1}\mathbf{C^t}$,

$$\mathbf{I} \pm \mathbf{P^b S_{22}^{ab}} = \mathbf{I} \pm \mathbf{P^b}\left[\mathbf{Y^b} + \mathbf{Y_F^c}\right]^{-1}\left[\mathbf{Y^b} - \mathbf{Y_F^c}\right] \tag{A.30}$$

$$= \mathbf{P^b}\left[\mathbf{Y^b} + \mathbf{Y_F^c}\right]^{-1}\left[\mathbf{Y^b}(\mathbf{P^{b^{-1}}} \pm \mathbf{I}) + \mathbf{Y_F^c}(\mathbf{P^{b^{-1}}} \mp \mathbf{I})\right], \tag{A.31}$$

then the determinant of

$$\left|\mathbf{I} \pm \mathbf{P^b S_{22}^{ab}}\right| = \frac{\left|\mathbf{P^b}\right|\left|\mathbf{Y^b}(\mathbf{P^{b^{-1}}} \pm \mathbf{I}) + \mathbf{Y_F^c}(\mathbf{P^{b^{-1}}} \mp \mathbf{I})\right|}{|\mathbf{Y^b} + \mathbf{Y_F^c}|}. \tag{A.32}$$

Taking the limit

$$\lim_{\mathbf{P^b} \to \mathbf{I}} |\mathbf{A}| = \left|\mathbf{I} + \mathbf{P^b S_{22}^{ab}}\right|\left|\mathbf{I} - \mathbf{P^b S_{22}^{ab}}\right| = \frac{|\mathbf{Y_F^c}|\left|\mathbf{Y^b}\right||\mathbf{2I}|^{\mathbf{2}}}{|\mathbf{Y^b} + \mathbf{Y_F^c}|^{\mathbf{2}}}. \tag{A.33}$$

Unless a matrix element on the main diagonal of $\mathbf{Y^b}$ is zero, $\left|\mathbf{Y^b}\right| \neq \mathbf{0}$. Because $|\mathbf{2I}| \neq \mathbf{0}$, if $|\mathbf{Y_F^c}| = \mathbf{0}$ then $|\mathbf{A}| = \mathbf{0}$. Let $\mathbf{a}$ contain m_a modes and $\mathbf{b}$ contain n_b modes then $\mathbf{C}$ is a $n_b \times m_a$ matrix and $\mathbf{Y^a}$ is a $m_a \times m_a$ matrix; in the case where $n_b > m_a$ it can be shown analytically $|\mathbf{Y_F^c}| = \mathbf{0}$ by pending zero-columns to $\mathbf{C}$ and making it square. Therefore, in order to avoid the occurrence of singularities for the infinitely-thin case where the length of $\mathbf{b} \to 0$, it is necessary that $m_a \geq n_b$.

Appendix B

Integrals

B.1 Normalization Integrals

An excellent discussion of normalization related to matrix description of waveguide discontinuities in the presence of evanescent modes are given in [75].

B.1.1 Floquet Modes

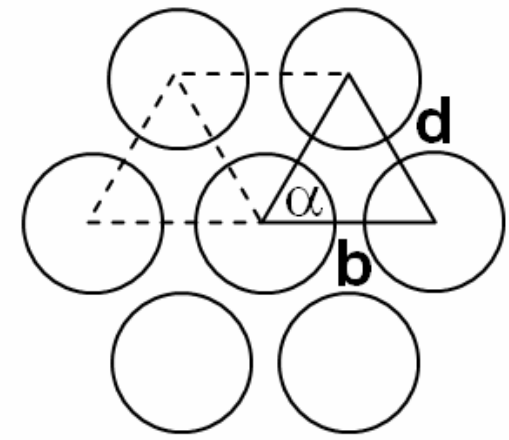

Figure B.1: Lattice geometry.

Longitudinal Floquet Modes

$\hat{z}$ directed Floquet modes [29] in an uniformly filled dielectric unit cell are given by:

$$Hz_{mn} = \left[H_{0_{mn}} e^{j\psi_{mn}}\right] e^{-jk_{x_{mn}}x} e^{-jk_{y_{mn}}y} \tag{B.1}$$

$$Ez_{mn} = \left[E_{0_{mn}} e^{j\xi_{mn}}\right] e^{-jk_{x_{mn}}x} e^{-jk_{y_{mn}}y} \tag{B.2}$$

where $\left[H_{0_{mn}} e^{j\psi_{mn}}\right]$ and $\left[E_{0_{mn}} e^{j\xi_{mn}}\right]$ represent the arbitrary magnitude and phase of the corresponding Hz_{mn} and Ez_{mn} mode. The parameters $k_{x_{mn}}$ and $k_{y_{mn}}$ depend on lattice parameters α, b, d (see Fig. B.1) and incident angles θ, ϕ:

$$k_{x_{mn}} = \sqrt{\epsilon_r} k_0 \sin\theta \cos\phi - \frac{m2\pi}{b} \tag{B.3}$$

$$k_{y_{mn}} = \sqrt{\epsilon_r} k_0 \sin\theta \sin\phi - \left(\frac{n2\pi}{d\sin\alpha} - \frac{m2\pi}{b\tan\alpha}\right) \tag{B.4}$$

$$k_{r_{mn}}^2 = k_{x_{mn}}^2 + k_{y_{mn}}^2 \tag{B.5}$$

where $k_0 = 2\pi/\lambda_0$ and μ_r of the dielectric is assumed to be unity.

Transverse Floquet Modes

The transverse fields relate to the longitudinal fields by way of Maxwell's equations.

TE ($Ez_{mn} = 0$):

$$\vec{E}_{T_{mn}} = \frac{j\omega\mu}{k_{r_{mn}}^2} \hat{z} \times \nabla_T Hz_{mn} = -\frac{\omega\mu}{k_{r_{mn}}^2} \left[k_{y_{mn}}\hat{x} - k_{x_{mn}}\hat{y}\right] Hz_{mn} = \frac{\omega\mu}{\beta_{mn}} \vec{H}_{T_{mn}} \times \hat{z} \tag{B.6}$$

$$\vec{H}_{T_{mn}} = -\frac{j\beta_{mn}}{k_{r_{mn}}^2} \nabla_T Hz_{mn} = -\frac{\beta_{mn}}{k_{r_{mn}}^2} \left[k_{x_{mn}}\hat{x} + k_{y_{mn}}\hat{y}\right] Hz_{mn} = \frac{\beta_{mn}}{\omega\mu} \hat{z} \times \vec{E}_{T_{mn}} \tag{B.7}$$

TM ($Hz_{mn} = 0$):

$$\vec{E}_{T_{mn}} = -\frac{j\beta_{mn}}{k_{r_{mn}}^2}\nabla_T Ez_{mn} = -\frac{\beta_{mn}}{k_{r_{mn}}^2}\left[k_{x_{mn}}\hat{x} + k_{y_{mn}}\hat{y}\right] Ez_{mn} = \frac{\beta_{mn}}{\omega\epsilon}\vec{H}_{T_{mn}} \times z \quad \text{(B.8)}$$

$$\vec{H}_{T_{mn}} = -\frac{j\omega\epsilon}{k_{r_{mn}}^2}\hat{z} \times \nabla_T Ez_{mn} = \frac{\omega\epsilon}{k_{r_{mn}}^2}\left[k_{y_{mn}}\hat{x} - k_{x_{mn}}\hat{y}\right] Ez_{mn} = \frac{\omega\epsilon}{\beta_{mn}}\hat{z} \times \vec{E}_{T_{mn}} \quad \text{(B.9)}$$

where $\beta_{mn} = \sqrt{\epsilon_r k_0^2 - k_{r_{mn}}^2}$ is positive real for $\epsilon_r k_0^2 \geq k_{r_{mn}}^2$ and negative imaginary for $\epsilon_r k_0^2 < k_{r_{mn}}^2$.

Field Normalization Factor $N_{\nu mn}$

For a Floquet mode of type ν, ($\nu = 1 = \text{TE}, \nu = 2 = \text{TM}$) and number mn, let the fields at the longitudinal location z be represented by:

$$\vec{E}_{\nu mn}(x, y, z) = \left(a_{\nu mn}e^{-j\beta_{mn}z} + b_{\nu mn}e^{j\beta_{mn}z}\right)\vec{E}_{T_{\nu mn}}(x, y)N_{\nu mn} \quad \text{(B.10)}$$

$$\vec{H}_{\nu mn}(x, y, z) = \left(a_{\nu mn}e^{-j\beta_{mn}z} - b_{\nu mn}e^{j\beta_{mn}z}\right)\vec{H}_{T_{\nu mn}}(x, y)N_{\nu mn} \quad \text{(B.11)}$$

then the complex power at z by definition is

$$\begin{aligned} P_{\nu mn}(z) &= \iint \hat{z} \cdot \left[\vec{E}_{\nu mn}(x, y, z) \times \vec{H}^*_{\nu mn}(x, y, z)\right] dxdy \\ &= |N_{\nu mn}|^2 \bar{P}_{\nu mn}(z) \iint \vec{E}_{T_{\nu mn}}(x, y) \cdot \left[\vec{H}^*_{T_{\nu mn}}(x, y) \times \hat{z}\right] dxdy \\ &= |N_{\nu mn}|^2 \bar{P}_{\nu mn}(z) P_{T_{\nu mn}} \end{aligned} \quad \text{(B.12)}$$

where

$$P_{T_{\nu mn}} = \frac{\iint \vec{E}_{T_{\nu mn}}(x, y) \cdot \vec{E}^*_{T_{\nu mn}}(x, y)dxdy}{Z^*_{\nu mn}}, \quad \text{(B.13)}$$

$$\bar{P}_{\nu mn}(z) = \begin{cases} |a_{\nu mn}|^2 - |b_{\nu mn}|^2 + 2j\Im(b_{\nu mn}a^*_{\nu mn}e^{j2\beta_{mn}z}), & \beta_{mn} \in \{\Re^+\}; \\ |a_{\nu mn}|^2 - |b_{\nu mn}|^2 - a_{\nu mn}b^*_{\nu mn}e^{-2|\beta_{mn}|z} + b_{\nu mn}a^*_{\nu mn}e^{2|\beta_{mn}|z}, & \beta_{mn} \in \{\Im^-\}; \end{cases} \quad \text{(B.14)}$$

and

$$Z_{\nu mn} = \begin{cases} \frac{\omega\mu}{\beta_{mn}}, & \text{if } \nu = 1; \\ \frac{\beta_{mn}}{\omega\epsilon}, & \text{if } \nu = 2. \end{cases} \quad \text{(B.15)}$$

The time averaged power flow for $\beta_{mn} \in \{\Re^+\}$ is

$$\begin{aligned} P^{av}_{\nu mn}(z) &= \Re[P_{\nu mn}(z)] \\ &= |N_{\nu mn}|^2 \frac{\iint \vec{E}_{T_{\nu mn}}(x,y) \cdot \vec{E}^*_{T_{\nu mn}}(x,y)dxdy}{Z_{\nu mn}} (|a_{\nu mn}|^2 - |b_{\nu mn}|^2) \\ &= |N_{\nu mn}|^2 |P_{T_{\nu mn}}| (|a_{\nu mn}|^2 - |b_{\nu mn}|^2) \end{aligned} \tag{B.16}$$

and for $\beta_{mn} \in \{\Im^-\}$

$$P^{av}_{\nu mn}(z) = \mp |N_{\nu mn}|^2 |P_{T_{\nu mn}}| \Re\left[j(a_{\nu mn} b^*_{\nu mn} e^{-2|\beta_{mn}|z} - b_{\nu mn} a^*_{\nu mn} e^{2|\beta_{mn}|z}) \right] \tag{B.17}$$

where $-$ is for $\nu = 1$ and $+$ for $\nu = 2$.

From the above derivations, if

$$|N_{\nu mn}| = \frac{1}{\sqrt{P_{T_{\nu mn}}}} = \frac{\sqrt{Z^*_{\nu mn}}}{\sqrt{\iint \vec{E}_{T_{\nu mn}}(x,y) \cdot \vec{E}^*_{T_{\nu mn}}(x,y)dxdy}} \tag{B.18}$$

then $P_{\nu mn}(z) = \bar{P}_{\nu mn}(z)$.

Normalized Transverse Floquet Modes

Let the field norm be:

$$\sqrt{\iint \vec{E}_{T_{1mn}}(x,y) \cdot \vec{E}^*_{T_{1mn}}(x,y)dxdy} = \frac{\omega\mu}{k_{r_{mn}}} H_{0_{mn}} \sqrt{S} \tag{B.19}$$

$$\sqrt{\iint \vec{E}_{T_{2mn}}(x,y) \cdot \vec{E}^*_{T_{2mn}}(x,y)dxdy} = \frac{|\beta_{mn}|}{k_{r_{mn}}} E_{0_{mn}} \sqrt{S} \tag{B.20}$$

then the normalized Transverse Floquet modes are:

$$\begin{aligned} \hat{E}_{T_{1mn}} &= \frac{\vec{E}_{T_{1mn}}}{\sqrt{\iint \vec{E}_{T_{1mn}}(x,y) \cdot \vec{E}^*_{T_{1mn}}(x,y)dxdy}} \\ &= \frac{-\frac{\omega\mu}{k^2_{r_{mn}}} \left[k_{y_{mn}} \hat{x} - k_{x_{mn}} \hat{y} \right] H z_{mn}}{\frac{\omega\mu}{k_{r_{mn}}} H_{0_{mn}} \sqrt{S}} \\ &= e^{j\psi_{mn}} \frac{1}{\sqrt{S}} \left(\frac{-k_{y_{mn}} \hat{x} + k_{x_{mn}} \hat{y}}{k_{r_{mn}}} \right) e^{-jk_{x_{mn}} x} e^{-jk_{y_{mn}} y} \end{aligned} \tag{B.21}$$

$$\begin{aligned}
\hat{H}_{T_{1mn}} &= \frac{\vec{H}_{T_{1mn}}}{\sqrt{\iint \vec{E}_{T_{1mn}}(x,y)\cdot\vec{E}^{*}_{T_{1mn}}(x,y)dxdy}} \\
&= \frac{-\frac{\beta_{mn}}{k^2_{r_{mn}}}\left[k_{x_{mn}}\hat{x}+k_{y_{mn}}\hat{y}\right]Hz_{mn}}{\frac{\omega\mu}{k_{r_{mn}}}H_{0_{mn}}\sqrt{S}} \\
&= e^{j\psi_{mn}}\frac{\beta_{mn}}{\omega\mu}\frac{1}{\sqrt{S}}\left(\frac{-k_{x_{mn}}\hat{x}-k_{y_{mn}}\hat{y}}{k_{r_{mn}}}\right)e^{-jk_{x_{mn}}x}e^{-jk_{y_{mn}}y}
\end{aligned} \tag{B.22}$$

$$\begin{aligned}
\hat{E}_{T_{2mn}} &= \frac{\vec{E}_{T_{2mn}}}{\sqrt{\iint \vec{E}_{T_{2mn}}(x,y)\cdot\vec{E}^{*}_{T_{2mn}}(x,y)dxdy}} \\
&= \frac{-\frac{\beta_{mn}}{k^2_{r_{mn}}}\left[k_{x_{mn}}\hat{x}+k_{y_{mn}}\hat{y}\right]Ez_{mn}}{\frac{|\beta_{mn}|}{k_{r_{mn}}}E_{0_{mn}}\sqrt{S}} \\
&= e^{j\xi_{mn}}\frac{\beta_{mn}}{|\beta_{mn}|}\frac{1}{\sqrt{S}}\left(\frac{-k_{x_{mn}}\hat{x}-k_{y_{mn}}\hat{y}}{k_{r_{mn}}}\right)e^{-jk_{x_{mn}}x}e^{-jk_{y_{mn}}y}
\end{aligned} \tag{B.23}$$

$$\begin{aligned}
\hat{H}_{T_{2mn}} &= \frac{\vec{H}_{T_{2mn}}}{\sqrt{\iint \vec{E}_{T_{2mn}}(x,y)\cdot\vec{E}^{*}_{T_{2mn}}(x,y)dxdy}} \\
&= \frac{\frac{\omega\epsilon}{k^2_{r_{mn}}}\left[k_{y_{mn}}\hat{x}-k_{x_{mn}}\hat{y}\right]Ez_{mn}}{\frac{|\beta_{mn}|}{k_{r_{mn}}}E_{0_{mn}}\sqrt{S}} \\
&= e^{j\xi_{mn}}\frac{\omega\epsilon}{|\beta_{mn}|}\frac{1}{\sqrt{S}}\left(\frac{k_{y_{mn}}\hat{x}-k_{x_{mn}}\hat{y}}{k_{r_{mn}}}\right)e^{-jk_{x_{mn}}x}e^{-jk_{y_{mn}}y}
\end{aligned} \tag{B.24}$$

If we choose the arbitrary phases of the longitudinal Floquet modes in the following way:

$$\psi_{mn} = 0 \text{ for } \beta_{mn} \text{ positive real or negative imaginary} \tag{B.25}$$

$$\xi_{mn} = 0 \text{ if } \beta_{mn} \text{ is positive real} \tag{B.26}$$

$$\xi_{mn} = \frac{\pi}{2} \text{ if } \beta_{mn} \text{ is negative imaginary} \tag{B.27}$$

then the normalized transverse Floquet modes become:

$$\hat{E}_{T_{1mn}} = \frac{1}{\sqrt{S}}\left(\frac{-k_{y_{mn}}\hat{x}+k_{x_{mn}}\hat{y}}{k_{r_{mn}}}\right)e^{-jk_{x_{mn}}x}e^{-jk_{y_{mn}}y} = \frac{\omega\mu}{\beta_{mn}}\hat{H}_{T_{1mn}}\times\hat{z} \tag{B.28}$$

$$\hat{H}_{T_{1mn}} = \frac{\beta_{mn}}{\omega\mu}\frac{1}{\sqrt{S}}\left(\frac{-k_{x_{mn}}\hat{x}-k_{y_{mn}}\hat{y}}{k_{r_{mn}}}\right)e^{-jk_{x_{mn}}x}e^{-jk_{y_{mn}}y} = \frac{\beta_{mn}}{\omega\mu}\hat{z}\times\hat{E}_{T_{1mn}} \tag{B.29}$$

$$\hat{E}_{T_{2mn}} = \frac{1}{\sqrt{S}}\left(\frac{-k_{x_{mn}}\hat{x}-k_{y_{mn}}\hat{y}}{k_{r_{mn}}}\right)e^{-jk_{x_{mn}}x}e^{-jk_{y_{mn}}y} = \frac{\beta_{mn}}{\omega\epsilon}\hat{H}_{T_{2mn}}\times z \tag{B.30}$$

$$\hat{H}_{T_{2mn}} = \frac{\omega\epsilon}{\beta_{mn}}\frac{1}{\sqrt{S}}\left(\frac{k_{y_{mn}}\hat{x}-k_{x_{mn}}\hat{y}}{k_{r_{mn}}}\right)e^{-jk_{x_{mn}}x}e^{-jk_{y_{mn}}y} = \frac{\omega\epsilon}{\beta_{mn}}\hat{z}\times\hat{E}_{T_{2mn}} \tag{B.31}$$

B.1.2 Waveguide Modes

The procedure for normalizing waveguide modes are similar to the above. Normalization integrals for cylindrical, rectangular and parallel-plate waveguides are embedded in perturbation calculations of Appendix B.3. For the purpose of establishing notation, the un-normalized longitudinal modes of a cylindrical waveguide [76] are:

For TE($E_z = 0$), $H_z = \psi_1$ modes:

$$\psi_{1nm1} = A_{1nm1} \sin n\phi J_n(k_{c_{1nm1}}\rho), \tag{B.32}$$

$$\psi_{1nm2} = A_{1nm2} \cos n\phi J_n(k_{c_{1nm2}}\rho). \tag{B.33}$$

For TM ($H_z = 0$), $E_z = \psi_2$ modes:

$$\psi_{2nm1} = A_{2nm1} \sin n\phi J_n(k_{c_{2nm1}}\rho), \tag{B.34}$$

$$\psi_{2nm2} = A_{2nm2} \cos n\phi J_n(k_{c_{2nm2}}\rho). \tag{B.35}$$

The first subscript, usually ν, denotes the mode type, 1 = TE and 2 = TM; additional subscripts n and m represent Bessel order and its zero indexes respectively; the last subscript separates the degenerate orthogonal modes.

B.2 Reaction Integrals

Let $\psi_{\nu n}$ represent a longitudinal mode satisfying the wave equation

$$\left(\nabla_T^2 + k_{c_{\nu n}}^2\right) \psi_{\nu n} = 0 \tag{B.36}$$

for a homogeneously-filled waveguide of arbitrary cross section C under boundary conditions:

$$\begin{cases} \frac{\partial H_{z_n}}{\partial \rho} = \left.\frac{\partial \psi_{1n}}{\partial \rho}\right|_C = 0 & \text{Neumann,} \\ E_{z_n} = \psi_{2n}|_C = 0 & \text{Dirichlet.} \end{cases}$$

It is possible to manipulate Maxwell's equations so that the transverse fields are expressed in terms of the longitudinal field components in a lossless medium [77]:

$$\vec{E}_T = -\frac{1}{k^2-\beta^2}[-jw\mu\hat{z}\times\nabla_T H_z + j\beta\nabla_T E_z], \tag{B.37}$$

$$\vec{H}_T = -\frac{1}{k^2-\beta^2}[jw\epsilon\hat{z}\times\nabla_T E_z + j\beta\nabla_T H_z], \tag{B.38}$$

the term $\sqrt{k^2-\beta^2} = k_c$ is usually referred to as the cut-off wave number and β is the propagation constant. Let $\psi_1 = H_z$ and $\psi_2 = E_z$ with subscripts 1 and 2 identifying TE and TM modes respectively, (B.37)-(B.38) separate into the following:

For TE modes, $E_z = 0$, $H_z = \psi_1$,

$$\vec{E}_{T_1} = \frac{jw\mu}{k_{c_1}^2}\hat{z}\times\nabla_T\psi_1, \tag{B.39}$$

$$\vec{H}_{T_1} = \frac{-j\beta_1}{k_{c_1}^2}\nabla_T\psi_1. \tag{B.40}$$

For TM modes, $H_z = 0$, $E_z = \psi_2$,

$$\vec{E}_{T_2} = \frac{-j\beta_2}{k_{c_2}^2}\nabla_T\psi_2, \tag{B.41}$$

$$\vec{H}_{T_2} = \frac{-jw\epsilon}{k_{c_2}^2}\hat{z}\times\nabla_T\psi_2. \tag{B.42}$$

The transverse fields relate to each other via the following:

$$\vec{H}_{T_1} = Y_1\hat{z}\times\vec{E}_{T_1}, \tag{B.43}$$

$$\vec{H}_{T_2} = Y_2\hat{z}\times\vec{E}_{T_2}, \tag{B.44}$$

where,

$$Y_1 = \frac{\beta_1}{\omega\mu}, \tag{B.45}$$

$$Y_2 = \frac{w\epsilon}{\beta_2}. \tag{B.46}$$

Suppose that two sets of fields $\vec{E}^b_{T_{vn}}$ and $\vec{H}^a_{T_{v'n'}}$ are valid over Ω^b and Ω^a, respectively

where $\Omega^b \subseteq \Omega^a$ and we wish to evaluate

$$\begin{aligned} S_{vn,v'n'} &= \int_{\Omega^b} \left(\vec{E}^b_{T_{vn}} \times \vec{H}^{a*}_{T_{v'n'}} \right) \cdot \hat{z}\, ds = \int_{\Omega^b} \vec{E}^b_{T_{vn}} \cdot \underbrace{\left(\vec{H}^{a*}_{v'n'} \times \hat{z} \right)}_{Y^{a*}_{v'n'} \vec{E}^{a*}_{T_{v'n'}}} ds \\ &= Y^{a*}_{v'n'} \int_{\Omega^b} \vec{E}^b_{T_{vn}} \cdot \vec{E}^{a*}_{T_{v'n'}}\, ds. \end{aligned} \tag{B.47}$$

Define the inner product between two transverse vectors $\vec{A}_T$ and $\vec{B}_T$ as

$$\langle \vec{A}_T | \vec{B}_T \rangle_\Omega = \int_\Omega \vec{A}_T \cdot \vec{B}^*_T\, ds, \tag{B.48}$$

where $*$ denotes complex conjugate.

TE-TE

$$\begin{aligned} \langle \vec{E}^b_{T_{1n}} | \vec{E}^a_{T_{1n'}} \rangle_{\Omega^b} &= \left(\frac{jw\mu^b}{k^2_{c_{1n}}} \right) \left(\frac{jw\mu^a}{k^2_{c_{1n'}}} \right)^* \int_{\Omega^b} \hat{z} \times \nabla_T \psi^b_{1n} \cdot \hat{z} \times \nabla_T \psi^{a*}_{1n'}\, ds \\ &= \left(\frac{w\mu^b}{k^2_{c_{1n}}} \right) \left(\frac{w\mu^a}{k^2_{c_{1n'}}} \right) \int_{\Omega^b} \nabla_T \psi^b_{1n} \cdot \nabla_T \psi^{a*}_{1n'}\, ds \end{aligned} \tag{B.49}$$

Using the directional derivative of a scalar (C.1), two-dimensional divergence theorem (C.6), Helmholtz wave equation and the Neumann boundary condition:

$$\begin{aligned} \langle \nabla_T \psi^b_{1n} | \nabla_T \psi^a_{1n'} \rangle_{\Omega^b} &= \int_{\Omega^b} \nabla_T \cdot (\psi^{a*}_{1n'} \nabla_T \psi^b_{1n})\, ds - \int_{\Omega^b} \psi^{a*}_{1n'} \underbrace{\nabla^2_T \psi^b_{1n}}_{-k^2_{c_{1n}} \psi^b_{1n}} ds \\ &= \oint_{d\Omega^b} \psi^{a*}_{1n'} \underbrace{\nabla_T \psi^b_{1n} \cdot \hat{n}}_{=0,\, \text{on } d\Omega^b}\, dl + k^{b2}_{c_{1n}} \int_{\Omega^b} \psi^{a*}_{1n'} \psi^b_{1n}\, ds \\ &= k^{b2}_{c_{1n}} \int_{\Omega^b} \psi^b_{1n} \psi^{a*}_{1n'}\, ds \end{aligned} \tag{B.50}$$

$$\boxed{\langle \vec{E}^b_{T_{1n}} | \vec{E}^a_{T_{1n'}} \rangle_{\Omega^b} = \frac{\omega^2 \mu^b \mu^a}{k^2_{c_{1n'}}} \int_{\Omega^b} \psi^b_{1n} \psi^{a*}_{1n'}\, ds} \tag{B.51}$$

TE-TM

$$\langle \vec{E}^b_{T_{1n}} | \vec{E}^a_{T_{2n'}} \rangle_{\Omega^b} = \left(\frac{jw\mu^b}{k^2_{c_{1n}}} \right) \left(\frac{-j\beta^a_{2n'}}{k^2_{c_{2n'}}} \right)^* \int_{\Omega^b} \hat{z} \times \nabla_T \psi^b_{1n} \cdot \nabla_T \psi^{a*}_{2n'}\, ds \tag{B.52}$$

Using vector identities (C.3), (C.4) and two-dimensional divergence theorem (C.6):

$$\begin{aligned}\langle \hat{z} \times \nabla_T \psi^b_{1n} | \nabla_T \psi^a_{2n'} \rangle_{\Omega^b} &= \int_{\Omega^b} \left[\nabla_T \cdot [\psi^{a*}_{2n'} (\hat{z} \times \nabla_T \psi^b_{1n})] - \psi^{a*}_{2n'} \underbrace{\nabla_T \cdot (\hat{z} \times \nabla_T \psi^b_{1n})}_{=0} \right] ds \\ &= \oint_{d\Omega^b} \psi^{a*}_{2n'} (\hat{z} \times \nabla_T \psi^b_{1n}) \cdot \hat{n}\, dl \\ &= - \oint_{d\Omega^b} \psi^{a*}_{2n'} \nabla_T \psi^b_{1n} \cdot \underbrace{(\hat{z} \times \hat{n})\, dl}_{\vec{dl}}\end{aligned}$$

Alternatively, if we had started with

$$\langle \vec{E}^b_{T_{1n}} | \vec{E}^a_{T_{2n'}} \rangle_{\Omega^b} = \left(\frac{jw\mu^b}{k^2_{c_{1n}}} \right) \left(\frac{-j\beta^a_{2n'}}{k^2_{c_{2n'}}} \right)^* \int_{\Omega^b} -\hat{z} \times \nabla_T \psi^{a*}_{2n'} \cdot \nabla_T \psi^b_{2n}\, ds \tag{B.53}$$

then

$$\langle \nabla_T \psi^b_{2n} | \nabla_T \psi^{a*}_{2n'} \times \hat{z} \rangle_{\Omega^b} = \langle \hat{z} \times \nabla_T \psi^b_{1n} | \nabla_T \psi^a_{2n'} \rangle_{\Omega^b} = \oint_{d\Omega^b} \psi^b_{1n} \nabla_T \psi^{a*}_{2n} \cdot \vec{dl} \tag{B.54}$$

Another way of obtaining the same results is to use (C.3) and write

$$\langle \vec{E}^b_{T_{1n}} | \vec{E}^a_{T_{2n'}} \rangle_{\Omega^b} = \left(\frac{jw\mu^b}{k^2_{c_{1n}}} \right) \left(\frac{-j\beta_{2n'}}{k^2_{c_{2n'}}} \right)^* \int_{\Omega^b} \nabla_T \psi^b_{1n} \times \nabla_T \psi^{a*}_{2n'} \cdot \hat{z}\, ds \tag{B.55}$$

then apply identity (C.5) followed by the two-dimensional Stokes theorem (C.7).

$$\boxed{\langle \vec{E}^b_{T_{1n}} | \vec{E}^a_{T_{2n'}} \rangle_{\Omega^b} = - \left(\frac{w\mu^b}{k^2_{c_{1n}}} \right) \left(\frac{\beta^{a*}_{2n'}}{k^{a^2}_{c_{2n'}}} \right) \oint_{d\Omega^b} \psi^b_{1n} \nabla_T \psi^{a*}_{2n} \cdot \vec{dl}} \tag{B.56}$$

TM-TE

$$\langle \vec{E}^b_{T_{2n}} | \vec{E}^a_{T_{1n'}} \rangle_{\Omega^b} = \left(\frac{-j\beta^b_{2n}}{k^2_{c_{2n}}} \right) \left(\frac{j\omega\mu^a}{k^{a^2}_{c_{1n'}}} \right)^* \int_{\Omega^b} \nabla_T \psi^b_{2n} \cdot \hat{z} \times \nabla_T \psi^{a*}_{1n'}\, ds \tag{B.57}$$

Following similar procedure as for the TE-TM case,

$$\boxed{\langle \vec{E}^b_{T_{2n}} | \vec{E}^a_{T_{1n'}} \rangle_{\Omega^b} = \left(\frac{\beta^b_{2n}}{k^2_{c_{2n}}} \right) \left(\frac{\omega\mu^a}{k^{a^2}_{c_{1n'}}} \right) \oint_{d\Omega^b} \psi^b_{2n} \nabla_T \psi^{a*}_{1n'} \cdot \vec{dl} = 0} \tag{B.58}$$

TM-TM

$$\langle \vec{E}^b_{T_{2n}} | \vec{E}^a_{T_{2n'}} \rangle_{\Omega^b} = \left(\frac{-j\beta^b_{2n}}{k^{b2}_{c_{2n}}} \right) \left(\frac{-j\beta^a_{2n'}}{k^{a2}_{c_{2n'}}} \right)^* \int_{\Omega^b} \nabla_T \psi^b_{2n} \cdot \nabla_T \psi^{a*}_{2n'} \, ds \tag{B.59}$$

Using the directional derivative of a scalar (C.1), two-dimensional divergence theorem (C.6), Helmholtz wave equation and the Dirichlet boundary condition:

$$\begin{aligned} \langle \nabla_T \psi^b_{2n} | \nabla_T \psi^a_{2n'} \rangle_{\Omega^b} &= \int_{\Omega^b} \nabla_T \cdot (\psi^b_{2n} \nabla_T \psi^{a*}_{2n'}) \, ds - \int_{\Omega^b} \psi^b_{2n} \underbrace{\nabla^2_T \psi^{a*}_{2n'}}_{-k^{a2}_{c_{2n'}} \psi^{a*}_{2n'}} \, ds \\ &= \oint_{d\Omega^b} \underbrace{\psi^b_{2n}}_{=0, \text{ on } d\Omega^b} \nabla_T \psi^{a*}_{2n'} \cdot \hat{n} \, dl + k^{a2}_{c_{2n'}} \int_{\Omega^b} \psi^b_{2n} \psi^{a*}_{2n'} \, ds \\ &= k^{a2}_{c_{2n'}} \int_{\Omega^b} \psi^b_{2n} \psi^{a*}_{2n'} \, ds \end{aligned} \tag{B.60}$$

$$\boxed{\langle \vec{E}^b_{T_{2n}} | \vec{E}^a_{T_{2n'}} \rangle_{\Omega^b} = \frac{\beta^b_{2n} \beta^{a*}_{2n'}}{k^{b2}_{c_{1n}}} \int_{\Omega^b} \psi^b_{2n} \psi^{a*}_{2n'} \, ds} \tag{B.61}$$

Because field normalization procedure can differ by preference and implementation, the more general (un-normalized) reaction integrals are given below for various transitions.

B.2.1 Floquet - Cylindrical Waveguide Transition

Define

$$\theta^a_{m'n'} = \tan^{-1} \left(\frac{k^a_{y_{m'n'}}}{k^a_{x_{m'n'}}} \right). \tag{B.62}$$

Integrals of type $\langle \mathbf{TE}^b | \mathbf{TE}^a \rangle$

$$\langle \vec{E}^b_{T_{1nm1}} | \vec{E}^a_{T_{1m'n'}} \rangle = \frac{j^n 2\pi \rho_b \sin(n\theta^a_{m'n'}) A^b_{1nm1} A^{a*}_{1m'n'} w^2 \mu^b \mu^a J_n(k^b_{c_{1nm}} \rho_b) J'_n(k^a_{r_{m'n'}} \rho_b)}{k^a_{r_{m'n'}} (k^{b2}_{c_{1nm}} - k^{a2}_{r_{m'n'}})}, \tag{B.63}$$

$$\langle \vec{E}^b_{T_{1nm2}} | \vec{E}^a_{T_{1m'n'}} \rangle = \frac{j^n 2\pi \rho_b \cos(n\theta^a_{m'n'}) A^b_{1nm2} A^{a*}_{1m'n'} w^2 \mu^b \mu^a J_n(k^b_{c_{1nm}} \rho_b) J'_n(k^a_{r_{m'n'}} \rho_b)}{k^a_{r_{m'n'}} (k^{b2}_{c_{1nm}} - k^{a2}_{r_{m'n'}})}; \tag{B.64}$$

Integrals of type $\langle \mathbf{TE}^b | \mathbf{TM}^a \rangle$

$$\langle \vec{E}^b_{T_{1nm1}} | \vec{E}^a_{T_{2m'n'}} \rangle = \frac{nj^n 2\pi \cos(n\theta^a_{m'n'}) A^b_{1nm1} A^{a^*}_{2m'n'} w\mu^b \beta^{a^*}_{m'n'} J_n(k^b_{c_{1nm}}\rho_b) J_n(k^a_{r_{m'n'}}\rho_b)}{k^{b2}_{c_{1nm}} k^{a2}_{r_{m'n'}}}, \tag{B.65}$$

$$\langle \vec{E}^b_{T_{1nm2}} | \vec{E}^a_{T_{2m'n'}} \rangle = \frac{-nj^n 2\pi \sin(n\theta^a_{m'n'}) A^b_{1nm2} A^{a^*}_{2m'n'} w\mu^b \beta^{a^*}_{m'n'} J_n(k^b_{c_{1nm}}\rho_b) J_n(k^a_{r_{m'n'}}\rho_b)}{k^{b2}_{c_{1nm}} k^{a2}_{r_{m'n'}}}; \tag{B.66}$$

Integrals of type $\langle \mathbf{TM}^b | \mathbf{TE}^a \rangle$

$$\langle \vec{E}^b_{T_{2nm1}} | \vec{E}^a_{T_{1m'n'}} \rangle = 0, \tag{B.67}$$

$$\langle \vec{E}^b_{T_{2nm2}} | \vec{E}^a_{T_{1m'n'}} \rangle = 0; \tag{B.68}$$

Integrals of type $\langle \mathbf{TM}^b | \mathbf{TM}^a \rangle$

$$\langle \vec{E}^b_{T_{2nm1}} | \vec{E}^a_{T_{2m'n'}} \rangle = \frac{j^n 2\pi \rho_b \sin(n\theta^a_{m'n'}) A^b_{2nm1} A^{a^*}_{2m'n'} \beta^b_{2nm} \beta^{a^*}_{m'n'} J'_n(k^b_{c_{2nm}}\rho_b) J_n(k^a_{r_{m'n'}}\rho_b)}{k^b_{c_{2nm}}(k^{a2}_{r_{m'n'}} - k^{b2}_{c_{2nm}})}, \tag{B.69}$$

$$\langle \vec{E}^b_{T_{2nm2}} | \vec{E}^a_{T_{2m'n'}} \rangle = \frac{j^n 2\pi \rho_b \cos(n\theta^a_{m'n'}) A^b_{2nm2} A^{a^*}_{2m'n'} \beta^b_{2nm} \beta^{a^*}_{m'n'} J'_n(k^b_{c_{2nm}}\rho_b) J_n(k^a_{r_{m'n'}}\rho_b)}{k^b_{c_{2nm}}(k^{a2}_{r_{m'n'}} - k^{b2}_{c_{2nm}})}. \tag{B.70}$$

B.2.2 Cylindrical - Cylindrical Waveguide Transition

Define

$$\Delta^s = \begin{cases} \pi, & n = p \neq 0; \\ 0, & n \neq p, n = 0 \text{ or } p = 0; \\ 0, & n = p = 0. \end{cases} \tag{B.71}$$

$$\Delta^c = \begin{cases} \pi, & n = p \neq 0; \\ 0, & n \neq p, n = 0 \text{ or } p = 0; \\ 2\pi, & n = p = 0. \end{cases} \tag{B.72}$$

Integrals of type $\langle \mathbf{TE}^b | \mathbf{TE}^a \rangle$

$$\langle \vec{E}^b_{T_{1nm1}} | \vec{E}^a_{T_{1pq1}} \rangle = \frac{\Delta^s \rho_b A^b_{1nm1} A^{a^*}_{1pq1} w^2 \mu^b \mu^a J_n(k^b_{c_{1nm}} \rho_b) J'_n(k^a_{c_{1pq}} \rho_b)}{k^a_{c_{1pq}} (k^{b^2}_{c_{1nm}} - k^{a^2}_{c_{1pq}})}, \tag{B.73}$$

$$\langle \vec{E}^b_{T_{1nm1}} | \vec{E}^a_{T_{1pq2}} \rangle = 0, \tag{B.74}$$

$$\langle \vec{E}^b_{T_{1nm2}} | \vec{E}^a_{T_{1pq1}} \rangle = 0, \tag{B.75}$$

$$\langle \vec{E}^b_{T_{1nm2}} | \vec{E}^a_{T_{1pq2}} \rangle = \frac{\Delta^c \rho_b A^b_{1nm2} A^{a^*}_{1pq2} w^2 \mu^b \mu^a J_n(k^b_{c_{1nm}} \rho_b) J'_n(k^a_{c_{1pq}} \rho_b)}{k^a_{c_{1pq}} (k^{b^2}_{c_{1nm}} - k^{a^2}_{c_{1pq}})}; \tag{B.76}$$

Integrals of type $\langle \mathbf{TE}^b | \mathbf{TM}^a \rangle$

$$\langle \vec{E}^b_{T_{1nm1}} | \vec{E}^a_{T_{2pq1}} \rangle = 0, \tag{B.77}$$

$$\langle \vec{E}^b_{T_{1nm1}} | \vec{E}^a_{T_{2pq2}} \rangle = \frac{n\Delta^c A^b_{1nm1} A^{a^*}_{2pq2} w \mu^b \beta^{a^*}_{2pq} J_n(k^b_{c_{1nm}} \rho_b) J_p(k^a_{c_{2pq}} \rho_b)}{k^{b^2}_{c_{1nm}} k^{a^2}_{c_{2pq}}}, \tag{B.78}$$

$$\langle \vec{E}^b_{T_{1nm2}} | \vec{E}^a_{T_{2pq1}} \rangle = \frac{-n\Delta^s A^b_{1nm2} A^{a^*}_{2pq1} w \mu^b \beta^{a^*}_{2pq} J_n(k^b_{c_{1nm}} \rho_b) J_p(k^a_{c_{2pq}} \rho_b)}{k^{b^2}_{c_{1nm}} k^{a^2}_{c_{2pq}}}, \tag{B.79}$$

$$\langle \vec{E}^b_{T_{1nm2}} | \vec{E}^a_{T_{2pq2}} \rangle = 0; \tag{B.80}$$

Integrals of type $\langle \mathbf{TM}^b | \mathbf{TE}^a \rangle$

$$\langle \vec{E}^b_{T_{2nm1}} | \vec{E}^a_{T_{1pq1}} \rangle = 0, \tag{B.81}$$

$$\langle \vec{E}^b_{T_{2nm1}} | \vec{E}^a_{T_{1pq2}} \rangle = 0, \tag{B.82}$$

$$\langle \vec{E}^b_{T_{2nm2}} | \vec{E}^a_{T_{1pq1}} \rangle = 0, \tag{B.83}$$

$$\langle \vec{E}^b_{T_{2nm2}} | \vec{E}^a_{T_{1pq2}} \rangle = 0; \tag{B.84}$$

Integrals of type $\langle \mathbf{TM}^b | \mathbf{TM}^a \rangle$

$$\langle \vec{E}^b_{T_{2nm1}} | \vec{E}^a_{T_{2pq1}} \rangle = \frac{\Delta^s \rho_b A^b_{2nm1} A^{a^*}_{2pq1} \beta^b_{2nm} \beta^{a^*}_{2pq} J'_n(k^b_{c_{2nm}} \rho_b) J_n(k^a_{c_{2pq}} \rho_b)}{k^b_{c_{2nm}} (k^{a^2}_{c_{2pq}} - k^{b^2}_{c_{2nm}})}, \tag{B.85}$$

$$\langle \vec{E}^b_{T_{2nm1}} | \vec{E}^a_{T_{2pq2}} \rangle = 0, \tag{B.86}$$

$$\langle \vec{E}^b_{T_{2nm2}} | \vec{E}^a_{T_{2pq1}} \rangle = 0, \tag{B.87}$$

$$\langle \vec{E}^b_{T_{2nm2}} | \vec{E}^a_{T_{2pq2}} \rangle = \frac{\Delta^c \rho_b A^b_{2nm2} A^{a^*}_{2pq2} \beta^b_{2nm} \beta^{a^*}_{2pq} J'_n(k^b_{c_{2nm}} \rho_b) J_n(k^a_{c_{2pq}} \rho_b)}{k^b_{c_{2nm}} (k^{a^2}_{c_{2pq}} - k^{b^2}_{c_{2nm}})}. \tag{B.88}$$

B.2.3 Floquet - Rectangular Waveguide Transition

Define

$$\phi^a_{pq} = k^a_{x_{pq}}\Delta x + k^a_{y_{pq}}\Delta y. \tag{B.89}$$

Integrals of type $\langle \mathbf{TE}^b | \mathbf{TE}^a \rangle$

$$\langle \vec{E}^b_{T_{1mn}} | \vec{E}^a_{T_{1pq}} \rangle = \frac{e^{j\phi^a_{pq}} A^b_{1mn} A^{a^*}_{1pq} w^2 \mu^b \mu^a}{k^{a^2}_{r_{pq}}} \Delta^{cx} \Delta^{cy}, \tag{B.90}$$

$$\Delta^{cx} = \begin{cases} \frac{jk^a_{x_{pq}}[1-e^{jk^a_{x_{pq}} l_b} cos(m\pi)]}{\frac{m^2\pi^2}{l_b^2} - k^{a^2}_{x_{pq}}}, & k^a_{x_{pq}} \neq \frac{m\pi}{l_b}; \\ \frac{l_b}{2}, & k^a_{x_{pq}} = \frac{m\pi}{l_b}; \\ l_b, & k^a_{x_{pq}} = \frac{m\pi}{l_b} = 0. \end{cases} \tag{B.91}$$

$$\Delta^{cy} = \begin{cases} \frac{jk^a_{y_{pq}}[1-e^{jk^a_{y_{pq}} w_b} cos(n\pi)]}{\frac{n^2\pi^2}{w_b^2} - k^{a^2}_{y_{pq}}}, & k^a_{y_{pq}} \neq \frac{n\pi}{w_b}; \\ \frac{w_b}{2}, & k^a_{y_{pq}} = \frac{n\pi}{w_b}; \\ w_b, & k^a_{y_{pq}} = \frac{n\pi}{w_b} = 0. \end{cases} \tag{B.92}$$

Integrals of type $\langle \mathbf{TE}^b | \mathbf{TM}^a \rangle$

$$\langle \vec{E}^b_{T_{1mn}} | \vec{E}^a_{T_{2pq}} \rangle = \frac{e^{j\phi^a_{pq}} A^b_{1mn} A^{a^*}_{2pq} w \mu^b \beta^{a^*}_{pq}}{k^{b^2}_{c_{1mn}} k^{a^2}_{r_{pq}}} \Delta, \tag{B.93}$$

$$\Delta = \frac{m\pi}{l_b}\left[1 - e^{jk^a_{y_{pq}} w_b}\cos(n\pi)\right]\Delta^{sx} - \frac{n\pi}{w_b}\left[1 - e^{jk^a_{x_{pq}} l_b}\cos(m\pi)\right]\Delta^{sy}, \tag{B.94}$$

$$\Delta^{sx} = \begin{cases} \frac{\frac{m\pi}{l_b}[1-e^{jk^a_{x_{pq}} l_b} cos(m\pi)]}{\frac{m^2\pi^2}{l_b^2} - k^{a^2}_{x_{pq}}}, & k^a_{x_{pq}} \neq \frac{m\pi}{l_b}; \\ \frac{jl_b}{2}, & k^a_{x_{pq}} = \frac{m\pi}{l_b}; \\ 0, & k^a_{x_{pq}} = \frac{m\pi}{l_b} = 0. \end{cases} \tag{B.95}$$

$$\Delta^{sy} = \begin{cases} \frac{\frac{n\pi}{w_b}[1-e^{jk^a_{y_{pq}} w_b} cos(n\pi)]}{\frac{n^2\pi^2}{w_b^2} - k^{a^2}_{y_{pq}}}, & k^a_{y_{pq}} \neq \frac{n\pi}{w_b}; \\ \frac{jw_b}{2}, & k^a_{y_{pq}} = \frac{n\pi}{w_b}; \\ 0, & k^a_{y_{pq}} = \frac{n\pi}{w_b} = 0. \end{cases} \tag{B.96}$$

Integrals of type $\langle \mathbf{TM}^b | \mathbf{TE}^a \rangle$

$$\langle \vec{E}^b_{T_{2mn}} | \vec{E}^a_{T_{1pq}} \rangle = 0. \tag{B.97}$$

Integrals of type $\langle \mathbf{TM}^b | \mathbf{TM}^a \rangle$

$$\langle \vec{E}^b_{T_{2mn}} | \vec{E}^a_{T_{2pq}} \rangle = \frac{e^{j\phi^a_{pq}} A^b_{2mn} A^{a^*}_{2pq} \beta^b_{2mn} \beta^{a^*}_{pq}}{k^{b^2}_{c_{2mn}}} \Delta^{sx} \Delta^{sy}. \tag{B.98}$$

B.2.4 Floquet - Parallel-Plate Waveguide Transition

Define

$$\phi^a_{pq} = k^a_{y_{pq}} \Delta y. \tag{B.99}$$

Integrals of type $\langle \mathbf{TE}^b | \mathbf{TE}^a \rangle$

$$\langle \vec{E}^b_{T_{10n}} | \vec{E}^a_{T_{1pq}} \rangle = \frac{e^{j\phi^a_{pq}} A^b_{10n} A^{a^*}_{1pq} w^2 \mu^b \mu^a}{k^{a^2}_{r_{pq}}} \Delta^{cy}. \tag{B.100}$$

Integrals of type $\langle \mathbf{TE}^b | \mathbf{TM}^a \rangle$

$$\langle \vec{E}^b_{T_{10n}} | \vec{E}^a_{T_{2pq}} \rangle = 0. \tag{B.101}$$

Integrals of type $\langle \mathbf{TM}^b | \mathbf{TE}^a \rangle$

$$\langle \vec{E}^b_{T_{20n}} | \vec{E}^a_{T_{1pq}} \rangle = 0. \tag{B.102}$$

Integrals of type $\langle \mathbf{TM}^b | \mathbf{TM}^a \rangle$

$$\langle \vec{E}^b_{T_{20n}} | \vec{E}^a_{T_{2pq}} \rangle = \frac{e^{j\phi^a_{pq}} A^b_{20n} A^{a^*}_{2pq} \beta^b_{20n} \beta^{a^*}_{pq}}{k^{b^2}_{c_{20n}}} \Delta^{sy}. \tag{B.103}$$

The above equations are degenerate forms of the Floquet - Rectangular Waveguide Transition integrals. Equations for the Floquet - Parallel-Plate Waveguide Transition in the vertical configuration should be obvious by comparison.

B.3 Perturbation Integrals

Perturbation integrals are necessary when exact solutions of the modes inside a thick aperture is not available. Small changes in material properties, geometrical variations, and conductor losses are taking into account analytically to help designers quickly perform trend analysis. Although a comprehensive treatment of perturbational and variation techniques is given in [52], detailed derivations of the perturbation expressions for propagating and evanescent modes in lossy waveguides are not given. These derivations are given in this section for various waveguide geometries.

B.3.1 Wall Perturbations

Suppose that a waveguide is filled with lossy material, and consider a perturbation of its perfectly conducting walls. Let the unperturbed fields (subscript 0) and the perturbed fields (no subscript) be

$$\vec{E}_0 = \hat{E}_0^+ e^{-\gamma_0 z}, \qquad \vec{E} = \hat{E}^- e^{+\gamma z}, \tag{B.104}$$

$$\vec{H}_0 = \hat{H}_0^+ e^{-\gamma_0 z}, \qquad \vec{H} = \hat{H}^- e^{+\gamma z}. \tag{B.105}$$

These field equations must satisfy Maxwell's equations

$$\nabla \times \vec{E}_0 = -j\omega\mu\vec{H}_0, \qquad \nabla \times \vec{E} = -j\omega\mu\vec{H}, \tag{B.106}$$

$$\nabla \times \vec{H}_0 = j\omega\epsilon\vec{E}_0, \qquad \nabla \times \vec{H} = j\omega\epsilon\vec{E}; \tag{B.107}$$

or

$$\nabla_T \times \hat{E}_0^+ - \gamma_0 \hat{z} \times \hat{E}_0^+ = -j\omega\mu\hat{H}_0^+, \qquad \nabla_T \times \hat{E}^- + \gamma \hat{z} \times \hat{E}^- = -j\omega\mu\hat{H}^-, \tag{B.108}$$

$$\nabla_T \times \hat{H}_0^+ - \gamma_0 \hat{z} \times \hat{H}_0^+ = j\omega\epsilon\hat{E}_0^+, \qquad \nabla_T \times \hat{H}^- + \gamma \hat{z} \times \hat{H}^- = j\omega\epsilon\hat{E}^-. \tag{B.109}$$

Scalar multiply the last equation by $\hat{E}_0$ and the first equation by $\hat{H}$ and apply the identity

$$\vec{A} \cdot \vec{B} \times \vec{C} = \vec{A} \times \vec{B} \cdot \vec{C} = \vec{C} \times \vec{A} \cdot \vec{B} = -\vec{A} \times \vec{C} \cdot \vec{B}, \tag{B.110}$$

the results are

$$\hat{E}_0^+ \cdot \nabla_T \times \hat{H}^- - \gamma \hat{E}_0^+ \times \hat{H}^- \cdot \hat{z} = j\omega\epsilon \vec{E}^- \cdot \hat{E}_0^+, \tag{B.111}$$

$$\hat{H}^- \cdot \nabla_T \times \hat{E}_0^+ - \gamma_0 \hat{E}_0^+ \times \hat{H}^- \cdot \hat{z} = -j\omega\mu \hat{H}_0^+ \cdot \hat{H}^-. \tag{B.112}$$

Subtract the above two equation and apply the identity

$$\nabla_T \cdot (\vec{A} \times \vec{B}) = \vec{B} \cdot \nabla_T \times \vec{A} - \vec{A} \cdot \nabla_T \times \vec{B}, \tag{B.113}$$

the result is

$$\nabla_T \cdot \left(\hat{E}_0^+ \times \hat{H}^- \right) + (\gamma - \gamma_0) \left(\hat{E}_0^+ \times \hat{H}^- \cdot \hat{z} \right) = - j\omega \left(\mu \hat{H}_0^+ \cdot \hat{H}^- + \epsilon \hat{E}^- \cdot \hat{E}_0^+ \right). \tag{B.114}$$

A similar procedure is carried out using the same set of vector identities for the second and third equation and the result is

$$\nabla_T \cdot \left(\hat{E}^- \times \hat{H}_0^+ \right) + (\gamma - \gamma_0) \left(\hat{E}^- \times \hat{H}_0^+ \cdot \hat{z} \right) = -j\omega \left(\mu \hat{H}^- \cdot \hat{H}_0^+ + \epsilon \hat{E}_0^+ \cdot \hat{E}^- \right). \tag{B.115}$$

Subtract the last two equations

$$\nabla_T \cdot \left(\hat{E}_0^+ \times \hat{H}^- \right) - \nabla_T \cdot \left(\hat{E}^- \times \hat{H}_0^+ \right) = - (\gamma - \gamma_0) \left(\hat{E}_0^+ \times \hat{H}^- - \hat{E}^- \times \hat{H}_0^+ \right) \cdot \hat{z}. \tag{B.116}$$

Geometry Variations

For geometric perturbation of the waveguide PEC walls, the general equation is integrated over the perturbed waveguide cross section S^-,

$$\oint_{C^-} \hat{E}_0^+ \times \hat{H}^- \cdot \vec{dl} = - (\gamma - \gamma_0) \int_{S^-} \left(\hat{E}_0^+ \times \hat{H}^- - \hat{E}^- \times \hat{H}_0^+ \right) \cdot \hat{z}\, ds, \tag{B.117}$$

where the divergence theorem is applied to the left-hand terms, one of which vanishes because $\vec{dl} \times \hat{E}^- = 0$ on C^-. The unknown

$$\gamma = \frac{- \oint_{C^-} \hat{E}_0^+ \times \hat{H}^- \cdot \vec{dl}}{\int_{S^-} \left(\hat{E}_0^+ \times \hat{H}^- - \hat{E}^- \times \hat{H}_0^+ \right) \cdot \hat{z} ds} + \gamma_0. \tag{B.118}$$

Suppose that the unperturbed cross section boundary $C^+ > C^-$ then because $\vec{dl} \times \hat{E}_0^+ = 0$ on C^+,

$$\oint_{C^+} \hat{E}_0^+ \times \hat{H}^- \cdot \vec{dl} = \oint_{C^-} \hat{E}_0^+ \times \hat{H}^- \cdot \vec{dl} + \oint_{\Delta C} \hat{E}_0^+ \times \hat{H}^- \cdot \vec{dl} = 0, \tag{B.119}$$

and

$$\gamma = \frac{\oint_{\Delta C} \hat{E}_0^+ \times \hat{H}^- \cdot \vec{dl}}{\int_{S^-} \left(\hat{E}_0^+ \times \hat{H}^- - \hat{E}^- \times \hat{H}_0^+ \right) \cdot \hat{z} ds} + \gamma_0. \tag{B.120}$$

Finite Conductivity

If there is no geometric change of the waveguide cross section, $S = S^+ = S^-$, $C = C^+ = C^-$ then the general equation integrated over the cross section S is

$$\oint_C \hat{E}^- \times \hat{H}_0^+ \cdot \hat{n}\, dl = (\gamma - \gamma_0) \int_S \left(\hat{E}_0^+ \times \hat{H}^- - \hat{E}^- \times \hat{H}_0^+ \right) \cdot \hat{z}\, ds, \tag{B.121}$$

where the divergence theorem is applied to the left-hand terms, one of which vanishes because $\hat{n} \times \hat{E}_0^+ = 0$ on C. Consider now the perturbation of the walls of a waveguide from a perfect conductor to an impedance sheet Z_s such that

$$\hat{n} \times \vec{E} = Z_s \vec{H}_{tan} \longrightarrow \hat{n} \times \hat{E}^- = Z_s \hat{H}_{tan}^-, \tag{B.122}$$

where $\hat{n}$ points into the metal and $\hat{H}_{tan}^-$ the magnetic field tangential to the boundary C, then upon substitution

$$\gamma = \frac{\oint_C Z_s \hat{H}_{tan}^- \cdot \hat{H}_0^+ \, dl}{\int_S \left(\hat{E}_0^+ \times \hat{H}^- - \hat{E}^- \times \hat{H}_0^+ \right) \cdot \hat{z}\, ds} + \gamma_0. \tag{B.123}$$

Let the unperturbed guide be homogenously filled with isotropic lossy material and its walls PEC, so that $\gamma_0 = \alpha_0 + j\beta_0$. For the perturbed guide, let $\gamma = \alpha + j\beta$ and

$$Z_s = R + jX = \sqrt{\frac{\mu_c}{\epsilon_c - j\sigma_c/\omega}} \tag{B.124}$$

be the equivalent surface impedance given by the complex wave impedance for a plane wave in a non-PEC medium. The parameters μ_c, ϵ_c, σ_c are the permeability, permittivity, conductivity of the metal, respectively. If the perturbation approximation,

$\hat{E}^- \approx \hat{E}_0^-$ and $\hat{H}^- \approx \hat{H}_0^-$ are valid then γ can be obtained. To find $\hat{E}_0^-$ and $\hat{H}_0^-$, recall that if

$$\hat{E}_0^+ = \vec{E}_T^+ + \hat{z}E_z^+, \qquad \hat{H}_0^+ = \vec{H}_T^+ + \hat{z}H_z^+, \tag{B.125}$$

then Maxwell's equations are consistent for

$$\hat{E}_0^- = \vec{E}_T^+ - \hat{z}E_z^+, \qquad \hat{H}_0^- = -\vec{H}_T^+ + \hat{z}H_z^+. \tag{B.126}$$

Using the above definitions,

$$\gamma = \frac{\oint_C Z_s \hat{H}_{tan}^- \cdot \hat{H}_0^+ \, dl}{-2\int_S \vec{E}_T^+ \times \vec{H}_T^+ \cdot \hat{z} \, ds} + \gamma_0 = \frac{\oint_C Z_s \hat{H}_{tan}^- \cdot \hat{H}_0^+ \, dl}{-2Y^+ \int_S \vec{E}_T^+ \cdot \vec{E}_T^+ \, ds} + \gamma_0, \tag{B.127}$$

where Y^+ is the forward wave admittance.

B.3.2 Cylindrical Waveguide

In the case of a cylindrical waveguide with radius $\rho = a$,

$$\hat{E}^- \approx \hat{E}_0^- = \vec{E}_T^+ - \hat{z}E_z^+ = E_\rho^+ \hat{\rho} + E_\phi^+ \hat{\phi} - E_z^+ \hat{z}, \tag{B.128}$$

$$\hat{H}^- \approx \hat{H}_0^- = -\vec{H}_T^+ + \hat{z}H_z^+ = -H_\rho^+ \hat{\rho} - H_\phi^+ \hat{\phi} + H_z^+ \hat{z}, \tag{B.129}$$

and

$$\hat{H}_{tan}^- = -H_\phi^+ \hat{\phi} + H_z^+ \hat{z}, \; \hat{n} = \hat{\rho}. \tag{B.130}$$

If Z_s is not a function of the contour C, then

$$\gamma = \frac{Z_s \oint_C \left(H_z^2 - H_\phi^2 \right) \, dl}{-2Y \int_S \vec{E}_T \cdot \vec{E}_T \, ds} + \gamma_0, \tag{B.131}$$

where the + superscripts are suppressed to simplify notation. Without loss of generality, the following derivations assume $z = 0$.

TE Modes ($Y_{1nm} = \frac{\gamma_{0_{1nm}}}{j\omega\mu}$)

$$H_{z_{1nm1}} = A_{1nm1} \sin(n\phi) J_n(k_{c_{1nm}}\rho), \tag{B.132}$$

$$H_{\phi_{1nm1}} = \frac{-\gamma_{0_{1nm}} n}{k_{c_{1nm}}^2 \rho} A_{1nm1} \cos(n\phi) J_n(k_{c_{1nm}}\rho), \tag{B.133}$$

$$\oint_C \left(H_{z_{1nm1}}^2 - H_{\phi_{1nm1}}^2\right) dl = \int_0^{2\pi} \left(H_{z_{1nm1}}^2 - H_{\phi_{1nm1}}^2\right)\Big|_{\rho=a} a\, d\phi \tag{B.134}$$
$$= \begin{cases} \pi a A_{1nm1}^2 J_n^2(k_{c_{1nm}} a)\left(1 - \frac{\gamma_{0_{1nm}}^2 n^2}{k_{c_{1nm}}^4 a^2}\right), & n \neq 0; \\ 0\,(\text{do not exist}), & n = 0. \end{cases}$$

$$E_{\rho_{1nm1}} = \frac{-j\omega\mu n}{k_{c_{1nm}}^2 \rho} A_{1nm1} \cos(n\phi) J_n(k_{c_{1nm}}\rho), \tag{B.135}$$

$$E_{\phi_{1nm1}} = \frac{j\omega\mu}{k_{c_{1nm}}} A_{1nm1} \sin(n\phi) J_n'(k_{c_{1nm}}\rho), \tag{B.136}$$

$$\int_S \vec{E}_{T_{1nm1}} \cdot \vec{E}_{T_{1nm1}}\, ds = \int_0^{2\pi}\int_0^a \left(E_{\rho_{1nm1}}^2 + E_{\phi_{1nm1}}^2\right) \rho\, d\rho\, d\phi \tag{B.137}$$
$$= \begin{cases} -\pi \frac{\omega^2\mu^2}{k_{c_{1nm}}^2} A_{1nm1}^2 \frac{a^2}{2}\left(1 - \frac{n^2}{k_{c_{1nm}}^2 a^2}\right) J_n^2(k_{c_{1nm}} a), & n \neq 0; \\ 0\,(\text{do not exist}), & n = 0. \end{cases}$$

$$\gamma_{1nm1} = \frac{Z_s \int_0^{2\pi}\left(H_{z_{1nm1}}^2 - H_{\phi_{1nm1}}^2\right)\Big|_{\rho=a} a\, d\phi}{-2Y_{1nm}\int_0^{2\pi}\int_0^a \left(E_{\rho_{1nm1}}^2 + E_{\phi_{1nm1}}^2\right)\rho\, d\rho\, d\phi} + \gamma_{0_{1nm}} \tag{B.138}$$
$$= \begin{cases} \frac{\left(1 - \frac{\gamma_{0_{1nm}}^2 n^2}{k_{c_{1nm}}^4 a^2}\right) Z_s}{Y_{1nm} a \frac{\omega^2\mu^2}{k_{c_{1nm}}^2}\left(1 - \frac{n^2}{k_{c_{1nm}}^2 a^2}\right)} + \gamma_{0_{1nm}}, & n \neq 0; \\ \text{do not exist}, & n = 0. \end{cases}$$

$$H_{z_{1nm2}} = A_{1nm2} \cos(n\phi) J_n(k_{c_{1nm}}\rho), \tag{B.139}$$

$$H_{\phi_{1nm2}} = \frac{\gamma_{0_{1nm}} n}{k_{c_{1nm}}^2 \rho} A_{1nm2} \sin(n\phi) J_n(k_{c_{1nm}}\rho), \tag{B.140}$$

$$\oint_C \left(H_{z_{1nm2}}^2 - H_{\phi_{1nm2}}^2\right) dl = \int_0^{2\pi} \left(H_{z_{1nm2}}^2 - H_{\phi_{1nm2}}^2\right)\Big|_{\rho=a} a\, d\phi \tag{B.141}$$
$$= \begin{cases} \pi a A_{1nm2}^2 J_n^2(k_{c_{1nm}} a)\left(1 - \frac{\gamma_{0_{1nm}}^2 n^2}{k_{c_{1nm}}^4 a^2}\right), & n \neq 0; \\ 2\pi a A_{10m2}^2 J_0^2(k_{c_{10m}} a), & n = 0. \end{cases}$$

$$E_{\rho_{1nm2}} = \frac{j\omega\mu n}{k_{c_{1nm}}^2 \rho} A_{1nm2} \sin(n\phi) J_n(k_{c_{1nm}}\rho), \tag{B.142}$$

$$E_{\phi_{1nm2}} = \frac{j\omega\mu}{k_{c_{1nm}}} A_{1nm2} \cos(n\phi) J_n'(k_{c_{1nm}}\rho), \tag{B.143}$$

$$\int_S \vec{E}_{T_{1nm2}} \cdot \vec{E}_{T_{1nm2}}\, ds = \int_0^{2\pi} \int_0^a \left(E^2_{\rho_{1nm2}} + E^2_{\phi_{1nm2}}\right) \rho\, d\rho\, d\phi \tag{B.144}$$
$$= \begin{cases} -\pi \frac{\omega^2\mu^2}{k^2_{c_{1nm}}} A^2_{1nm2} \frac{a^2}{2} \left(1 - \frac{n^2}{k^2_{c_{1nm}} a^2}\right) J^2_n(k_{c_{1nm}} a), & n \neq 0; \\ -2\pi \frac{\omega^2\mu^2}{k^2_{c_{10m}}} A^2_{10m2} \frac{a^2}{2} J^2_0(k_{c_{10m}} a), & n = 0. \end{cases}$$

$$\gamma_{1nm2} = \frac{Z_s \int_0^{2\pi} \left(H^2_{z_{1nm2}} - H^2_{\phi_{1nm2}}\right)\Big|_{\rho=a} a\, d\phi}{-2Y_{1nm} \int_0^{2\pi} \int_0^a \left(E^2_{\rho_{1nm2}} + E^2_{\phi_{1nm2}}\right) \rho\, d\rho\, d\phi} + \gamma_{0_{1nm}} \tag{B.145}$$
$$= \frac{\left(1 - \frac{\gamma^2_{0_{1nm}} n^2}{k^4_{c_{1nm}} a^2}\right) Z_s}{Y_{1nm} a \frac{\omega^2\mu^2}{k^2_{c_{1nm}}} \left(1 - \frac{n^2}{k^2_{c_{1nm}} a^2}\right)} + \gamma_{0_{1nm}},\ n \geq 0.$$

TM Modes ($Y_{2nm} = \frac{j\omega\epsilon}{\gamma_{0_{2nm}}}$)

$$H_{z_{2nm1}} = 0, \tag{B.146}$$
$$H_{\phi_{2nm1}} = \frac{-j\omega\epsilon}{k_{c_{2nm}}} A_{2nm1} \sin(n\phi) J'_n(k_{c_{2nm}}\rho), \tag{B.147}$$

$$\oint_C \left(H^2_{z_{2nm1}} - H^2_{\phi_{2nm1}}\right)\, dl = \int_0^{2\pi} \left(H^2_{z_{2nm1}} - H^2_{\phi_{2nm1}}\right)\Big|_{\rho=a} a\, d\phi \tag{B.148}$$
$$= \begin{cases} \pi a \frac{\omega^2\epsilon^2}{k^2_{c_{2nm}}} A^2_{2nm1} {J'_n}^2(k_{c_{2nm}} a), & n \neq 0; \\ 0\,(\text{do not exist}), & n = 0. \end{cases}$$

$$E_{\rho_{2nm1}} = \frac{-\gamma_{0_{2nm}}}{k_{c_{2nm}}} A_{2nm1} \sin(n\phi) J'_n(k_{c_{2nm}}\rho), \tag{B.149}$$
$$E_{\phi_{2nm1}} = \frac{-\gamma_{0_{2nm}} n}{k^2_{c_{2nm}}\rho} A_{2nm1} \cos(n\phi) J_n(k_{c_{2nm}}\rho), \tag{B.150}$$

$$\int_S \vec{E}_{T_{2nm1}} \cdot \vec{E}_{T_{2nm1}}\, ds = \int_0^{2\pi} \int_0^a \left(E^2_{\rho_{2nm1}} + E^2_{\phi_{2nm1}}\right) \rho\, d\rho\, d\phi \tag{B.151}$$
$$= \begin{cases} \pi \frac{\gamma^2_{0_{2nm}}}{k^2_{c_{2nm}}} A^2_{2nm1} \frac{a^2}{2} {J'_n}^2(k_{c_{2nm}} a), & n \neq 0; \\ 0\,(\text{do not exist}), & n = 0. \end{cases}$$

$$\gamma_{2nm1} = \frac{Z_s \int_0^{2\pi} \left(H_{z_{2nm1}}^2 - H_{\phi_{2nm1}}^2\right)\Big|_{\rho=a} a\, d\phi}{-2Y_{2nm} \int_0^{2\pi} \int_0^a \left(E_{\rho_{2nm1}}^2 + E_{\phi_{2nm1}}^2\right) \rho\, d\rho\, d\phi} + \gamma_{0_{2nm}} \tag{B.152}$$

$$= \begin{cases} \frac{Y_{2nm} Z_s}{a} + \gamma_{0_{2nm}}, & n \neq 0; \\ \text{do not exist}, & n = 0. \end{cases}$$

$$H_{z_{2nm2}} = 0, \tag{B.153}$$

$$H_{\phi_{2nm2}} = \frac{-j\omega\epsilon}{k_{c_{2nm}}} A_{2nm2} \cos(n\phi) J_n'(k_{c_{2nm}}\rho), \tag{B.154}$$

$$\oint_C \left(H_{z_{2nm2}}^2 - H_{\phi_{2nm2}}^2\right) dl = \int_0^{2\pi} \left(H_{z_{2nm2}}^2 - H_{\phi_{2nm2}}^2\right)\Big|_{\rho=a} a\, d\phi \tag{B.155}$$

$$= \begin{cases} \pi a \frac{\omega^2\epsilon^2}{k_{c_{2nm}}^2} A_{2nm2}^2 {J_n'}^2(k_{c_{2nm}} a), & n \neq 0; \\ 2\pi a \frac{\omega^2\epsilon^2}{k_{c_{20m}}^2} A_{20m2}^2 {J_0'}^2(k_{c_{20m}} a), & n = 0. \end{cases}$$

$$E_{\rho_{2nm2}} = \frac{-\gamma_{0_{2nm}}}{k_{c_{2nm}}} A_{2nm2} \cos(n\phi) J_n'(k_{c_{2nm}}\rho), \tag{B.156}$$

$$E_{\phi_{2nm2}} = \frac{\gamma_{0_{2nm}} n}{k_{c_{2nm}}^2 \rho} A_{2nm2} \sin(n\phi) J_n(k_{c_{2nm}}\rho), \tag{B.157}$$

$$\int_S \vec{E}_{T_{2nm2}} \cdot \vec{E}_{T_{2nm2}}\, ds = \int_0^{2\pi} \int_0^a \left(E_{\rho_{2nm2}}^2 + E_{\phi_{2nm2}}^2\right) \rho\, d\rho\, d\phi \tag{B.158}$$

$$= \begin{cases} \pi \frac{\gamma_{0_{2nm}}^2}{k_{c_{2nm}}^2} A_{2nm1}^2 \frac{a^2}{2} {J_n'}^2(k_{c_{2nm}} a), & n \neq 0; \\ 2\pi \frac{\gamma_{0_{20m}}^2}{k_{c_{20m}}^2} A_{20m1}^2 \frac{a^2}{2} {J_0'}^2(k_{c_{20m}} a) & n = 0. \end{cases}$$

$$\gamma_{2nm2} = \frac{Z_s \int_0^{2\pi} \left(H_{z_{2nm2}}^2 - H_{\phi_{2nm2}}^2\right)\Big|_{\rho=a} a\, d\phi}{-2Y_{2nm} \int_0^{2\pi} \int_0^a \left(E_{\rho_{2nm2}}^2 + E_{\phi_{2nm2}}^2\right) \rho\, d\rho\, d\phi} + \gamma_{0_{2nm}} \tag{B.159}$$

$$= \frac{Y_{2nm} Z_s}{a} + \gamma_{0_{2nm}},\ n \geq 0.$$

B.3.3 Rectangular Waveguide

In the case of a rectangular waveguide with length a, width b,

$$\hat{E}^- \approx \hat{E}_0^- = \vec{E}_T^+ - \hat{z}E_z^+ = E_x^+\hat{x} + E_y^+\hat{y} - E_z^+\hat{z}, \tag{B.160}$$

$$\hat{H}^- \approx \hat{H}_0^- = -\vec{H}_T^+ + \hat{z}H_z^+ = -H_x^+\hat{x} - H_y^+\hat{y} + H_z^+\hat{z}, \tag{B.161}$$

and

$$\hat{H}_{tan}^- = \begin{cases} -H_x^+\hat{x} + H_z^+\hat{z}, & \hat{n} = \pm\hat{y}; \\ -H_y^+\hat{y} + H_z^+\hat{z}, & \hat{n} = \pm\hat{x}. \end{cases} \tag{B.162}$$

If Z_s is not a function of the contour C, then

$$\gamma = \frac{Z_s \oint_C \hat{H}_{tan}^- \cdot \hat{H}_0^+ \, dl}{-2Y^+ \int_S \vec{E}_T^+ \cdot \vec{E}_T^+ \, ds} + \gamma_0, \tag{B.163}$$

where

$$\begin{aligned} \oint_C \hat{H}_{tan}^- \cdot \hat{H}_0^+ \, dl = &\int_0^a H_z^2 - H_x^2\big|_{y=0} \, dx + \int_0^b H_z^2 - H_y^2\big|_{x=a} \, dy \\ &\int_a^0 H_z^2 - H_x^2\big|_{y=b} \, (-dx) + \int_b^0 H_z^2 - H_y^2\big|_{x=0} \, (-dy), \end{aligned}$$

and the + superscripts are suppressed to simplify notation. Without loss of generality, the following derivations assume $z = 0$.

TE Modes ($Y_{1mn} = \frac{\gamma_{0_{1mn}}}{j\omega\mu}$)

$$H_{z_{1mn}} = A_{1mn} \cos\left(\frac{m\pi x}{a}\right) \cos\left(\frac{n\pi y}{b}\right), \tag{B.164}$$

$$H_{x_{1mn}} = \frac{\gamma_{0_{1mn}}}{k_{c_{1mn}}^2} \frac{m\pi}{a} A_{1mn} \sin\left(\frac{m\pi x}{a}\right) \cos\left(\frac{n\pi y}{b}\right), \tag{B.165}$$

$$H_{y_{1mn}} = \frac{\gamma_{0_{1mn}}}{k_{c_{1mn}}^2} \frac{n\pi}{b} A_{1mn} \cos\left(\frac{m\pi x}{a}\right) \sin\left(\frac{n\pi y}{b}\right), \tag{B.166}$$

$$\oint_C \hat{H}^-_{tan_{1mn}} \cdot \hat{H}^+_{1mn}\, dl \tag{B.167}$$

$$= \begin{cases} A^2_{1mn}\left[a\left(1-\frac{\gamma^2_{0_{1mn}} m^2\pi^2}{k^4_{c_{1mn}} a^2}\right)+b\left(1-\frac{\gamma^2_{0_{1mn}} n^2\pi^2}{k^4_{c_{1mn}} b^2}\right)\right], & m\neq 0,\ n\neq 0; \\ A^2_{10n}\left[2a+b\left(1-\frac{\gamma^2_{0_{10n}} n^2\pi^2}{k^4_{c_{10n}} b^2}\right)\right], & m=0,\ n\neq 0; \\ A^2_{1m0}\left[a\left(1-\frac{\gamma^2_{0_{1m0}} m^2\pi^2}{k^4_{c_{1m0}} a^2}\right)+2b\right], & m\neq 0,\ n=0; \\ A^2_{100}\left[2a+2b\right] \text{ (do not exist)}, & m=0,\ n=0. \end{cases}$$

$$E_{x_{1mn}} = \frac{j\omega\mu}{k^2_{c_{1mn}}}\frac{n\pi}{b} A_{1mn}\cos\left(\frac{m\pi x}{a}\right)\sin\left(\frac{n\pi y}{b}\right), \tag{B.168}$$

$$E_{y_{1mn}} = \frac{-j\omega\mu}{k^2_{c_{1mn}}}\frac{m\pi}{a} A_{1mn}\sin\left(\frac{m\pi x}{a}\right)\cos\left(\frac{n\pi y}{b}\right), \tag{B.169}$$

$$\int_S \vec{E}_{T_{1mn}} \cdot \vec{E}_{T_{1mn}}\, ds = \int_0^a \int_0^b \left(E^2_{x_{1mn}} + E^2_{y_{1mn}}\right) dx\, dy \tag{B.170}$$

$$= \begin{cases} -\frac{\omega^2\mu^2}{k^4_{c_{1mn}}} A^2_{1mn}\frac{ab}{4}\left[\left(\frac{m\pi}{a}\right)^2+\left(\frac{n\pi}{b}\right)^2\right], & m\neq 0,\ n\neq 0; \\ -\frac{\omega^2\mu^2}{k^4_{c_{10n}}} A^2_{10n}\frac{ab}{2}\left(\frac{n\pi}{b}\right)^2, & m=0,\ n\neq 0; \\ -\frac{\omega^2\mu^2}{k^4_{c_{1m0}}} A^2_{1m0}\frac{ab}{2}\left(\frac{m\pi}{a}\right)^2, & m\neq 0,\ n=0; \\ 0 \text{ (do not exist)}, & m=0,\ n=0. \end{cases}$$

$$\gamma_{1mn} = \frac{Z_s \oint_C \hat{H}^-_{tan_{1mn}} \cdot \hat{H}^+_{1mn}\, dl}{-2Y_{1mn}\int_0^a\int_0^b \left(E^2_{x_{1mn}} + E^2_{y_{1mn}}\right) dx\, dy} + \gamma_{0_{1mn}} \tag{B.171}$$

$$= \begin{cases} \frac{\left[a\left(1-\frac{\gamma^2_{0_{1mn}} m^2\pi^2}{k^4_{c_{1mn}} a^2}\right)+b\left(1-\frac{\gamma^2_{0_{1mn}} n^2\pi^2}{k^4_{c_{1mn}} b^2}\right)\right] Z_s}{Y_{1mn}\frac{\omega^2\mu^2}{k^4_{c_{1mn}}} A^2_{1mn}\frac{ab}{2}\left[\left(\frac{m\pi}{a}\right)^2+\left(\frac{n\pi}{b}\right)^2\right]} + \gamma_{0_{1mn}}, & m\neq 0,\ n\neq 0; \\ \frac{\left[2a+b\left(1-\frac{\gamma^2_{0_{10n}} n^2\pi^2}{k^4_{c_{10n}} b^2}\right)\right] Z_s}{Y_{10n}\frac{\omega^2\mu^2}{k^4_{c_{10n}}} A^2_{10n} ab\left(\frac{n\pi}{b}\right)^2} + \gamma_{0_{10n}}, & m=0,\ n\neq 0; \\ \frac{\left[a\left(1-\frac{\gamma^2_{0_{1m0}} m^2\pi^2}{k^4_{c_{1m0}} a^2}\right)+2b\right] Z_s}{Y_{1m0}\frac{\omega^2\mu^2}{k^4_{c_{1m0}}} A^2_{1m0} ab\left(\frac{m\pi}{a}\right)^2} + \gamma_{0_{1m0}}, & m\neq 0,\ n=0; \\ \text{do not exist}, & m=0,\ n=0. \end{cases}$$

TM Modes ($Y_{2mn} = \frac{j\omega\epsilon}{\gamma_{0_{2mn}}}$)

$$H_{z_{2mn}} = 0, \tag{B.172}$$

$$H_{x_{2mn}} = \frac{j\omega\epsilon}{k_{c_{2mn}}^2}\frac{n\pi}{b}A_{2mn}\sin\left(\frac{m\pi x}{a}\right)\cos\left(\frac{n\pi y}{b}\right), \tag{B.173}$$

$$H_{y_{2mn}} = \frac{-j\omega\epsilon}{k_{c_{2mn}}^2}\frac{m\pi}{a}A_{1mn}\cos\left(\frac{m\pi x}{a}\right)\sin\left(\frac{n\pi y}{b}\right), \tag{B.174}$$

$$\oint_C \hat{H}^-_{tan_{2mn}} \cdot \hat{H}^+_{2mn}\, dl \tag{B.175}$$
$$= \begin{cases} A_{2mn}^2 \frac{\omega^2\epsilon^2}{k_{c_{2mn}}^4}\left[a\left(\frac{n\pi}{b}\right)^2 + b\left(\frac{m\pi}{a}\right)^2\right], & m \neq 0,\ n \neq 0; \\ 0 \text{ (do not exist)}, & m \text{ or } n = 0. \end{cases}$$

$$E_{x_{2mn}} = \frac{-\gamma_{0_{2mn}}}{k_{c_{2mn}}^2}\frac{m\pi}{a}A_{2mn}\cos\left(\frac{m\pi x}{a}\right)\sin\left(\frac{n\pi y}{b}\right), \tag{B.176}$$

$$E_{y_{2mn}} = \frac{-\gamma_{0_{2mn}}}{k_{c_{2mn}}^2}\frac{n\pi}{b}A_{2mn}\sin\left(\frac{m\pi x}{a}\right)\cos\left(\frac{n\pi y}{b}\right), \tag{B.177}$$

$$\int_S \vec{E}_{T_{2mn}} \cdot \vec{E}_{T_{2mn}}\, ds = \int_0^a \int_0^b \left(E_{x_{2mn}}^2 + E_{y_{2mn}}^2\right) dx\, dy \tag{B.178}$$
$$= \begin{cases} \frac{\gamma_{0_{2mn}}^2}{k_{c_{2mn}}^4} A_{2mn}^2 \frac{ab}{4}\left[\left(\frac{m\pi}{a}\right)^2 + \left(\frac{n\pi}{b}\right)^2\right], & m \neq 0,\ n \neq 0; \\ 0 \text{ (do not exist)}, & m \text{ or } n = 0. \end{cases}$$

$$\gamma_{2mn} = \frac{Z_s \oint_C \hat{H}^-_{tan_{2mn}} \cdot \hat{H}^+_{2mn}\, dl}{-2Y_{2mn}\int_0^a \int_0^b \left(E_{x_{2mn}}^2 + E_{y_{2mn}}^2\right) dx\, dy} + \gamma_{0_{2mn}} \tag{B.179}$$
$$= \begin{cases} \frac{Y_{2mn}\left[a\left(\frac{n\pi}{b}\right)^2 + b\left(\frac{m\pi}{a}\right)^2\right]Zs}{\frac{ab}{2}\left[\left(\frac{m\pi}{a}\right)^2 + \left(\frac{n\pi}{b}\right)^2\right]} + \gamma_{0_{2mn}}, & m \neq 0,\ n \neq 0; \\ \text{do not exist}, & m \text{ or } n = 0. \end{cases}$$

B.3.4 Parallel-Plate Waveguide

In the case of a parallel-plate waveguide with separation d,

$$\hat{E}^- \approx \hat{E}_0^- = \vec{E}_T^+ - \hat{z}E_z^+ = E_x^+\hat{x} + E_y^+\hat{y} - E_z^+\hat{z}, \tag{B.180}$$

$$\hat{H}^- \approx \hat{H}_0^- = -\vec{H}_T^+ + \hat{z}H_z^+ = -H_x^+\hat{x} - H_y^+\hat{y} + H_z^+\hat{z}, \tag{B.181}$$

and

$$\hat{H}^-_{tan} = \begin{cases} -H^+_x \hat{x} + H^+_z \hat{z}, & \hat{n} = \pm\hat{y} \text{ (horizontal)}; \\ -H^+_y \hat{y} + H^+_z \hat{z}, & \hat{n} = \pm\hat{x} \text{ (vertical)}. \end{cases} \tag{B.182}$$

If Z_s is not a function of the contour C, then

$$\gamma = \frac{Z_s \oint_C \hat{H}^-_{tan} \cdot \hat{H}^+_0 \, dl}{-2Y^+ \int_S \vec{E}^+_T \cdot \vec{E}^+_T \, ds} + \gamma_0, \tag{B.183}$$

where

$$\oint_C \hat{H}^-_{tan} \cdot \hat{H}^+_0 \, dl = \tag{B.184}$$
$$\begin{cases} \int_0^l H_z^2 - H_x^2\big|_{y=0} \, dx + \int_l^0 H_z^2 - H_x^2\big|_{y=d} \, (-dx), & \hat{n} = \pm\hat{y}, \\ \int_0^l H_z^2 - H_y^2\big|_{x=0} \, dy + \int_l^0 H_z^2 - H_y^2\big|_{x=0} \, (-dy), & \hat{n} = \pm\hat{x}, \end{cases}$$

where l is an arbitrary length of the plate and + superscripts are suppressed to simplify notation. Without loss of generality, the following derivations assume $z = 0$.

TE Modes

For the horizontal case ($Y_{1n} = \frac{\gamma_{0_{1n}}}{j\omega\mu}$):

$$H_{z_{1n}} = A_{1n} \cos\left(\frac{n\pi y}{d}\right), \tag{B.185}$$

$$H_{x_{1n}} = 0, \tag{B.186}$$

$$E_{x_{1n}} = \frac{j\omega\mu}{k_{c_{1n}}} A_{1n} \sin\left(\frac{n\pi y}{d}\right), \tag{B.187}$$

$$E_{y_{1n}} = 0. \tag{B.188}$$

$$\oint_C \hat{H}^-_{tan_{1n}} \cdot \hat{H}^+_{0_{1n}} \, dl = 2lA^2_{1n}. \tag{B.189}$$

$$\int_S \vec{E}^+_{T_{1n}} \cdot \vec{E}^+_{T_{1n}\, ds} = \int_0^l \int_0^d E^2_{x_{1n}} \, dx \, dy = \begin{cases} -\frac{\omega^2\mu^2}{k^2_{c_{1n}}} A^2_{1n} \frac{ld}{2}, & n \neq 0; \\ 0 \text{ (do not exist)}, & n = 0. \end{cases} \tag{B.190}$$

$$\gamma_{1n} = \frac{Z_s \oint_C \hat{H}^-_{tan_{1n}} \cdot \hat{H}^+_{0_{1n}} \, dl}{-2Y_{1n} \int_0^l \int_0^d E^2_{x_{1n}} \, dx \, dy} + \gamma_{0_{1n}} = \begin{cases} \frac{Z_s}{Y_{1n} \frac{\omega^2\mu^2}{k^2_{c_{1n}}} \frac{d}{2}} + \gamma_{0_{1n}}, & n \neq 0; \\ \text{do not exist}, & n = 0. \end{cases} \tag{B.191}$$

For the vertical case ($Y_{1m} = \frac{\gamma_{0_{1m}}}{j\omega\mu}$):

$$H_{z_{1m}} = A_{1m}\cos\left(\frac{m\pi x}{d}\right), \tag{B.192}$$

$$H_{y_{1m}} = 0, \tag{B.193}$$

$$E_{x_{1m}} = 0, \tag{B.194}$$

$$E_{y_{1m}} = \frac{-j\omega\mu}{k_{c_{1m}}} A_{1m}\sin\left(\frac{m\pi x}{d}\right). \tag{B.195}$$

$$\oint_C \hat{H}^-_{tan_{1m}} \cdot \hat{H}^+_{0_{1m}}\, dl = 2lA^2_{1m}. \tag{B.196}$$

$$\int_S \vec{E}^+_{T_{1m}} \cdot \vec{E}^+_{T_{1m}\, ds} = \int_0^l \int_0^d E^2_{y_{1m}}\, dy\, dx = \begin{cases} -\frac{\omega^2\mu^2}{k^2_{c_{1m}}} A^2_{1m}\frac{ld}{2}, & m \neq 0; \\ 0 \text{ do not exist}, & m = 0. \end{cases} \tag{B.197}$$

$$\gamma_{1m} = \frac{Z_s \oint_C \hat{H}^-_{tan_{1m}} \cdot \hat{H}^+_{0_{1m}}\, dl}{-2Y_{1m}\int_0^l \int_0^d E^2_{y_{1m}}\, dy\, dx} + \gamma_{0_{1m}} = \begin{cases} \frac{Z_s}{Y_{1m}\frac{\omega^2\mu^2}{k^2_{c_{1m}}}\frac{d}{2}} + \gamma_{0_{1m}}, & m \neq 0; \\ \text{do not exist}, & m = 0. \end{cases} \tag{B.198}$$

TM Modes

For the horizontal case ($Y_{2n} = \frac{j\omega\epsilon}{\gamma_{0_{2n}}}$):

$$H_{z_{2n}} = 0, \tag{B.199}$$

$$H_{x_{2n}} = \frac{j\omega\epsilon}{k_{c_{2n}}} A_{2n}\cos\left(\frac{n\pi y}{d}\right), \tag{B.200}$$

$$E_{x_{2n}} = 0, \tag{B.201}$$

$$E_{y_{2n}} = \frac{-\gamma_{0_{2n}}}{k_{c_{2n}}} A_{2n}\cos\left(\frac{n\pi y}{d}\right). \tag{B.202}$$

$$\oint_C \hat{H}^-_{tan_{2n}} \cdot \hat{H}^+_{0_{2n}}\, dl = 2l\frac{\omega^2\epsilon^2}{k^2_{c_{2n}}} A^2_{2n}. \tag{B.203}$$

$$\int_S \vec{E}^+_{T_{2n}} \cdot \vec{E}^+_{T_{2n}\, ds} = \int_0^l \int_0^d E^2_{y_{2n}}\, dy\, dx = \begin{cases} \frac{\gamma^2_{0_{2n}}}{k^2_{c_{2n}}} A^2_{2n}\frac{ld}{2}, & n \neq 0; \\ \frac{\gamma^2_{0_{20}}}{k^2_{c_{20}}} A^2_{20} ld, & n = 0. \end{cases} \tag{B.204}$$

$$\gamma_{2n} = \frac{Z_s \oint_C \hat{H}^-_{tan_{2n}} \cdot \hat{H}^+_{0_{2n}}\, dl}{-2Y_{2n}\int_0^l \int_0^d E^2_{y_{2n}}\, dy\, dx} + \gamma_{0_{2n}} = \begin{cases} \frac{2Y_{2n}Z_s}{d} + \gamma_{0_{2n}}, & n \neq 0; \\ \frac{Y_{20}Z_s}{d} + \gamma_{0_{20}}, & n = 0. \end{cases} \tag{B.205}$$

For the vertical case ($Y_{2n} = \frac{j\omega\epsilon}{\gamma_{0_{2m}}}$):

$$H_{z_{2m}} = 0, \tag{B.206}$$

$$H_{y_{2m}} = \frac{-j\omega\epsilon}{k_{c_{2m}}} A_{2m} \cos\left(\frac{m\pi x}{d}\right), \tag{B.207}$$

$$E_{x_{2m}} = \frac{-\gamma_{0_{2m}}}{k_{c_{2m}}} A_{2m} \cos\left(\frac{m\pi x}{d}\right), \tag{B.208}$$

$$E_{y_{2m}} = 0. \tag{B.209}$$

$$\oint_C \hat{H}^-_{tan_{2m}} \cdot \hat{H}^+_{0_{2m}}\, dl = 2l \frac{\omega^2\epsilon^2}{k^2_{c_{2m}}} A^2_{2m}. \tag{B.210}$$

$$\int_S \vec{E}^+_{T_{2m}} \cdot \vec{E}^+_{T_{2m}\, ds} = \int_0^l \int_0^d E^2_{x_{2m}}\, dx\, dy = \begin{cases} \frac{\gamma^2_{0_{2m}}}{k^2_{c_{2m}}} A^2_{2m} \frac{ld}{2}, & m \neq 0; \\ \frac{\gamma^2_{0_{20}}}{k^2_{c_{20}}} A^2_{20} ld, & m = 0. \end{cases} \tag{B.211}$$

$$\gamma_{2m} = \frac{Z_s \oint_C \hat{H}^-_{tan_{2m}} \cdot \hat{H}^+_{0_{2m}}\, dl}{-2Y_{2m} \int_0^l \int_0^d E^2_{x_{2m}}\, dx\, dy} + \gamma_{0_{2m}} = \begin{cases} \frac{2Y_{2m}Z_s}{d} + \gamma_{0_{2m}}, & m \neq 0; \\ \frac{Y_{20}Z_s}{d} + \gamma_{0_{20}}, & m = 0. \end{cases} \tag{B.212}$$

B.4 Transition Integrals

At an air-metal or waveguide-waveguide transition, finite conductance of the metal at the interface contributes to loss. This is taking into account in the mode-matching procedure using the impedance boundary condition over the support of $\Omega^a - \Omega^b$ by evaluating the surface admittance matrix $\mathbf{Y^s}$, where

$$Y^s_{mn} = \mp Z_s Y^a_m Y^{a*}_n \left(\delta_{mn} - \int_{\Omega^b} \vec{E}^a_{T_m} \cdot \vec{E}^{a*}_{T_n}\, dS\right). \tag{B.213}$$

To illustrate this process, we evaluate

$$\int_{\Omega^b} \vec{E}^a_{T_m} \cdot \vec{E}^{a*}_{T_n}\, dS \tag{B.214}$$

for an air/metal transition where Ω^a is a Floquet unit cell and the metal of finite conductivity σ is perforated by a circular aperture of radius ρ_b.

Floquet Modes in Cylindrical Coordinates

The longitudinal Floquet modes in cylindrical coordinates are given by:

$$\psi^a_{\nu mn} = \tilde{A}^a_{\nu mn} e^{-jk_{r_{mn}}\rho\cos(\phi-\theta_{mn})}, \tag{B.215}$$

where $\theta_{mn} = \tan^{-1}(k_{y_{mn}}/k_{x_{mn}})$,

$$\tilde{A}^a_{1mn} = \frac{k_{r_{mn}}}{\omega\mu}\frac{1}{\sqrt{S}} e^{j\zeta_{1mn}}, \tag{B.216}$$

$$\tilde{A}^a_{2mn} = \frac{k_{r_{mn}}}{|\beta_{mn}|}\frac{1}{\sqrt{S}} e^{j\zeta_{2mn}}, \tag{B.217}$$

are the orthonormalized field amplitudes, $\nu = 1 \equiv$ TE, $\nu = 2 \equiv$ TM and S is the surface area of Ω^a. To evaluate for the transverse fields, it is necessary to first find the transverse gradient of the longitudinal potentials in the cylindrical coordinate system,

$$\begin{aligned}\nabla_T \psi^a_{\nu mn} = &- jk_{r_{mn}}\cos(\phi-\theta_{mn})\tilde{A}^a_{\nu mn} e^{-jk_{r_{mn}}\rho\cos(\phi-\theta_{mn})}\hat{\rho} \\ &+ jk_{r_{mn}}\sin(\phi-\theta_{mn})\tilde{A}^a_{\nu mn} e^{-jk_{r_{mn}}\rho\cos(\phi-\theta_{mn})}\hat{\phi};\end{aligned} \tag{B.218}$$

the transverse electric fields are

$$\vec{E}^a_{T_{1mn}} = \frac{j\omega\mu}{k^2_{r_{mn}}}\hat{z}\times\nabla_T\psi^a_{1mn}, \tag{B.219}$$

$$\vec{E}^a_{T_{2mn}} = \frac{-j\beta_{mn}}{k^2_{r_{mn}}}\nabla_T\psi^a_{2mn}. \tag{B.220}$$

Define

$$A = k_{r_{m'n'}}\cos(\theta_{m'n'}) - k_{r_{mn}}\cos(\theta_{mn}) = k_{x_{m'n'}} - k_{x_{mn}}, \tag{B.221}$$

$$B = k_{r_{m'n'}}\sin(\theta_{m'n'}) - k_{r_{mn}}\sin(\theta_{mn}) = k_{y_{m'n'}} - k_{y_{mn}}. \tag{B.222}$$

TE-TE

$$\begin{aligned}\int_{\Omega^b}\vec{E}^a_{T_{1mn}}\cdot\vec{E}^{a*}_{T_{1m'n'}}\,dS &= \frac{\omega\mu}{k^2_{r_{mn}}}\frac{\omega\mu}{k^2_{r_{m'n'}}}\int_{\Omega^b}\hat{z}\times\nabla_T\psi^a_{1mn}\cdot\hat{z}\times\nabla_T\psi^{a*}_{1m'n'}\,dS \\ &= \frac{\omega\mu}{k^2_{r_{mn}}}\frac{\omega\mu}{k^2_{r_{m'n'}}}\int_0^{\rho_b}\int_0^{2\pi}\nabla_T\psi^a_{1mn}\cdot\nabla_T\psi^{a*}_{1m'n'}\,\rho\,d\rho\,d\phi \\ &= \begin{cases}\frac{\cos(\theta_{mn}-\theta_{m'n'})2\pi\rho_b J_1\left(\rho_b\sqrt{A^2+B^2}\right)}{S\sqrt{A^2+B^2}}, & A\neq 0, B\neq 0; \\ \frac{\pi\rho_b^2}{S}, & A=0, B=0.\end{cases}\end{aligned} \tag{B.223}$$

TE-TM

$$\int_{\Omega^b} \vec{E}^a_{T_{1mn}} \cdot \vec{E}^{a*}_{T_{2m'n'}}\, dS = -\frac{\omega\mu}{k^2_{r_{mn}}} \frac{\beta^*_{m'n'}}{k^2_{r_{m'n'}}} \int_{\Omega^b} \hat{z} \times \nabla_T \psi^a_{1mn} \cdot \nabla_T \psi^{a*}_{2m'n'}\, dS \tag{B.224}$$

$$= \begin{cases} \frac{\sin(\theta_{mn}-\theta_{m'n'}) 2\pi\rho_b J_1\left(\rho_b\sqrt{A^2+B^2}\right)}{S\sqrt{A^2+B^2}}, & A \neq 0, B \neq 0; \\ 0, & A = 0, B = 0. \end{cases}$$

TM-TE

$$\int_{\Omega^b} \vec{E}^a_{T_{2mn}} \cdot \vec{E}^{a*}_{T_{1m'n'}}\, dS = -\frac{\beta_{mn}}{k^2_{r_{mn}}} \frac{\omega\mu}{k^2_{r_{m'n'}}} \int_{\Omega^b} \nabla_T \psi^a_{2mn} \cdot \hat{z} \times \nabla_T \psi^{a*}_{1m'n'}\, dS \tag{B.225}$$

$$= \begin{cases} \frac{\sin(\theta_{mn}-\theta_{m'n'}) 2\pi\rho_b J_1\left(\rho_b\sqrt{A^2+B^2}\right)}{S\sqrt{A^2+B^2}}, & A \neq 0, B \neq 0; \\ 0, & A = 0, B = 0. \end{cases}$$

TM-TM

$$\int_{\Omega^b} \vec{E}^a_{T_{2mn}} \cdot \vec{E}^{a*}_{T_{2m'n'}}\, dS = \frac{\beta_{mn}}{k^2_{r_{mn}}} \frac{\beta^*_{m'n'}}{k^2_{r_{m'n'}}} \int_{\Omega^b} \nabla_T \psi^a_{2mn} \cdot \nabla_T \psi^{a*}_{2m'n'}\, dS \tag{B.226}$$

$$= \begin{cases} \frac{\cos(\theta_{mn}-\theta_{m'n'}) 2\pi\rho_b J_1\left(\rho_b\sqrt{A^2+B^2}\right)}{S\sqrt{A^2+B^2}}, & A \neq 0, B \neq 0; \\ \frac{\pi\rho_b^2}{S}, & A = 0, B = 0. \end{cases}$$

Appendix C

Identities

C.1 Vector Identities

$$\nabla_T f \cdot \nabla_T g = \nabla_T \cdot (f \nabla_T g) - g \nabla_T^2 f \tag{C.1}$$

$$\vec{A} \times (\vec{B} \times \vec{C}) = (\vec{A} \cdot \vec{C})\vec{B} - (\vec{A} \cdot \vec{B})\vec{C} \tag{C.2}$$

$$\vec{A} \times \vec{B} \cdot \vec{C} = \vec{A} \cdot \vec{B} \times \vec{C} = \vec{C} \times \vec{A} \cdot \vec{B} \tag{C.3}$$

$$\vec{A} \cdot \nabla_T \psi = \nabla_T \cdot (\psi \vec{A}) - \psi \nabla_T \cdot \vec{A} \tag{C.4}$$

$$\nabla_T f \times \nabla_T g = \nabla_T \times (f \nabla_T g) \tag{C.5}$$

C.2 Integral Identities

$$\int_\Omega \nabla_T \cdot \vec{A}\, ds = \oint_{d\Omega} \vec{A} \cdot \hat{n}\, dl \tag{C.6}$$

$$\int_\Omega (\nabla_T \times \vec{A}) \cdot \hat{n}\, dS = \oint_{d\Omega} \vec{A} \cdot \vec{dl}, \tag{C.7}$$

Appendix D

Sample Code

A sample software implementation of the scattering analysis for thick FSS's having cylindrical perforations of arbitrary longitudinal profile and on-axis symmetry using the MATLAB programming language is outlined by the code below.

```
% Author: Hung Loui (Copyright)
% Date: July 21, 2006
% This code outlines multi-layer mode-matching analysis for thick FSS's
% having cylindrical perforations of arbitrary longitudinal profile and
% on-axis symmetry.

clear all; close all; clc;

% Fundamental Constants
ep0=8.854e-12; mu0=4*pi*1e-7;

% Flags
SAVE_FLAG=0; SHOW_GEOM=1;

% Scaling factor
scal=1;

% Straight Hole
r0=6.528e-3/2*0.9; r0=r0/scal;
r=r0;

% % Linear Taper 1
% dr=(0.308-0.257)/10;
% r=in2m([0.308:-dr:0.257,0.257+dr:dr:0.308]/2);

% % Linear Taper 2
% r0=6.528e-3/2; r0=r0/scal;
% r=r0*linspace(1,0.7,16);
% r=[r(1:end-1),fliplr(r)];

% % Modulated Cos Taper
% r0=6.528e-3/2; r=r0*(0.7+0.3*abs(cos(0:pi/30:pi/2)));
% r=[r(1:end-1),fliplr(r)];

t=ones(1,length(r))*9.24e-3/length(r); t=t/scal;
```

```
ep=ep0*ones(1,length(r))*2.33; mu=mu0*ones(1,length(r));
wN=ones(1,length(r))*2; wM=ones(1,length(r))*2;

[ord,ori]=jreduce(r,ep,mu,wN,wM);

% Enter lattice parameters
db=8.24e-3;dd=db; db=db/scal; dd=dd/scal; alpha=60*pi/180; fM=3;fN=3;

% Show geometry
if SHOW_GEOM == 1,
   geom_plot(r*1e3,t*1e3);
   xlabel('(mm)');ylabel('(mm)'),zlabel('(mm)');
   title(['Unit-Cell Geometry - Thickness = ',num2str(sum(t)*1000,3),'(mm)']);
end

% Create waveguide structure
for n=1:length(r),
    wg{n}=waveguide(r(n),t(n),ep(n),mu(n),wN(n),wM(n));
end

F00_TE=fM*(2*fN+1)+(fN+1); F00_TM=(2*fM+1)*(2*fN+1)+F00_TE;

freq=16.5e9:0.1e9:30e9; freq=freq*scal;
% theta=[0.001,15,30,45,60,75]*pi/180;
theta=45*pi/180;
phi=90*pi/180;

tic;
h = waitbar(0,'Sweep Theta and Frequency');
for theta_n=1:length(theta),
  for freq_n=1:length(freq),
    a=floquet(db,dd,alpha,0,ep0,mu0,fM,fN,theta(theta_n),phi,freq(freq_n));
    disp('Junction #1');
    [wg{1},Sj{1}]=fq2wg(a,wg{1},freq(freq_n));
    Sp{1}=wgprop(wg{1});
    S=cascade(Sj{1},Sp{1});

    for wg_n=1:(length(wg)-1),
      disp(['Junction #',num2str(wg_n+1)]);
      if ord(wg_n)==wg_n, % if the current junction has not been done
        if wg{wg_n}.r > wg{wg_n+1}.r,
          [wg{wg_n},wg{wg_n+1},Sj{wg_n+1}]=...
            wg2wg(wg{wg_n},wg{wg_n+1},freq(freq_n));
          Sp{wg_n+1}=wgprop(wg{wg_n+1});
        else
          [wg{wg_n+1},wg{wg_n},Sj{wg_n+1}]=...
            wg2wg(wg{wg_n+1},wg{wg_n},freq(freq_n));
          Sp{wg_n+1}=wgprop(wg{wg_n+1});
          Sj{wg_n+1}=rot90(Sj{wg_n+1},2);
        end
        S=cascade(S,Sj{wg_n+1},Sp{wg_n+1});
      else % if the current junction has been analyzed
        wg{wg_n+1}=wgupdt(wg{wg_n+1},freq(freq_n));
        Sp{wg_n+1}=wgprop(wg{wg_n+1});
        S=cascade(S,rot90(Sj{ord(wg_n)+1},ori(wg_n)),Sp{wg_n+1});
      end
    end

    disp(['Junction #',num2str(length(wg)+1)]);
    S=cascade(S,rot90(Sj{1},2));
    FSS_S11_TE(freq_n)=S{1,1}(F00_TE,F00_TE);
    FSS_S12_TE(freq_n)=S{1,2}(F00_TE,F00_TE);
    FSS_S21_TE(freq_n)=S{2,1}(F00_TE,F00_TE);
    FSS_S22_TE(freq_n)=S{2,2}(F00_TE,F00_TE);
```

```
    FSS_S11_TM(freq_n)=S{1,1}(F00_TM,F00_TM);
    FSS_S12_TM(freq_n)=S{1,2}(F00_TM,F00_TM);
    FSS_S21_TM(freq_n)=S{2,1}(F00_TM,F00_TM);
    FSS_S22_TM(freq_n)=S{2,2}(F00_TM,F00_TM);

    waitbar(freq_n/length(freq),h,...
            ['\Theta = ',num2str(theta(theta_n)*180/pi,-1),'\circ, ',...
             'Frequency = ', num2str(freq(freq_n)/1e9,3),'GHz'])
    end
    % keep S21_TE and S21_TM as a function of theta and frequency
    T_TE(theta_n,:)=FSS_S21_TE;
    T_TM(theta_n,:)=FSS_S21_TM;
end
close(h);
toc

if SAVE_FLAG==1,
    save('simdata.mat','T_TE','T_TM','theta','phi','freq',...
         'r','t','ep','mu','wN','wM','db','dd','alpha','fM','fN');
end;

% Plot S-parameters for the last theta
figure; set(gcf,'color','w');
subplot(2,2,1); hold on; grid on;
plot(freq/1e9,20*log10(abs(FSS_S21_TE)),'b',...
     freq/1e9,20*log10(abs(FSS_S12_TE)),'b.');
plot(freq/1e9,20*log10(abs(FSS_S21_TM)),'r',...
     freq/1e9,20*log10(abs(FSS_S12_TM)),'r.');
set(gca,'Xlim',[freq(1),freq(end)]/1e9,'Ylim',[-30,0],'box','on');
legend('|S21-TE|','|S12-TE|','|S21-TM|','|S12-TM|',0);
subplot(2,2,2); hold on; grid on;
plot(freq/1e9,angle(FSS_S21_TE)*180/pi,'b',...
     freq/1e9,angle(FSS_S12_TE)*180/pi,'b.');
plot(freq/1e9,angle(FSS_S21_TM)*180/pi,'r',...
     freq/1e9,angle(FSS_S12_TM)*180/pi,'r.');
set(gca,'Xlim',[freq(1),freq(end)]/1e9,'box','on');
legend('\angle S21-TE','\angle S12-TE','\angle S21-TE','\angle S12-TE',0);
subplot(2,2,3); hold on; grid on;
plot(freq/1e9,20*log10(abs(FSS_S11_TE)),'b',...
     freq/1e9,20*log10(abs(FSS_S22_TE)),'b.');
plot(freq/1e9,20*log10(abs(FSS_S11_TM)),'r',...
     freq/1e9,20*log10(abs(FSS_S22_TM)),'r.');
set(gca,'Xlim',[freq(1),freq(end)]/1e9,'Ylim',[-30,0],'box','on');
legend('|S11-TE|','|S22-TE|','|S11-TM|','|S22-TM|','Location','Best');
subplot(2,2,4); hold on; grid on;
plot(freq/1e9,angle(FSS_S11_TE)*180/pi,'b',...
     freq/1e9,angle(FSS_S22_TE)*180/pi,'b.');
plot(freq/1e9,angle(FSS_S11_TM)*180/pi,'r',...
     freq/1e9,angle(FSS_S22_TM)*180/pi,'r.');
set(gca,'Xlim',[freq(1),freq(end)]/1e9,'box','on');
legend('\angle S11-TE','\angle S22-TE','\angle S11-TM','\angle S22-TM',0);

function geom_plot(r,t)
% Author: Hung Loui (Copyright)
% Date: July 21, 2006

figure; axis equal; Vcolor=[132 132 193]; temp_z=-sum(t)/2;
for n=1:length(r),
    [x,y,z]=cylinder(r(n),100);
    [face,vert]=surf2patch(x,y,t(n)*z+temp_z);
    patch(surf2patch(x,y,t(n)*z+temp_z),...
          'FaceVertexCData',Vcolor,'FaceColor','flat');
    temp_z=temp_z+t(n);
    if n<length(r),
```

```
        theta=linspace(0,2*pi,101);
        x=[vert(1:2:length(vert),1)';r(n+1)*cos(theta)];
        y=[vert(1:2:length(vert),2)';r(n+1)*sin(theta)];
        patch(surf2patch(x,y,temp_z*ones(size(x))),...
              'FaceVertexCData',Vcolor,...
              'FaceColor','flat','EdgeColor','k');
    end
end;

view(0,0); cameratoolbar('Show'); grid on;
set(gca,'visible','on','box','on'); set(gcf,'color','w');
cameratoolbar('SetCoordSys','none','SetMode','orbit');
```